Versatile Electrochemical Sensing with a Prussian Blue Zinc Oxide Carbon Nanotube Composite

by Raja Ram Pandey

A dissertation submitted to the Faculty of the Graduate School at Middle Tennessee State University in Partial Fulfillment of the requirements for the degree of Doctor of Philosophy in Molecular Biosciences

Major Professor: Charles C. Chusuei, Ph.D.

Chengshan Wang, Ph.D.

Justin M. Miller, Ph.D.

Anthony L. Farone, Ph.D.

Ying Gao, Ph.D.

In honor to my family and parents, for continued love and support.

Acknowledgements

It is a genuine pleasure to convey my gratitude and deep sense of thanks to my research advisor Dr. Charles C. Chusuei. The keen interest and adherence of my advisor above all his overwhelming attitude to guide me had been significantly responsible for completion of my research work. His scholarly and timely advice, scientific approach, and meticulous scrutiny have helped me to accomplish this task to a great extent. I would like to thank my committee members Drs. Chengshan Wang, Justin M. Miller, Anthony L. Farone and Ying Gao especially for their insightful comments and supports, their valuable time to go through my dissertation and suggestions for required proper corrections. I would like to express my gratitude to Dr. Gao and Dr. Farone for providing me support with the cell culture of A549 and BT20 cells. I am extremely thankful to Drs. Rajarshi Ghosh and Sarah Mathias for providing me cell culture training and helping me a lot. I am excited to extend my thanks to my colleagues of research lab Nawaraj Karki and Christopher Clark for their support and suggestion during my research work.

I would like to be grateful with the Department of Chemistry and Biology for providing me access to the equipment, chemical supplies and laboratory space. I am happy to respect and praise faculty and staff members of Department of chemistry and Biology who gave me amazing courses theoretically and helped me throughout my sojourn in MTSU. I would like to appreciate my friends Harun Roshid, Prithviraj Sripathi and Nayma Alsam who helped me in my stay in the MTSU. I would like to thank my juniors Christopher and Ethan whose friendly support in our research activities is remembered forever.

I would like to offer special thanks to my wife, Kabita Baniya for taking care of me with unabating patience and supporting me throughout my life. Many thanks go to my little daughters, Kristina Pandey and Riya Pandey for providing enjoyable environment in my stay in Murfreesboro, TN. Finally, I am thankful to God who brought me in this world for the specific purpose of my life and the journey of MTSU study. I am very grateful to my parents, Jamuna Maya Pandey and Khadananda Pandey for their emotional and physical support. At the end, I would like to thank and remember my sisters and brothers especially Navaraj Pandey who have always encouraged and supported me to pursue higher education.

ABSTRACT

The design of a sensor is currently required for reliable, accurate and rapid quantification of hydrogen peroxide (H_2O_2). The selective measurement of H_2O_2 in complex systems is crucial because H_2O_2 plays a vital role in various fields such as cosmetic and pharmaceutical companies, clinical control, chemical and biochemical industry, agriculture products, fuel cells, environmental protection, organic synthesis and cancer cell analysis. Complex, time consuming and expensive methods are used to determine H_2O_2 concentrations under current practices.

Our method uses electrochemical techniques for real-time monitoring of H_2O_2 directly. To design a selective and sensitive sensor for H_2O_2, the earth rich materials including ZnO, carbon nanotubes (CNTs) and Prussian Blue (PB) were synthesized and applied. ZnO nanoparticles were synthesized using a reflux-synthesis process before attaching them to functionalized CNTs (COOH-MWNTs). After tethering refluxed ZnO to carboxylic acid functionalized multiwalled carbon nanotubes (COOH-MWNTs), an electrochemical sensing composite was produced by electrostatically attaching Prussian Blue to ZnO/COOH-MWNTs to enhance sensitivity towards H_2O_2. ZnO nanoparticles were characterized by transmission electron microscopy (TEM). A simple ultrasonication process was used to tether ZnO synthesized nanoparticles. Finally, PZC concept was applied to attach PB on the surface of ZnO/COOH-MWNTs. The morphology and chemical composition of ZnO/COOH-MWNTs and PB/ZnO/COOH-MWNTs composites were studied under TEM, Raman spectroscopy, Fourier transform infrared spectroscopy (FTIR), and X-ray photoelectron spectroscopy (XPS). The modification of glassy carbon electrode (GCE) was performed using the PB/ZnO/COOH-MWNTs. Nafion(2wt%) was used to cap the nanocomposite on the GCE to design a Nafion/PB/ZnO/COOH-MWNTs sensor to monitor H_2O_2. The electrocatalytic activity of the prepared sensor for the reduction and oxidation of H_2O_2 was

examined under cyclic voltammetry (CV) and chronoamperometry (CA) techniques. The cytotoxicity study of the PB/ZnO/COOH-MWNTs composite for its potential *in vivo* use was also done with the help of an Alamar Blue assay.

A practical use of Nafion/PB/ZnO/COOH-MWNTs/GCE sensor for *ex situ* determination of H_2O_2 in BT20 and 4T1 cancer cells was explained. The sensor demonstrated a wide linear response in the range of 1 µM to 3 mM concentration at an operating potential of -0.004 V on the potentiostat. In addition, this sensor was used to delineate the role of oxidative stress in cancer cell viability by measuring the concentration of H_2O_2 in response to apoptosis in BT20 cancer cells. This sensor shows excellent reproducibility, good stability and it is used as versatile sensor to measure H_2O_2 in different environments. In addition, the same sensor is versatile to study other analytes such as homomvanillic acid, dopamine and glutathione at different potentials.

TABLE OF CONTENTS

PAGE

LIST OF TABLES

TABLE **PAGE**

LIST OF FIGURES

FIGURE **PAGE**

Chapter 1

GENERAL INTRODUCTION

1.1 Background and Literature Review

The first observation of carbon nanotubes (CNTs) was in 1952 [1]. CNTs, varying from 4 to 30 nm in diameter and maximum 1 μm in length, were re-discovered by Iijima on the negative end of carbon electrode applied in the d. c. arc-discharge evaporation of carbon in an argon-filled vessel (100 Torr). The introduction of carbon nanotubes (CNT) by Iijima [2] and C_{60}, fullerenes by Kroto et al. [3] has greatly changed the direction of science and technology. When the matter dimensions appear under nanometer size scales, larger percentages of atoms are exposed on the outermost surface, resulting in the greater surface area-to-volume ratio for unique and exciting properties [4]. Because of the many annual publications related with CNTs, these nanotubes are currently most attractive materials of interest. Numerous publications relating to CNTs are growing rapidly. Understanding the fundamentals and applications of CNTs is the main focus of the current research. A wide impact of CNTs shows the potential applications in biomedical sensing, drug and gene delivery, energy storage, microelectronics and various other fields of research. Another interesting field of research is the structure and surface modification of CNTs, resulting in the synthesis of very impressive chemical, mechanical, electrical and optical properties. Currently, electrochemical sensing using the CNTs is rising as one of the most exciting field of research [5-12].

The design of a sensor in increasingly demand for a rapid, accurate and reliable determination of biological analytes is needed [13]. Different analytes such as ascorbic acid,

bilirubin, folic acid, hydrogen peroxide, bicarbonate, acetaminophen, uric acid, dopamine, homovanilic acid and glutathione generally exists in biological samples with its mixture composition. It is important to selectively determine H_2O_2 as it plays a crucial role in many fields, including cosmetics [14], food and agricultural products [15, 16], chemical [17], pharmaceutical [14], biochemical industries [17-19], environmental protection [20], clinical control [21-25], fuel cells [26, 27], swimming pool disinfection [28] and oxidative stress in breast cancer cells [29].

For an accurate, reliable, and rapid analysis of hydrogen peroxide (H_2O_2), a significance of designing a biosensor has increased in recent years [30]. Selective and accurate detection of H_2O_2 is crucial step for screening of cholesterol in blood to control cardiovascular diseases [31], detecting the beginning of food spoilage and observing signaling events triggering reactive oxygen species generation [32]. H_2O_2 is a final product of different enzymatic reactions and H_2O_2 concentration may be used directly as an indicator of reaction progress [30]. An increased level of H_2O_2 may assist in releasing the potent hydroxyl radical in the human brain [33]. H_2O_2 is established as the mediator of cellular pathology and oxidative signaling and has a role in the origin of many neurodegenerative diseases, such as Parkinson's disease [18, 34-36]. H_2O_2 facilitates in signaling pathways for cytotoxicity and takes part in the cell's ability to response to bacteria and other diseases at its physiological level [37]. It operates as a second messenger in cellular signal amplification and transduction so that it demonstrates a major role to regulate a number of oxidative stress-related states [38]. H_2O_2, the most stable component of reactive oxygen species (peroxides, superoxides, hydroxyl radical and singlet oxygen), can damage cellular proteins, DNA, lipid molecules with the consequence of the dysfunction of cells above the physiological concentration resulting in aging and age-related disease states initiating from neurodegeneration

to diabetes to cancer and ultimately apoptosis [39]. Tumor cells generate more H_2O_2 compared with normal cells [40]. Hence, studying a wide concentration range of H_2O_2 can upgrade our comprehensive view of the progression of cancer cells at the early stage.

The use of spectrophotometry [41, 42], fluorescence [43], chemiluminescence [44, 45], titration [46] and electrochemical techniques [36, 47, 48] are widespread uses to analyze H_2O_2 concentration. The electrochemical method has low operating cost, simple, and fast process compared to other methods. This exceptional method particularly provides many benefits such as convenient operation, possibility of miniaturization and low operating cost [49]. The state-of-the-art technology uses expensive metals like gold (Au) [48] and platinum (Pt) [47] to alter the fundamental electrode substrates, such as glassy carbon electrodes (GCE). GCE is also recognized as "glass-like or vitreous carbon" electrode. GCE contains unique properties so that it can resist chemical attack, high temperature, hardness (6-7 mhos) and impermeability to gases and liquids [50, 51]. GCE is inert under aqueous solution condition. It is shown that the hydronium ion reduction on the Pt electrode and GCE surface had 2.10 V difference against the standard hydrogen electrode at normal temperature. This potential difference occurs due to the Pt-H covalent bond formation [52], displaying the higher inertness of GCE compared to Pt electrode. Similarly, GCE displays slow kinetics and it requires a high overpotential during redox reactions so that its efficient quantification of H_2O_2 is restricted [53]. Moreover, although electrochemical processes are used to obtain direct and real-time determination of biological samples [36, 24, 54], high positive potential (generally +0.6 V against saturated calomel electrode (SCE)) is needed due to direct oxidation of H_2O_2 on the bare conventional electrode surface so that potential co-oxidative interferences are realized from other analytes such as ascorbic acid and uric acid [36]. Therefore,

developing highly-sensitive and selective biosensor is of great importance for quantification of H_2O_2 without using these expensive elements at its reduction potential [13, 22, 54].

ZnO is an n-type semi-conductor material. Since it has exciton binding energy (60 meV), wide band gap (3.37 eV) and high breakdown strength, it is an ideal candidate for bio-sensing materials [32, 55, 56]. PB is believed to be an artificial enzyme peroxidase and it is extensively used in the preparation of electrochemical sensors [57]. It is common for its electrochemical, electrochromic, photophysical and magnetic properties and it has potential analytical applications [58]. PB shows a face-centered cubic lattice structure of a hexacyanoferrate having ferric (Fe^{+3}) and ferrous (Fe^{+2}) ions alternating in the cubic lattice sites, associating with nitrogen and carbon atoms of cyanide groups, respectively. It has formula, $Fe_4^{+3}[Fe^{+2}(CN)_6]_3$ with different redox states [59].

Various materials are widely used to modify GCE. For detection of NADH, Musameh et al. modified GCE with carbon nanotubes (CNTs), observing a decrease in overpotential upon the application of CNTs [60]. Wang et al. modified GCEs for the analysis of cytochrome c using single-walled carbon nanotubes [61]. Wayu et al. [32] were able to attach ZnO with MWNTs to detect hydrogen peroxide. This modified electrode displays the remarkable electrocatalytic activity and stable response with H_2O_2. Lu et al. [62] deposited Prussian blue (PB) on the gold surface using electrolysis process to detect H_2O_2 in micromolar range.

1.2 Structure and properties of CNTs

Diamond and graphite are allotropes of carbon including ionsdaleite, C60, C70, C540, carbon nanotubes and amorphous carbon [2]. CNTs are considered as seamless cylinders obtained by rolling of a one-atom thick layer of graphite, known as graphene [63]. CNTs are classified into a single-walled carbon nanotubes (SWNTs) and multi-walled carbon nanotubes (MWNTs) based on the number of graphene sheets. A single graphene sheet rolled-up into a tube refers to SWNTs

whereas a number of concentric layers of graphene sheets shows MWNTs. The different angles and curvatures of CNTs determines the exact structure of it. The graphene sheet can be rolled up into a tube and are explained with the help of one dimensional unit cell as described by a lattice vector (T) and a chiral vector (C_h) (Figure 1.1). The definition of C_h mathematically is $C_h = na_1+ma_2$, where a_1 and a_2 are the basic vectors of the honeycomb lattice. Then integers, n and m ($n \geq m$) regulates the chiral angle 0. This angle is an angle between the zigzag direction of the honeycomb lattice and the direction of the chiral vector, C_h. One dimensional translational vector of nanotubes is called the lattice vector T along the nanotube direction normal to C_h [63].

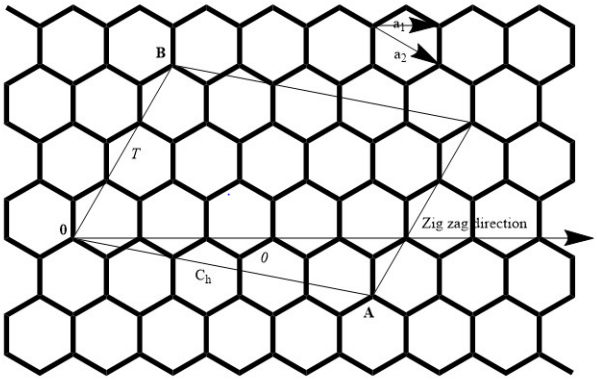

Figure 1.1: Two dimensional graphene sheet representing the vectors that define the structure of nanotubes.

The vector (n, m) represents the chirality of the nanotube. Zigzag nanotubes are given by the vectors (0, m) or (n, 0). The vector (n, n) displays armchair nanotubes whereas the other vector (n, m) shows chiral or helical nanotubes. The chiral angles 0^o and 30^o denote zigzag and armchair nanotubes, respectively while the chiral angles between those angles is for chiral nanotubes (i.e. $0^o<0<30^o$) (Figure 1.2).

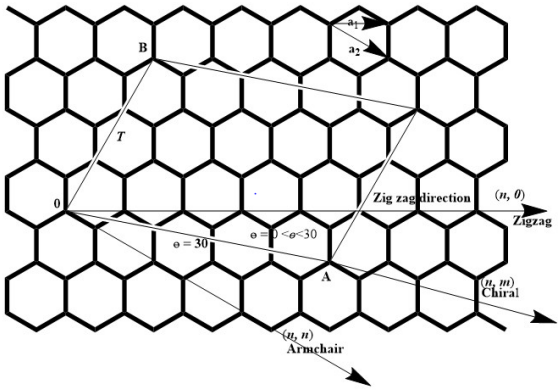

Figure 1.2: Schematic diagram displaying three types of SWNTs formed by rolling up a graphene sheet into tube at different angles.

The nanotube's diameter can be calculated as:

$$d = \frac{a}{n}\sqrt{n^2 + nm + m^2} \quad \text{where a = 0.246 nm}$$

Various chiralities and diameters result in different kinds of nanotubes with their own marked electrical, mechanical, optical and piezoelectric properties. The metallic properties are determined by the armchair nanotubes whereas chiral and zigzag nanotubes are either metallic if n-m = 3j (where j is an integer and m ≠ n) or semiconductors with other n and m values [64]. MWNTs are pondered as the metallic conductors. On the other hand, SWNTs are generally recognized to be a mixture of metallic and semiconducting nanotubes. Since metallic CNTs show very good electrical conductivity, they can support current density of 4 x 10^9 A/cm^2, relatively 1000 times more than that of silver [65]. Recently, CNTs are extremely attractive materials in the fields of electronic, energy and sensing applications owing to the wide range of electronic properties of CNTs based on their nanometer scale dimensions, inertness and robustness [66, 67].

1.3 Preparation of CNTs, extraction and modification:

Chemical vapor deposition, laser ablation and arc-discharge are the three main processes for the preparation of carbon nanotubes. The initial large scale synthesis process of SWNTs comes under laser ablation method developed by the Smalley group [67]. A pulsed laser is used in this procedure to vaporize a graphite/catalyst composite target in an inert environment of Ar or He. On the wall of reactor, the nanotubes are synthesized with other byproducts such as graphitic and amorphous carbon, particles of metal catalysts, and small fullerene molecules.

The first method used was arc-discharge for preparing SWNTs and MWNTs [67]. Ijima generated MWNTs using this method. CNTs, altering from 4 to 30 nm in diameter and highest 1 μm in length were re-discovered by Ijima on the negative end of carbon electrode related in the d. c. arc-discharge evaporation of carbon in an argon-filled vessel (100 torr). Although comparatively cheaper, the synthesized nanotubes under this method need further purification prior to use.

The more suitable method for synthesizing large quantities of CNTs is known as chemical vapor deposition (CVD). To generate MWNTs, Harris et al. [68] applied this process for the first time. When the decomposition of a gaseous hydrocarbon source (ethylene or acetylene) takes place in the presence of metal nanoparticles (Co or Fe) as a catalyst at medium temperature and over a comparatively longer period of time, the nanotubes are synthesized in this process. Since CVD is a more controllable and cost-effective method as compared to laser ablation and arc-discharge processes, this method is recognized as a superior for synthesizing large amounts of CNTs. However, due to the detection of side-wall defects, the quality of CNTs obtained by this method are reported as inferior [66].

All methods have problems in the synthesis of nanotubes, resulting in a mixture of nanotubes with various diameters, chiralities and length distribution. Similarly, metal catalyst residues,

carbonaceous impurities and other byproducts are associated with the synthesized nanotubes. Such contamination will reduce the overall yield of usable materials, so, it is necessary to remove such impurities. Various physical and chemical techniques are possible such as, high temperature annealing, oxidative acid treatment, solubilization and functionalization by surfactants comes under chemical techniques whereas physical methods cover chromatography, filtration, laser treatments and centrifugation [68]. Pure SWNTs can best be obtained by acid treatments/or gas phase oxidation. However, for avoiding the metal catalyst residues and enhancing the structural perfection, high temperature annealing is a highly effective for MWNTs synthesis under catalytic methods [68]. SWNT is a seamless cylinder containing only one layer whereas MWNT is cylindrical in shape having many concentric layers of graphene. We are using MWNTs as the support for all experiments in this dissertation.

Since CNTs appears to exist in the form of bundles owing to strong tube-to-tube van der Waals' interaction, they tend to be insoluble in almost all solvents. So, various attempts have been conducted to exfoliate and solubilize nanotubes. The application of surfactants with sonication, the end and/or side wall functionalization, protonation by super acids, and polymer wrapping of CNTs are various modification techniques. Such methods are able to improve solubility using different solvents and synthesize composite materials for many applications [69-71].

1.4 Electrochemical sensing using CNTs composite

Many compounds present in real biological samples may undergo reduction and oxidation processes at the same potential, resulting in fouling of the electrode and poor reproducibility and selectivity of the sensor. So, nanotubes must be modified with different functional groups to avoid such limitations. They can be attached with metal or metal oxide nanoparticles, enzymes and other nanomaterials. Tethering of nanotubes with other nanoparticles has enhanced the electrocatalytic

activity by hindering other interferences on the surface of the electrode [12]. The use of enzyme-based biosensors have been limited in recent years because of their critical demands on environmental conditions, high cost and instability of enzymes, low reproducibility and complex process in the synthesis [72]. Hence, the development of non-enzymatic sensors have been highlighted in recent research fields.

Different sensors have been fabricated using nanotubes with inorganic nanoparticles to analyze biologically important molecules. Such sensors have been an attractive tool for very good sensitivity and selectivity. Out of many strategies, the most common technique is to sonicate nanoparticles with nanotubes, or stir mechanically, or form the nanostructure directly by adsorbing proper precursors on the nanotubes with successive reactions. Similarly, using gas phase deposition, electroless or electrochemical deposition, nanoparticles are decorated on the surface of nanotubes for electrochemical sensing [73].

1.5 Electrochemical techniques for sensing

The earliest electrochemical sensor was discovered by P. Hersh in 1950 for monitoring oxygen [74]. The advancement in electrochemical sensors then began for analyzing hazardous chemicals for occupational safety and health administration (OSHA). Electrochemical sensors conduct by interacting with specific analytes and react by generating an electrical signal proportional to the analyte concentration. Various electrochemical methods have been emerged for electrochemical sensing such as potentiometry, amperometry and voltammetry [75]. Two groups such as static and dynamic techniques are the category of electrochemical methods. In a dynamic techniques, such as coulometry, amperometry, voltammetry and polarography, current is allowed to pass through the electrolyte solution. In the Static technique, no current is permitted to pass through electrolyte solution, such as potentiometry. The electrochemical process family tree is shown below. Among

these techniques, cyclic voltammetry and chronoamperometry are used in our research. These methods are relatively easy to study bioanalytes and the sensitivity of bioanalytes are observed with wider range. Large amplitudes permit measurement of current (CA) and voltage (CV) at a controlled potentials as shown in Figure 1.3.

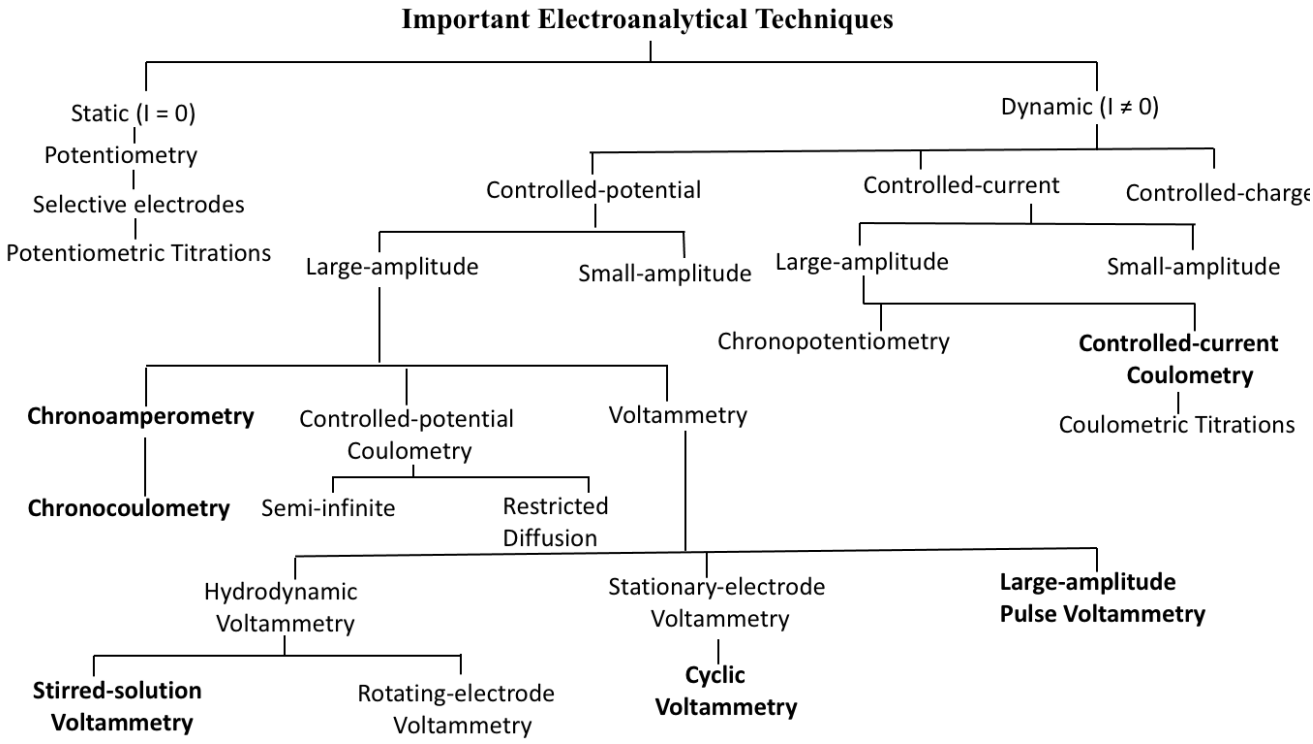

Figure 1.3: Electrochemical methods family tree (Adapted from reference 76)

1.5.1 Cyclic Voltammetry

One of the electrochemical techniques is cyclic voltammetry (CV), widely used in many areas. The potential of the working electrode is altered with time linearly in this versatile electroanalytical method, and the current obtained is determined as a function of applied potential.

As the potential is applied on the working electrode against the reference electrode, CV signal is obtained as an excitation signal. As a result, the resulting current as a response signal is earned.

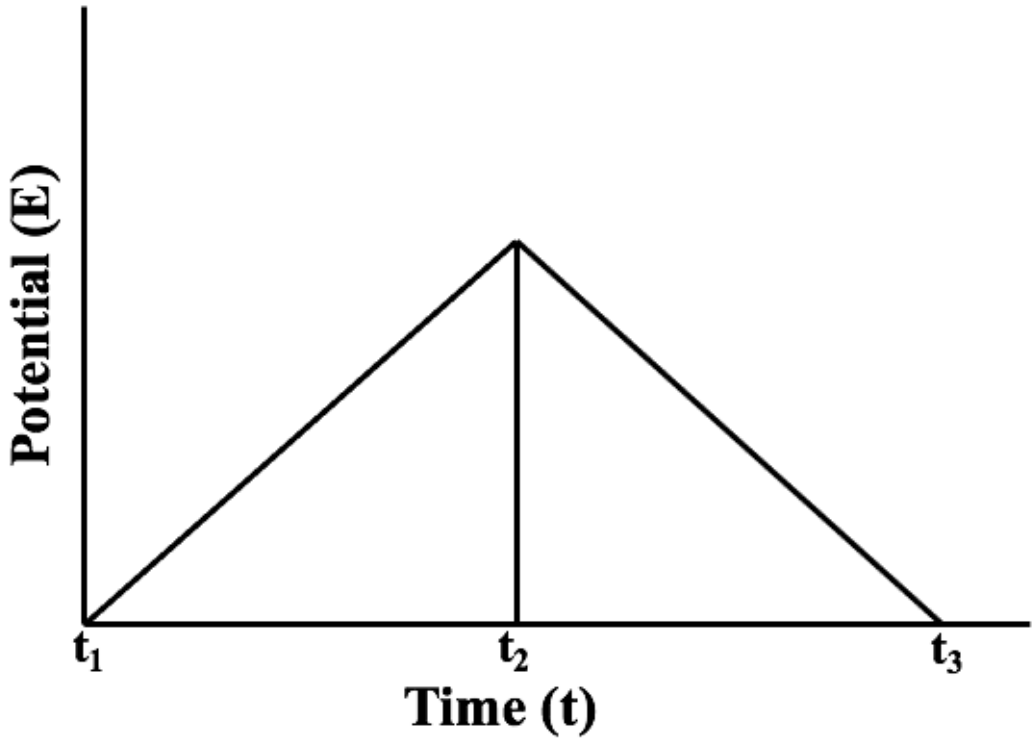

Figure 1.4: A triangular waveform, potential versus time.

Figure 1.4 describes the cyclic voltammogram excitation signal that is a scan of potential linearly with a waveform of triangle. Such characteristic feature of triangular voltage waveform is applied to the working electrode. When a potential scan is applied linearly between t_1 and t_2, the potential can be switched back to its starting value at time t_3. The current is calculated using the working electrode in the course of the potential scan so that a cyclic voltammogram is achieved. The voltammogram can be expressed by plotting the vertical axis with current versus the horizontal axis with potential. This horizontal axis is also considered as a time axis since the potential linearly changes with time.

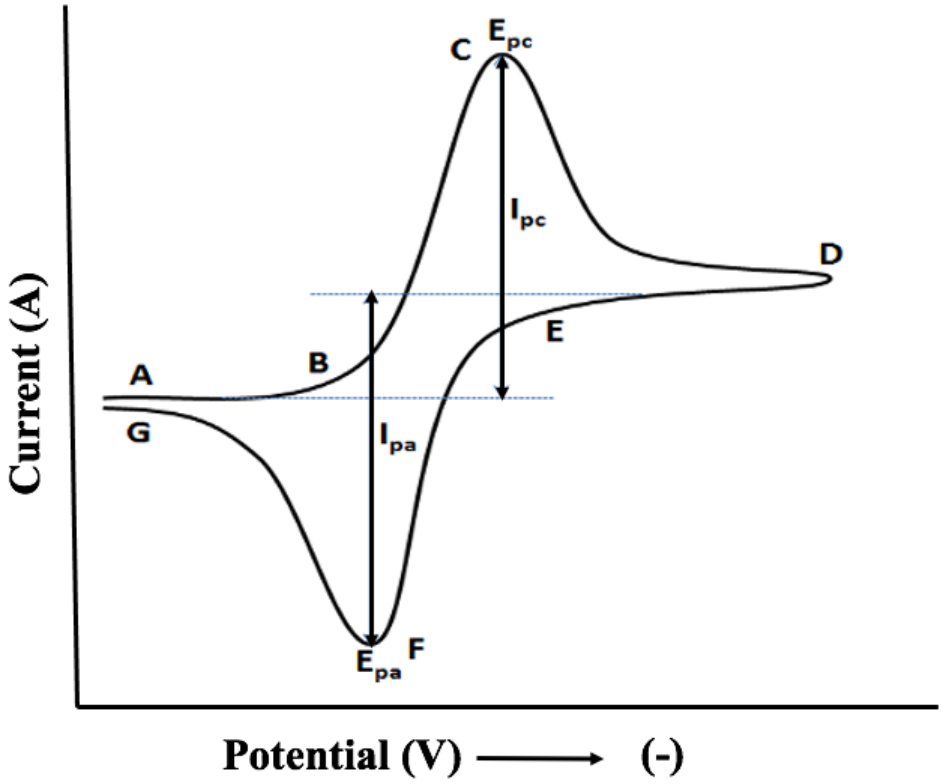

Figure 1.5: A schematic diagram of cyclic voltammogram (CV)

At the beginning, the working electrode under the influence of initial potential does not show any electrode reactions immediately. The potential is negatively noticed in forward direction. The current observed is very little at 'A' as the potential scan begins. The current starts to go up at point 'B' where the electroactive species can readily be reduced since the potential of the electrode is negative enough. An immediate increase of current appears between 'B' and 'C' because of the greater rate of reduction at more negative potential. The current is observed highest at point 'C'. However, since the amount of analyte on the electrode surface reduces fast, the current decreases from 'C' to 'D'. The current associated with the reduction potential goes down at more negative potentials due to exhaustion of analytes at the electrode. Hence, the rate of diffusion of reactants governs the current through the depleted layer of substances. Although analyte diffusion towards the electrode is considered to take place before reduction, the reduction in the current flow is found

between points ‘C’ and ‘D’ because reduction is faster than diffusion. To switch scanning, it is reversed to positive direction at ‘D’. As the potential is still sufficiently negative, a small cathodic current becomes active although the potential is scanning in the positive direction. The reduced species placed nearby the electrode begins to be oxidized providing in the increase of current in presence of high positive electrode potential at ‘E’. At this point, the rate of oxidation goes up at more positive potentials and the anodic current increases rapidly from ‘E’ to ‘F’ and it appears maximum at ‘F’. From ‘F’ to ‘G’, the current is reduced since the substance around the electrode is consumed of the reduced species. The complete first cycle is achieved when the analytes are reversed to their starting state ‘A’ as shown in Figure 1.5. Then the multiple cycles are resumed as required.

In cyclic voltammogram, the peak current (I_{pc}) of cathode, peak current (I_{pa}) anode, peak potential (E_{pc}) of cathode and peak potential (E_{pa}) of anode are reported to be very basic factors. When the transfer of electrons are rapid than that of other processes, such as diffusion, the number of electrons transferred in the electrode can be calculated from the splitting between the peak potentials.

$$\Delta E_p = [E_{pa} - E_{pc}] = \frac{2.303\ RT}{nF} \quad (3)$$

ΔE_p is $\frac{2.303\ RT}{nF}$ V at 25^0 C with n electrons for a reversible redox reaction. Due to the slow electron transfer rate for irreversible processes, the peak separation (ΔE_p) results in a greater value. For a reversible couple, the formal reduction potential (E^0) is explained as

$$E^0 = \frac{E_{pa}+E_{pc}}{2} \quad (4)$$

For a reversible systems at 25^0 C, the peak current (I_p) is directly proportional to the concentration of analyte according to the equation of Randles-Sevçik:

$$I_p = 2.686x10^5 n^{3/2} AC^o D^{1/2} v^{1/2} \quad (5)$$

where the area of the electrode is denotated by A (cm^2), the number of electrons is expressed by n, D is the coefficient of diffusion ($cm^2 \cdot S^{-1}$), C^0 is the concentration of analyte and V indicates the scan rate ($V \cdot s^{-1}$). This relationship is necessary in analytical use of CV.

Additionally, the individual peaks are splitted widely and reduced in height for irreversible methods (with sluggish electron transfer). The peak potential shift defines such systems with the enlarging scan rate. The given equation is applied to describe that the E_p is dependent on the scan rate:

$$E_p = E^\circ - \left(\frac{RT}{\alpha n_a F}\right)[0.78 - \ln(K^\circ/D)^{\frac{1}{2}}] + \ln\left(\frac{\alpha n_a F v}{RT}\right)^{\frac{1}{2}} \quad (6)$$

where V is the scan rate, α shows the transfer coefficient, n_a indicates the number of electrons included in the charge transfer step, K^0 is the standard rate constant. In irreversible system, the given equation is used for peak current and it shows that peak current is still consistent with the bulk current and $V^{1/2}$.

$$I_p = (2.99 \times 10^5)\, n\, (\alpha n)^{1/2} ACD^{1/2} v^{1/2} \quad (7)$$

Cyclic voltammetry is necessary to generate the excitation signal applying a wave form generator and to use this signal to an electrochemical cell by a potentiostat. It is also required to determine the resulting current by a current-to-voltage converter and to show the voltammogram using a recorder. In general, the main three objects are enclosed in an individual electronic device.

The three electrodes used for the voltammetric measurements in an electrochemical cell are (1) working electrode, (2) a reference electrode and (3) a counter electrode. They are kept in a solution having the analyte of interest and the supporting analyte (a surplus of a non-reactive electrolyte). The electrode where redox processes take place is called the working electrode. The electrode diameter is basically kept less than 5 mm so that its susceptibility to have polarized can be enhanced. Working electrodes are generally synthesized from conducting materials such as solid gold or Platinum, liquid mercury and various forms of carbon like graphite and glassy carbon. Mercury electrodes in the form of dropping mercury electrodes are constantly reused as a thin film plated onto metal substrate or a carbon or as a stationary hanging mercury drop electrode. Although the positive potential range is limited by the oxidation of mercury, mercury electrodes have been used for studying reduction processes in the past. The application of mercury electrodes are narrowed since it has environmental issue regarding to the mercury and its compounds. Hence, gold, solid platinum and carbon electrodes are most commonly accepted as the working electrode. Because of its expanded potential nature, physical and chemical stabilities, glassy carbon electrode (GCE) is widely recognized as a standard carbon electrode materials. The working electrode is GCE used in this dissertation research.

Another electrode is the reference electrode that offers an exact reference potential ideally against which the working electrode potential is measured. The commonly used references for voltammetric studies are saturated calomel electrode (SCE) or Ag/AgCl electrode in aqueous solution. However, calomel reference electrode (Hg/Hg_2Cl_2) was prohibited due to its environmental concern. The Ag/AgCl electrode is used in this research. The precise voltage of this reference electrode is reported to be +0.210 V.

The third electrode is the counter electrode. It is also pronounced as auxiliary electrode and it is generally a piece of platinum gauze or wire. It conducts electricity from the source of signal to the working electrode through the solution. It maintains the large current going through the reference electrode so that the potential of the electrode remains stable. [75, 77, 78].

1.5.2 Chronoamperometry

Chronoamperometry (CA) is a simple and a widely used electroanalytical technique in which the working electrode potential is stepped to a higher value resulting in Faradaic current. The resulting current is analyzed as a function of time. The Cottrell equation is used to describe the Faradaic current as shown below. This current is because of electron transfer between the electrode and the redox reaction of the target analyte.

$$I = \frac{\mathrm{nFA}C_y^0\sqrt{D_y}}{\sqrt{\pi t}} \tag{8}$$

where I is the current in amps, F is Faraday's constant (96, 485 C/mol), n is the number of electron transferred, D_y is the diffusion coefficient for species y in cm^2/s, C_y^0 indicates the initial concentration of reduce or oxidize able analyte in $mole/cm^3$, A is the projected area in cm^2, and t is the time in seconds. Using the slope of the plot I vs $t^{-1/2}$, the diffusion coefficient of the target analyte is calculated. Therefore, the Cottrell current plot shows an important diagnostic process to study whether the analyte of interest is freely diffusional in solution. When a solid electrode comes in a contact with a solution having an oxidized form of electroactive species, it creates a solid-liquid interface. The electrode reduces the neighboring molecules at the beginning which are then depleted as shown:

$$Ox + e^- \longrightarrow Red$$

Such disappearance causes a concentration gradient [79]. Figure 1.6a is the sketch of the waveform used in a potential step experiment. E_1 indicates the area where Faradaic process does not occur. The mass-transfer-limited region is shown by E_2 where the concentration of analyte on the electrode surface comes to zero. At the electrode surface, the current (flux) is proportional to the concentration gradient. The flux of the oxidized form of molecules is continued toward the electrode surface that causes the removal of the molecules in the bulk solution (Figure 1.6b). Finally, the slope of the concentration profiles decreases at the electrode surface with time as shown in Figure 1.6C.

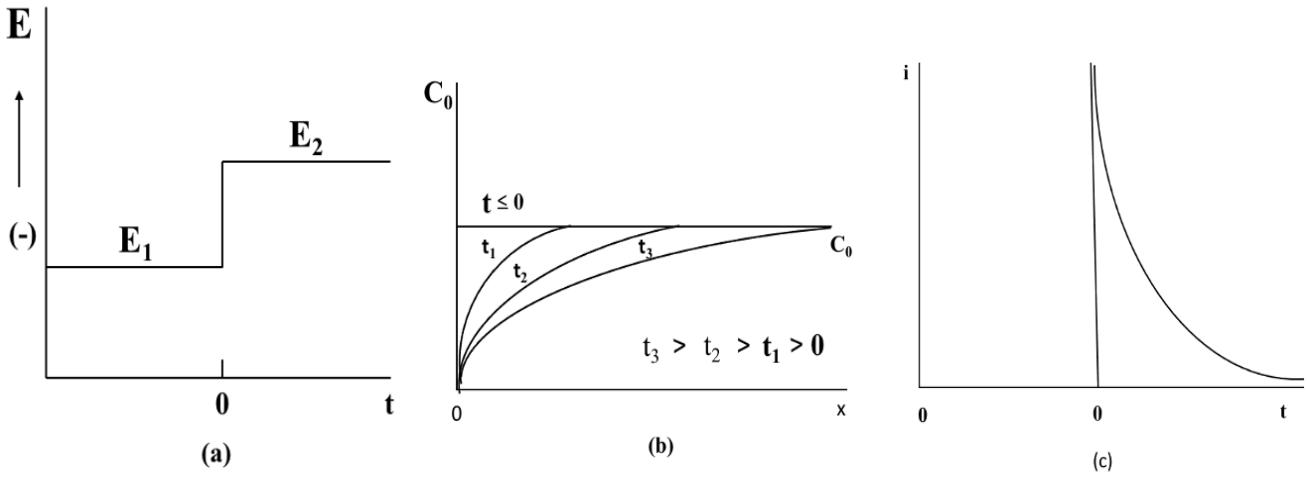

Figure 1.6: Chronoamperometry redox reaction conditions; (a) Waveform of potential step experiment where Ox species is electro-inactive at E_1, However, at a diffusion-limited rate at E_2, it is reduced; (b) concentration profiles for different times in the experiment; (c) current flow as a function of time.

1.6 Motivation and Research Objective

It is acknowledged that involving nanomaterials into electrochemical sensors has the potential for enhancement in sensitivity (two orders of magnitude) owing to large surface area which permits the enzyme immobilization and other materials [80]. Many efforts have been made to alter the surface of CNTs with different materials. Wayu et al. [32] were able to attach ZnO with

MWNTs to detect hydrogen peroxide. This modified electrode displays remarkable electrocatalytic activity and a stable response with H_2O_2. Li et al. [57] deposited PB on the gold surface using electrolysis process to detect H_2O_2 in micromolar range. PB is the iron complex compound which acts as catalyst. The Fe (II) and Fe(III) states present in PB is responsible to enhance redox activity with various bio-analytes. However, the notion regarding the attachment of PB with the composite of refluxed ZnO/MWNTs through point zero charge process has not been investigated. Detailed delineation of the impact of this composite on the changes in the chemical activity and electronic structures has not been described. Moreover, the biocompatibility of this resulting composite needs to be studied for *in vivo* uses. The proposed work seeks to correlate changes in the electrocatalytic activity of PB/ZnO/MWNTs composite for higher sensitivity and lower detection limit.

1.7 Scope of the Dissertation

The cost-effective method for designing and fabricating the sensitive and selective H_2O_2 sensor comes under the analysis of this dissertation. The characterized earth rich materials have been applied for detection of H_2O_2. The potential use of the fabricated sensor for *in situ* determination of H_2O_2 in cancer cells is explained. With the purpose of correlating NP-CNTs electrocatalytic activity with morphological structures, synthesis of the composite was achieved in three steps: (i) ZnO NPs were prepared by refluxing, which were then (ii) attached to COOH-MWNTs, and followed by (iii) PB electrostatic attachment to the COOH-MWNTs for H_2O_2 detection. This composite, PB/ZnO/COOH-MWNTs is characterized with various techniques, including scanning electron microscopy (SEM), transmission electron microscopy (TEM), X-ray photoelectron spectroscopy, Raman spectroscopy, fluorescence spectroscopy, enzyme-linked immune sorbent assays (ELISA). CV and CA are applied for the qualitative and quantitative

electrocatalytic properties related to morphology modification. Electrocatalytic improvements from the PB/ZnO/COOH-MWNTs nanocomposite morphological structures from the surface of COOH functional groups and attachment of ZnO NPs and PB were studied. Chapter 1 originates with a short overview of literature and selected nanomaterials: COOH-MWNTs, ZnO NPs and PB. The electrochemical techniques such as CV and CA are studied. Chapter 2 begins with the synthesis, fabrication and characterization of ZnO NPs and PB/ZnO/COOH-MWNTs structures. The refluxed synthesis method, surface characterization technique, point zero charge (PZC) experiments for enhancing electrocatalytic activity are investigated. Chapter 3 presents the biocompatibility of the developed sensor. The cytotoxicity of the synthesized composite on THP-1 cells is demonstrated. Chapter 4 addresses the selective detection of H_2O_2 at pH=7.0 phosphate buffer solutions. The effect of potential interferences such as UA, AA, APAP, and Glu is studied. It also discusses a real-world use of the fabricated sensor. The developed sensor for *in situ* monitoring H_2O_2 in BT20 and 4T1 cancer cells was studied. The result of CA is compared with that of ELISA for detection of H_2O_2 in these cells. Chapter 5 discusses application of the sensing composite to investigate the relationship of apoptosis with oxidative stress in BT20 cancer cells by flow cytometer. Chapter 6 and 7 explains the versatile capability of our sensor to study dopamine, and homovanillic acid. The coalescence of ZnO nanoparticles under SEM analysis is the interesting findings in this dissertation mentioned below.

Chapter 2

Synthesis and characterization of the PB/ZnO/COOH-MWNTs nanocomposite

Abstract

The reflux synthesis of zinc oxide (ZnO) nanoparticles was performed. After tethering refluxed ZnO to carboxylic acid functionalized multiwalled carbon nanotubes (COOH-MWNTs), an electrochemical sensing composite was produced by electrostatically attaching Prussian Blue on the surface of ZnO/COOH-MWNTs. The point zero charge (PZC) was explained how it plays role to enhance the sensitivity of H_2O_2. The size and morphology of ZnO nanoparticles are studied under TEM and EDX. ZnO/COOH-MWNTs nanocomposites were explained by FTIR whereas PB/ZnO/COOH-MWNTs were characterized by SEM, EDS and XPS. High electrocatalytic activity for H_2O_2 was obtained when PB was successfully attached on the ZnO/COOH-MWNTs. The diffusion controlled experiment was performed using PB/ZnO/COOH-MWNTs sensor.

2.1 Introduction

As the particle size decreases down to 1-100 nm in diameter, the surface structure and morphology of substances alters becoming nanomaterials. Modification of surface structure and morphology of nanomaterials is of great influence for uses in the highly emerging areas of nanotechnology. The real challenge in the field of nanoscale science is the facile methods for generating nanomaterials with controlled morphology and surface properties because the electronic, catalytic and optical properties of the nanomaterials are studied by these factors.

Nanomaterials are highly applicable for fabrication of noble and improved electrochemical sensors and biosensors because of their unique physical and chemical properties [81].

Modified carbon nanotubes (COOH-MWNTs) is one of the newly growing nanomaterials which are getting more attention these days for electrochemical sensing. Using various chemical reaction methods, scientists were able to tether COOH-MWNTs with different metal oxides for their applications in many fields. For example, ultrasonic irradiation with acid treated SWNTs, zinc acetate and triethanolamine in aqueous phase processing at low temperature was used by Lin et al. to design uniform coating of SWNTs. This composite, ZnO/SWNTs increased the electron transport and optical properties of SWNTs [82]. MWNTs were attached with atomic layer deposition of ZnO and they were annealed under N_2 gas at 900^o C. ZnO coating MWNTs composite increased optical and electron field-emission properties of MWNTs [83]. Vijayalakshmi et al. fabricated MnO_2/MWNTs/Ta composite using electron beam evaporation and spray deposition process for the analysis of H_2O_2 in milk [84]. Ping et al. developed an amperometric sensor based on PB and poly (O-phenylenediamine) modified GCE for the quantification of H_2O_2 in beverages [85]. Wei et al. reported the design of Hb/ZnO-MWNTs/Nafion film and direct electron transfer between Hb and ZnO/MWNTs/Nafion takes place due to their synergic effect to enhance the electrocatalytic activity of H_2O_2 [86]. Synthesis of ZnO nanoparticles generally appears as needle-like and flower like shapes. Such shapes are not easy to control [87-89]. In our study, the morphology of ZnO nanoparticles, however, were controlled by reflux synthesis method by changing the synthesis temperature before attaching to the functionalized MWNTs. The point zero charge concept is used to attach PB with the composite of ZnO/MWNTs. An electrocatalyst composite consisting of refluxed zinc oxide nanoparticles (NPs) attached to carboxylic acid-functionalized multiwalled carbon nanotubes (ZnO/COOH-

MWNTs) was electrostatically tethered to PB to further enhance the sensitivity and selectivity of H_2O_2 for the first time in this work.

2.2 Materials and Methods

The following chemicals are used in the study without any modifications

i) Multiwalled carbon nanotubes, MWNTs 95%, (30±10) nm (Nanolab Inc. 22 Bedford street, Waltham, MA 02453)

ii) Hydrogen peroxide (Fisher Scientific, Fair Lawn, New Jersey, USA)

iii) Nafion (Ion power, Inc., St. Louis, MO, USA)

iv) Sodium Hydroxide, NaOH (Fisher Scientific, Fair Lawn, New Jersey, USA)

v) Zinc Nitrate hexahydrate, 98%, Zn(NO3)2.6H2O (Sigma-Adrich, St. Louis, MO, USA)

vi) Hydrochloric acid (Fisher Scientific)

vii) Alumina slurry 0.05 µm, 1.0 µm (Buehler Lake Bluff, IL, USA)

viii) Uric acid 99% crystalline (Sigma Aldrich, St. Louis, MO, USA)

ix) L-ascorbic acid, 99% (Sigma Adrich, St. Louis, MO, USA)

x) Folic acid, 97% (Sigma-Aldrich, St. Louis, MO, USA)

xi) 4-acetamidophenol, 98% (Sigma Aldrich, St. Louis, MO, USA)

xii) Phosphate buffer solutions, PBS, pH 7.0 (Sigma-Adrich, St. Louis, MO, USA)

xiii) Hydrogen peroxide (Fisher Scientific, Fair Lawn, New Jersey, USA)

xiv) Glucose 96% (Sigma-Aldrich, St. Louis, MO, USA)

2.3 Synthesis of refluxed Zinc oxide nanoparticles

In this research, ZnO nanoparticles were synthesized by the refluxed process following a procedure developed by Feng et al [90]. For the first hour, 0.50 M of 42.0 mL $Zn(NO_3)_2.6H_2O$ solution was added into the 1.00 M of 42.0 mL NaOH solution in a boiling flask with constant stirring continuously. These two mixtures were mixed under refluxed method in an inert N_2 atmosphere for another 2 hrs at 90^0 C as shown in Figure 2.1. with the appearance of white precipitate, ZnO nanoparticles were collected and made them pure by washing with ultrapure water. Several washing and using centrifugation process were continued for the purification of the sample. Finally, the obtained ZnO nanoparticles were dried in the desiccator for overnight. Such particles were again dried in an oven for 1 hour at 65^0 C.

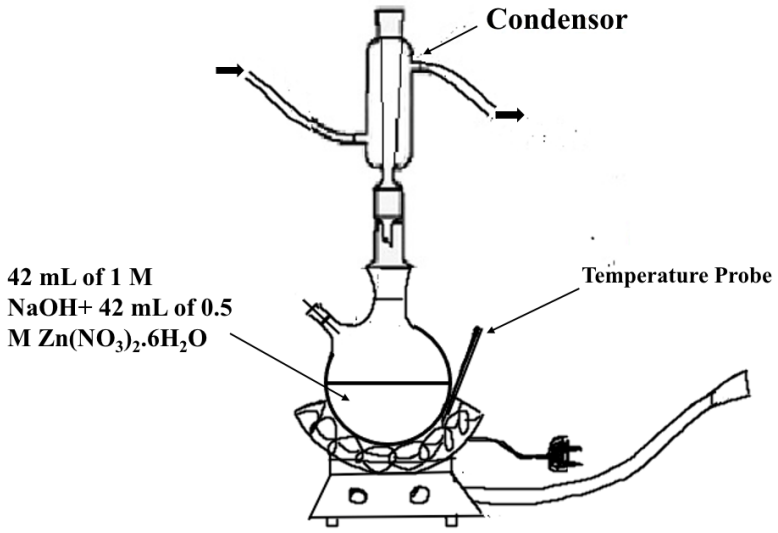

Figure 2.1: The set up for the synthesis of ZnO nanoparticles by reflux process under inert N_2 gas condition.

2.4 Fabrication of refluxed PB/ZnO/COOH-MWNTs nanocomposites

Bamboo structured COOH-MWNTs (95% purity, 30 nm diam.) were obtained from Nanolab, Inc. (Waltham, MA, USA) and used as received. A 4.0 mg of refluxed ZnO and 4.0 mg of COOH-MWNTs were taken into 2.0 mL vial. Then, 1.0 mL of absolute anhydrous ethyl alcohol was casted into the vial to form the suspension. The suspension was kept into sonicator for 1 hr to disperse ZnO and COOH-MWNTs. The composite, ZnO/COOH-MWNTs was dried in oven at 80^0 C. After complete dry of ZnO/COOH-MWNTs, this composite was dried in dessicator for 24 hours. Then, 4.0 mg of ZnO/COOH-MWNTs were mixed with 2.0 mg of Prussian blue (PB) in PBS at pH 6.6. The mixture was stirred for 5 hours to attach PB on the surface of the composite, ZnO/COOH-MWNTs.

2.5 Preparation of Nafion/PB/ZnO/COOH-MWNTs/GCE sensor

Prior to modification, the GCE was polished using a 1.0-µm diam Al_2O_3 slurry (Buehler Ltd, Lake Bluff, IL, USA), and then further polished using a 0.05-µm diam Al_2O_3 slurry to obtain a mirror like finish. Doubly-distilled deionized 18 MΩ Millipore water (Milli-Q water filtration system, Model ELix, USA) was used to rinse the electrodes. The GCEs were then cleaned by sonication in a 1:1 volume mixture of concentrated HNO_3:H_2O for 5 min. The electrodes were then dried at room temperature. Each PB/ZnO/COOH-MWNT nanocomposite was drop-casted onto glassy carbon electrodes (GCE), 3 mm in diam. A 5-µL colloidal aliquot of the composite as a colloidal suspension was pipetted on the cleaned GCE surface. The GCE was then kept in the oven for 20 min at 80^o C. After drying, a second 10-µL aliquot of 2% Nafion^{TM} solution was applied to the top-most layer of the composite onto the GCE, and then dried in an oven at 80^o C for additional 12 min to obtain the PB/ZnO/COOH-MWNTs/GCE working electrode for electrochemical sensing.

2.6 Surface characterization of ZnO nanostructure and ZnO/COOH-MWNTs composite and PB/ZnO/COOH-MWNTs

Morphology and diameter size of ZnO, ZnO/COOH-MWNTs and PB/ZnO/COOH-MWNTs were characterized using scanning electron microscopy (SEM), transmission electron microscopy (TEM), Fourier transform infrared spectroscopy (FTIR), energy dispersive X-ray spectroscopy (EDX) and X-ray photoelectron spectroscopy (XPS). TEM study of the ZnO nanoparticles and ZnO/COOH-MWNTs composite was conducted using a JEOL 1400 transmission electron microscope. ZnO and ZnO/COOH-MWNT samples for TEM images were designed by using a droplet on 200 mesh carbon-coated Cu TEM grids (SPI supplies, west chester, PA, USA). EDX is used to analyze the ZnO nanoparticles. The TEM data were analyzed using image J version 1.38x software National Institute of Health (NIH) (http://rsbweb.nih.gov/ij/download.html).

Point-of-zero charge experiments were conducted by applying 12 various pH solutions. Different pH solutions were prepared in the range from 1 through 12 with the help of HCl and NaOH solution. The initial pH values were determined after 30 minutes when 2.0 mL of these solutions were kept in 12 various Nalgene cryogenic vials. Then, 2.0 mg of the experimental sample was added in each vial and shaked well with the solutions. After 16 hours, the final pH values of the solution were measured. The initial pH versus final pH values were plotted to calculate the PZC. A pH meter with spear tip electrode was used for PZC measurements.

2.7 Results and Discussion

The morphology and diameter size of ZnO nanoparticles were maintained by reflux synthesis process. The purity of the synthesized ZnO nanoparticles were studied by TEM, EDX and XPS

techniques. TEM image of synthesized ZnO nanoparticles is shown in Figure 2.2. Figure 2.2 displays a characteristic image of an electrodeposited ZnO films. The C, O and Zn are emanated from the ZnO powder surface confirming its reflux synthesis. EDS of the ZnO nanostructure refluxed synthesis from 0.5 M $Zn(NO_3)_2.6H_2O$ showed a high percentage of Zn present in the sample [91].

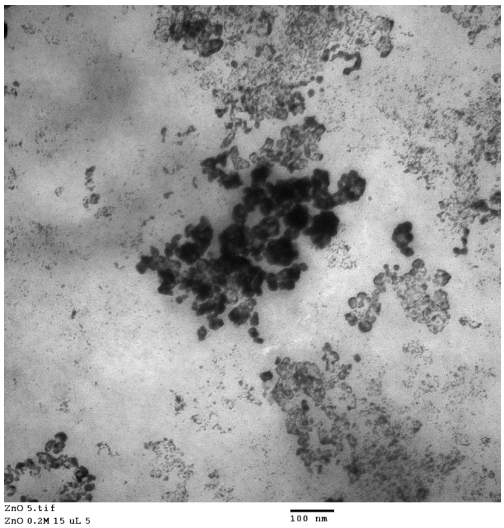

Figure 2.2: TEM image of refluxed ZnO nanoparticles
Reproduced with permission from ref. [29]. Copyright 2019, American Chemical Society

The functionalized multi-walled carbon nanotubes (MWNTs) were attached to ZnO nanoparticles, thereby, synthesizing carbon zinc oxide composite with enhanced sensitivity properties. These MWNTs were acquired and used as received. In the initial analysis, when the

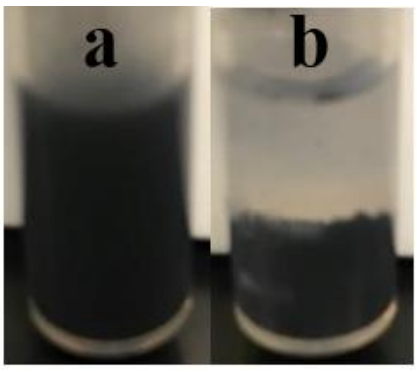

COOH functionalized MWNT was attached with ZnO nanoparticles using ultrasonication process, the density of the composite was changed. After 1 hr of sonication, COOH moieties of MWNT provide buoyancy, remaining uniformly dispersed and

Figure 2.3: Effect of sonication on the reaction of ZnO nanoparticle with COOH-MWNTs (a) COOH-MWNTs and (b) ZnO/COOH-MWNTs in absolute anhydrous ethyl alcohol after 1 hr sonication

suspended in absolute anhydrous ethyl alcohol (AAEA) solution.

However, the buoyancy of MWNT nanocomposite markedly decreases when ZnO nanoparticles were introduced to the system. The composite ZnO displayed the sedimentation within 5-10 min after 1 hr sonication as shown in Figure 2.3b. This indicates that ZnO nanoparticles are tethered well to MWNTs for enhancing electrocatalytic activity.

Figure 2.4 displays the ATR-IR spectra of ZnO/COOH-MWNTs nanocomposites produced by reflux process. ATR-IR results show that the peak diminished in the range from (1641-1691) cm^{-1} is also showing that the COOH functional group and the ZnO nanostructure are in the attachment into the nanotubes. The peaks at 1641 cm^{-1} is due to the C=C stretching vibration of the COOH-MWNTs graphene backbone [92]. Another peak at 1691 cm^{-1} is because of C=O stretching vibration of COOH group [92]. The C=O stretch disappeared since it is involved in attachment of ZnO nanoparticles. This proved to be the deflection of ZnO on MWNTs.

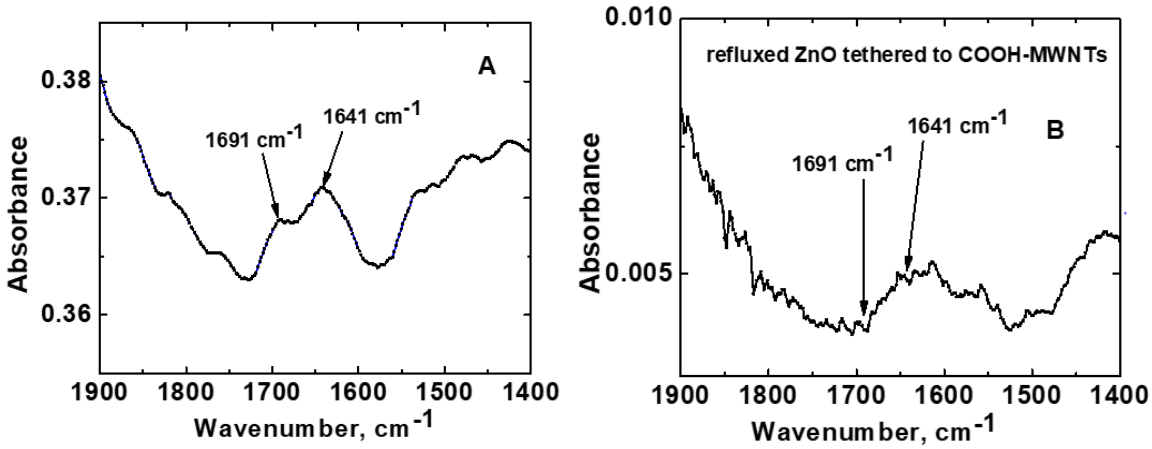

Figure 2.4: ATR-IR spectra of (A) COOH-MWNTs and (B) refluxed ZnO tethered to COOH-MWNTs in the range from 1900-1400 cm^{-1}[92]. Reproduced with permission. Copyright 2015, Wiley Analytical Science

Figure 2.5A shows the TEM images of ZnO/MWNTs. MWNTs look like the film with an average diameter of 30 nm. However, ZnO was deposited on and tethered to the outside of MWNTs as nanoparticle of ~ 13 nm as obtained from Figure 2.5B histogram analysis.

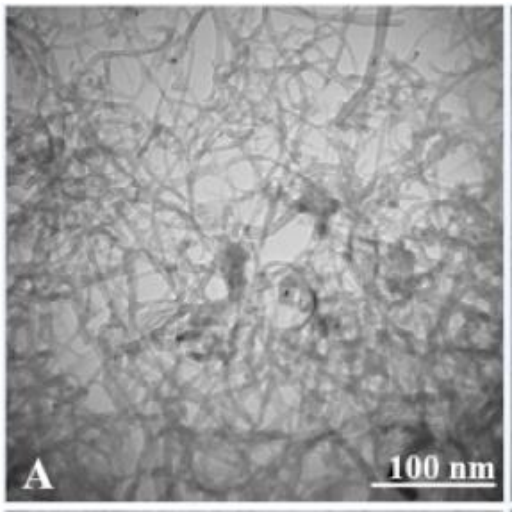

Figure 2.5A: TEM image of refluxed ZnO/ COOH-MWNTs.

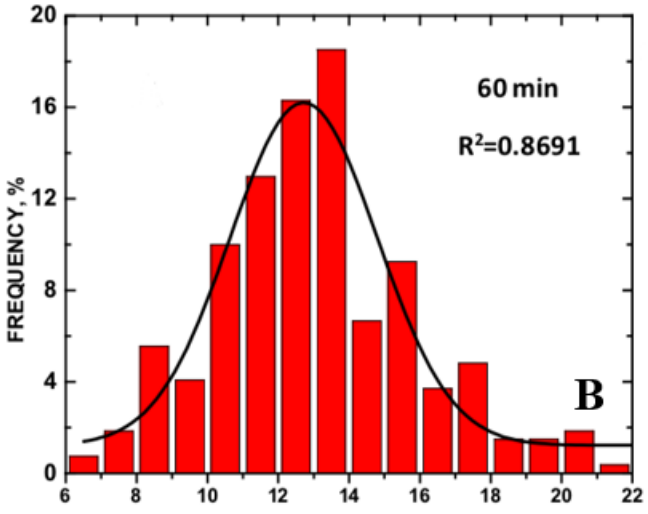

Figure 2.5B: Histogram showing the refluxed ZnO with average 13 nm in diameter (n = 576).

Reproduced with permission from ref. [29]. Copyright 2019, American Chemical Society

Figure 2.5A indicates the homogeneous morphology showing that ZnO nanoparticles are uniformly distributed in the MWNT.

2.7.1 Determination of point zero charge (PZC)

PZC measurement is used to attach PB on the surface of ZnO/COOH-MWNTs. PZC is the pH value at which the solid surface is electrostatically neutral in aqueous solution. The PZC is usually measured with respect to the pH of the electrolyte and ultimately assigned the PZC of a given substrate or particles. In addition, the pH of a solution lower than the PZC value of the materials generates the acidic solution, denoting more protons than hydroxide groups and the adsorbent surface is charged positively attracting anions. However, the pH solution higher than the PZC value shows the basic solution with more hydroxide groups, resulting in the negatively charged surface adsorbents on the solid surface which attract cations, according with the Guoy Chapman theory [93]. The PZC experiments were conducted to study the tethering of PB to the ZnO/COOH-MWNTs. Such PZC study was performed by using the Park and Regalbuto procedure [94]. The experimental results displaying the point of zero charge of refluxed ZnO/COOH-MWNTs and PB are shown in Figure 2.6. The PZC values of refluxed ZnO/COOH-MWNTs and PB were measured and found to be 7.3 and 6.0, respectively. The PZC value for the refluxed ZnO only was also found to be 7.2. The PZC values for both refluxed ZnO and refluxed ZnO/COOH-MWNTs composites were studied to be almost same. The agreement in the similarity of PZC measurements indicates that the COOH-MWNTs surface is covered by ZnO nanoparticles. This value also shows that the refluxed ZnO nanoparticles are associated with the attachment of COOH functional groups [91]. Due to the differences in PZC values of ZnO/COOH-MWNTs and PB, PB was attached on the surface of ZnO/COOH-MWNTs using the PBS of pH 6.6. In this case, PB adopted a negative charge whereas ZnO/COOH-MWNTs adopted a positive charge when they were kept in PBS of pH 6.6. Due to the electrostatic attraction between these oppositely charged

nanocomposite and PB, PB were successfully tethered on the surface of ZnO/COOH-MWNTs to enhance the sensitivity of H_2O_2.

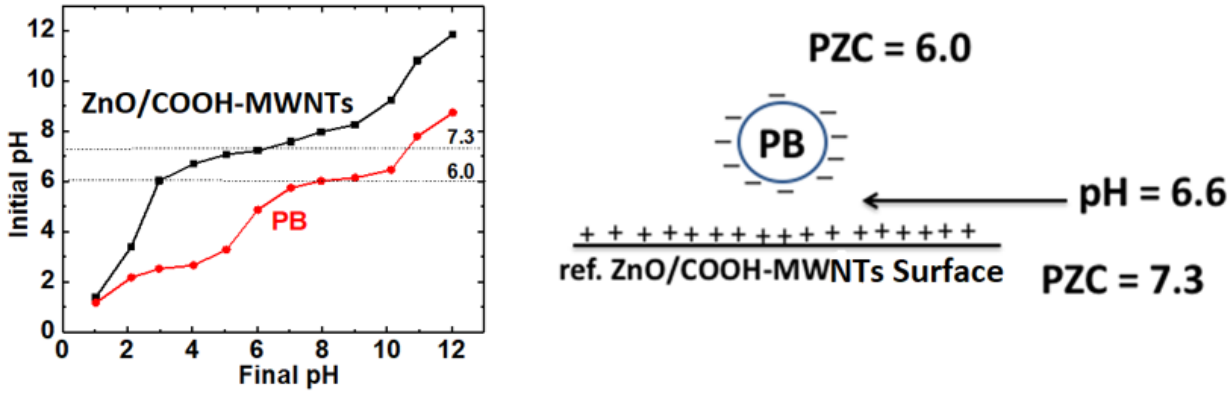

Figure 2.6: The determination of PZC of ZnO/MWNTs and PB (right), A scheme of attaching PB with the composite, ZnO/MWNTs using PZC (left). Reproduced with permission from ref. [29]. Copyright 2019, American Chemical Society

Figure 2.7 shows the schematic diagram of how PB is able to enhance the sensitivity of H_2O_2.

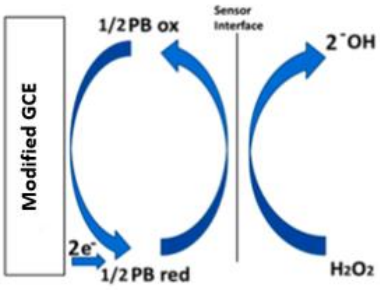

$$K_4Fe_4^{II}[Fe^{II}(CN)_6]_3 + 2\,H_2O_2 \leftrightarrows Fe_4^{III}[Fe^{II}(CN)]_6 + 4OH^- + 4K^+$$

$$H_2O_2 + 2e^- \rightarrow 2OH^-$$

Figure 2.7: Schematic diagram showing the influence of PB with H_2O_2 to enhance sensitivity.

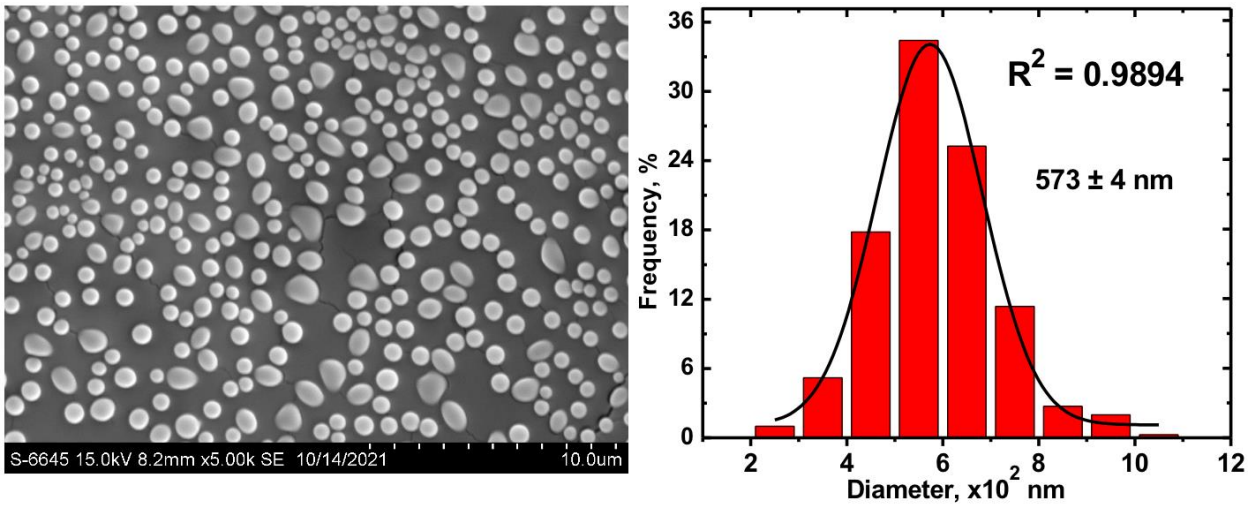

Figure 2.8: SEM image of Nafion/PB/ZnO/COOH-MWNTs deposited onto the working GCE surface

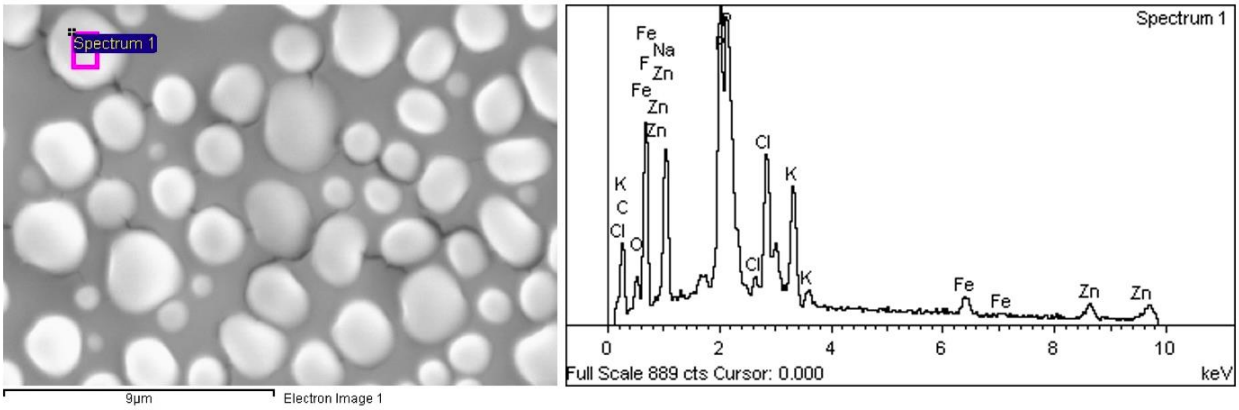

Figure 2.9: Energy dispersive X-ray spectroscopy of the Nafion/PB/ZnO/COOH-MWNTs

Figure 2.8 shows an SEM of the optimized composite deposited onto the glassy carbon electrode used for the DA sensing. The average diameter of the ZnO particles of 573 ± 4 nm (n = 504) resulted from the introduction of the PB to the ZnO/COOH-MWNTs. In contrast, the ZnO/COOH-MWNTs had a diameter of 12.7 ± 0.1 nm as we reported previously. Figure 2.9 shows the accompanying EDX of this same surface, focused on a representative particle encapsulated on the working electrode surface. Elemental atomic percentages from the EDX (based on the L edge for Zn and the K edge for the remaining elements) were 27% C, 7.61% O, 35.36% F, 8.87% Na, 8.06% P, 1.92% Cl, 6.48% K, 2.65% Fe and 1.92% Zn. In contrast, EDX

probes more deeply into the bulk. The fluorine emanates from the Nafion film used to bind the PB/ZnO/COOH-MWNTs to the GCE surface. Na, P, Cl, and K are consistent with spectator ions in the solution preparation for the composite. Differences in atomic percentages obtained from EDX and XPS are due to variations in surface sensitivity thus permitting insight into the structure of the topmost surface of the electrode material. Note that XPS is sensitive only to the top-most 50-100 Å; entities deeper into the bulk are invisible to the technique [95]. In contrast, EDX probes deeply into the bulk. It is hypothesized that ZnO is getting electron density from PB as Fe^{+2} is converted into Fe^{+3} in the composite. When PB was attached with ZnO/COOH-MWNTs, there is possibility of generating negative surface on ZnO and Fe atom exposes +ve charge on the surface of composite. Such scenario may be the driving force for the coalescence of the ZnO particles as shown in the SEM image of PB/ZnO/COOH-MWNTs.

X-ray photoelectron spectra (XPS) were acquired using a Perkin-Elmer PHI 560 system with a double-pass cylindrical mirror analyzer operated using a Mg Kα anode with a hν = 1253.6 eV photon energy operated at 250 Watts and 13 kV. The binding energy (BE) for the C 1s level at 284.4 eV, indicating adventitious carbon [96], was used for charge referencing. XPS peaks were curvefitted using 70%-to-30% Gaussian-Lorentzian lineshapes with Shirley and Touggard background subtractions [97]. BE peak envelopes were deconvoluted using CasaXPS ver. 2.2.107 (Devonshire, UK) software. ZnO, ZnO/COOH-MWNTs and PB/ZnO/COOH-MWNTs were mounted as a powder onto a custom-built sample holders and inserted into the XPS system via turbopumped antechamber in separate experiments and outgassed in a turbopumped antechamber prior to scans. Tantalum (Ta) was used as holder or probe for the materials. No signal was observed from the Ta 4f orbitals, indicating that the foil sample holder was completely covered.

System pressure did not exceed 1 x 10^{-8} Torr during scans. Core level intensities of the O 1s, C 1s and N 1s orbitals were normalized using their known atomic sensitivity factors [98].

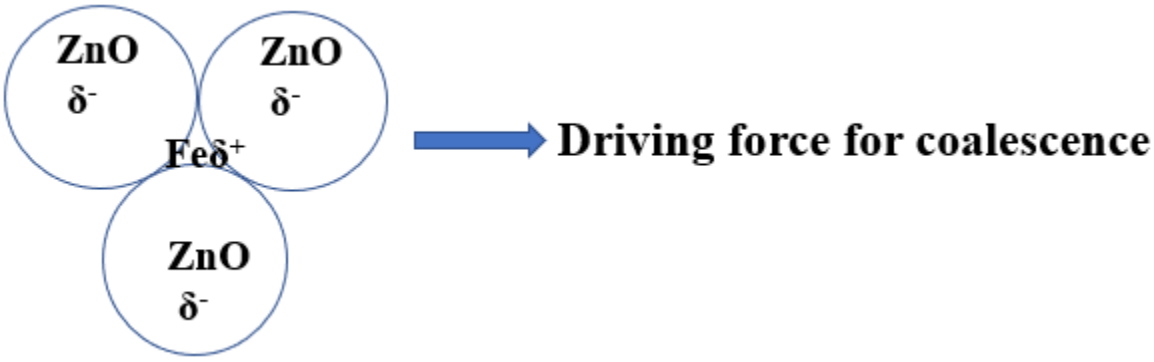

Scheme 2.1: Possible mechanism for the coalescence of ZnO nanoparticles as shown in SEM image.

We hypothesize the ZnO clusters in the SEM image are due to the electrostatic attraction between number of ZnO nanoparticles in presence of Fe ions as shown in Scheme 2.1. Various loading of PB with the ZnO/COOH-MWNTs can be hypothesized to determine the size of coalescence under possible SEM experiments. In our XPS results, the addition of PB on ZnO cluster lowers the binding energy. It means PB increases electron density on the surface of ZnO. This is basically justified the Scheme 2.1. Therefore, agglomeration of ZnO nanoparticles may be electrostatically driven. In addition, the relative peak area intensity of O 1s of ZnO at 530.2 eV was increased while that of O 1s of ester bond at 532.2 eV was observed lower with the introduction of PB as shown in figure 2.10, suggesting the reason for the bigger coalescence of ZnO particles. Randles-Sevçik analysis indicates a greater electroactive surface area of PB/ZnO/COOH-MWNTs (3.44 times more) compared to ZnO/COOH-MWNTs (as shown in Appendix C). The higher sensitivity of the composite may be due to the crevices present in the coalescence of ZnO nanoparticles in which case SEM is not able to observe such crevices.

Our XPS data shows elemental atomic percentages of 17.2% C, 82.5% O, 0.25% Zn and 0.04% Fe. It should be noted that the XPS sample scanned did not contain Nafion to permit analysis of the Fe, which would have been completely obscured due to photoelectron attenuation by its top overlayers. In comparing the two elemental EDX and XPS data sets the only elements free of artifacts, namely the Nafion, are Fe and Zn. In normalizing the Zn signal to Fe by dividing atomic percentages, the Zn/Fe ratio from EDX (0.724) and XPS (6.25) can be obtained. The markedly higher Zn signal (6-fold) from XPS as compared to EDX thus indicates a dominance of Zn at the topmost surface of the electrode, consistent with ZnO particles. Furthermore, the core level shifts of the O 1s and Zn 2p orbitals also verify the expected chemical oxidation states to be found for ZnO particles. Hence, the elemental composition data in conjunction with SEM indicate a coalescence of the ZnO nanoparticles into the larger ZnO clusters (574 nm diameter) after introduction of the PB to the ZnO/COOH-MWNTs with ZnO particles 12.7 nm in diameter.

The precise mechanism for the coalescence is not well understood and is a subject for ongoing investigation. The mechanism involves a charge transfer to the Zn atoms indicated by the XPS data. There is a negative 0.5-to-0.8 eV shift towards the lower binding energy in both of the Zn 2p orbitals upon introduction of the PB, denoting an increase in electron density in the ZnO surface (Figure 2.11). There is also an accompanying shift in the Fe 2p orbitals, for instance from 710.0 eV to 707.6 eV when comparing Fe in the free unattached PB and that attached to the ZnO/COOH-MWNTs, indicating attachment of Fe on the surface of ZnO in the composite. Since the trends in the Fe and Zn core level shifts are in the same direction, we can rule out redox activity between the PB and ZnO/COOH-MWNT as being the driving force for the agglomeration. What is definitive, however, is that that the PB is chemically bound to the ZnO particles such that it migrates into the bulk of the material as indicated by the Zn 2p chemical shift. The relative ratio

of the ZnO to COOH-MWNTs, using the integrated O 1s peak envelope areas comparing core level shifts at 530.2 eV, denoting ZnO (60.1%) [99] and at ~532 eV denoting COOH-MWNTs (39.9%) [32], indicating that the ratio of the ZnO:COOH-MWNTs is 3:2 (Figure 2.11). Hence, the majority of oxygen detected is from ZnO particles. This finding is also consistent with ZnO particles which are a majority of the surface species on the electrode surface. In addition, under XPS study, the chemical composition and information about oxidation states of ions in the PB/ZnO/COOH-MWNTs nanocomposite were reported. The spectra of the Zn $2p_{3/2}$, Zn $2p_{1/2}$ and Fe 2p were fitted to 70:30 Gaussian-Lorentzian peaks applying a Tougaard background substraction.

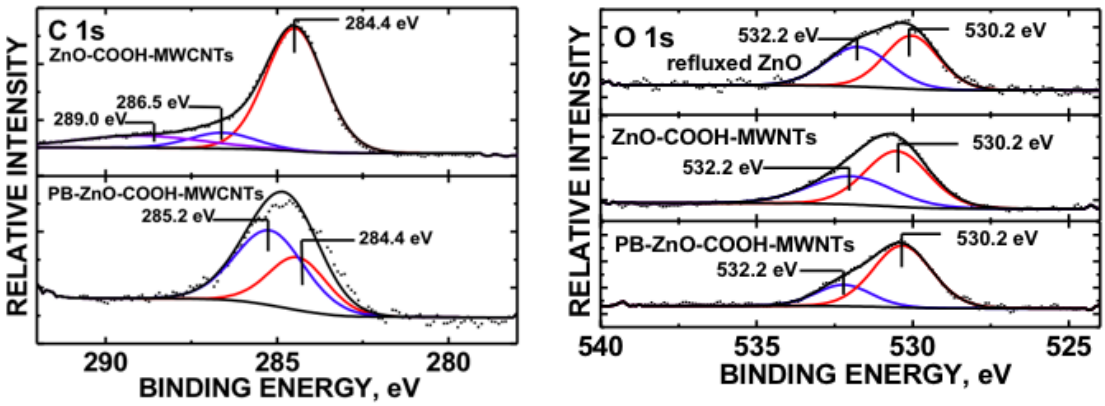

Figure 2.10: XPS analysis of C 1s and O 1s of various composites as shown in above figures
Reproduced with permission from ref. [29]. Copyright 2019, American Chemical Society

Figure 2.10 C 1s shows 284.4 eV of sp^2 C-C bond in the graphite of CNTs [100, 101] in XPS analysis along with the C 1s atoms present in the ester bonds [101, 102] represented by other binding energies. This indicates that functionalized MWNTs are attached with ZnO nanoparticles. Figure 2.10 O 1s displays 530.2 eV of O 1s from ZnO [99] and other binding energies indicate the O 1s from ester bond of oxygen [103].

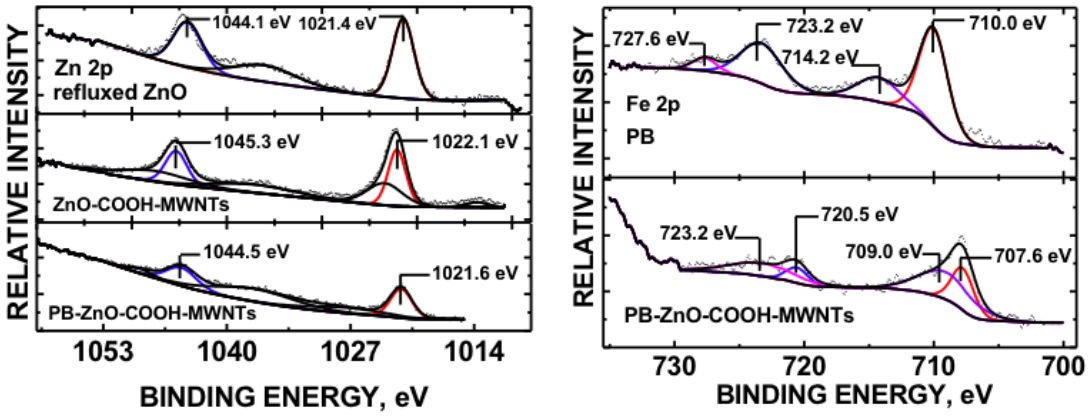

Fig. 2.11: XPS analysis of Zn 2p and Fe 2p of various composites as shown in above figures Reproduced with permission from ref. [29]. Copyright 2019, American Chemical Society

Figure 2.11 Zn 2p indicates the $2p_{1/2}$ orbital at higher potential and $2p_{3/2}$ orbital at lower potential with spin orbit coupling. The doublet separation value (~23 eV) between these peaks shows Zn 2p from ZnO [104]. The peak positions of Zn 2p at 1021.4 eV and 1044.1 eV in ZnO nanoparticles are shifted to higher binding energies to 1022.1 eV and 1045.3 eV, respectively in ZnO-MWNTs. This explains the shift to higher binding energy to the withdrawal of electrons from ZnO by the electronegative oxygen of the COOH-MWNT, showing the involvement of O-containing groups in the development of composite [100, 105]. It is observed that the chemical shift moves towards lower binding energies, 1021.6 eV and 1044.5 eV from 1022.1 eV and 1045.3 eV, respectively with the attachment of PB. Similarly, Figure 2.11 Fe 2p explains the significant change of chemical shift in lower binding energy of PB. This concludes that the lower binding energy effect due to the attachment of PB to ZnO/MWNT describes the electron rich morphology of the composite, correlating with higher electrocatalytic activity.

Diffusion of analyte ensures that direct electronic signal comes from chemical signal so that we can quantify the amount of analytes present in the solution accurately. The rationale for Randles-Sevçik analysis is to observe the diffusion of analytes in aqueous conditions under the influence of potential. Electrocatalytic activity of H_2O_2 was studied due to the effect of scan rate

on PB/ZnO/COOH-MWNTs. Cyclic voltammograms of 5 mM H_2O_2 in 70 mM PBS with saturated N_2 at pH 7.0 was shown in Figure 2.12. This CV was studied at various scans of 10, 20, 30, 40, 50, 60, 70, 80, 90, 100, 110, and 120 $mV{\cdot}s^{-1}$ using the PB/ZnO/COOH-MWNTs/GCE electrode. The electrocatalytic reduction of H_2O_2 due to the effect of the potential by Nafion/PB/ZnO/COOH-MWNTs/GCE was observed by CV. The peak potential for the catalytically reduced H_2O_2 shifts to increasingly negative potential with enhancing scan rate larger. However, with the scan rates, the reduction and oxidation peak current (I_{pc}) for H_2O_2 increased linearly which explains that the reduction reaction was diffusion controlled. The relationship between the scan rate and I_{pc} was investigated to have a good linear connection over the range of 10 – 120 $mV{\cdot}s^{-1}$ as shown in Figure 2.13. The straight line indicates the diffusion controlled. A correlation coefficient (R^2) of 0.9943 and 0.9679 was observed for the linear regression equation, I_{pc} (μA) = 12.29 $V^{1/2}$ ($V{\cdot}s^{-1}$) + 39.62 and I_{pc} (μA) = 4.38 $V^{1/2}$ ($V{\cdot}s^{-1}$) + 20.27 for reduction and oxidation, respectively. Therefore, the reaction of H_2O_2 with the electrode surface area of Nafion/PB/ZnO/COOH-MWNTs/GCE displays good correlation with the expression of Randles-Sevçik as the I_{pc} goes up linearly as a function of the square root of the scan rate. The Randles-Sevçik equation describes the effect of scan rate on the peak current in the CV. Since the reaction takes place so rapidly that the rate of reaction is the transport of reactant through medium, it is referred to as a diffusion controlled reaction. The spontaneous transfer of electroactive species from regions of higher concentration to the regions of lower concentration occurs in this process. This phenomenon is characterized by the peak currents of reduction (I_{pc}) and oxidation (I_{pa}) to scale proportionally with the square root of the scan rate for irreversible redox processes according to the equation [106, 79]:

$$I_p = 0.4961\ nFAC_o^* \left(\frac{\alpha n F v D_E}{RT}\right)^{1/2} \quad (1)$$

where I_p is the peak current in amps, α is the transfer coefficient, n is the number of electrons, A is the electrode area (cm^2), D_E is the diffusion coefficient at the electrode surface ($cm^2 \cdot s^{-1}$), C_o^* is the concentration in $mol \cdot cm^{-3}$, and v is the scan rate in $V \cdot s^{-1}$, R is the universal gas constant, n is the number of electrons involved in the redox reaction, F is the Faraday constant, and T is the absolute temperature. Equation (1) can be used to estimate charged molecule diffusion coefficient for redox processes.

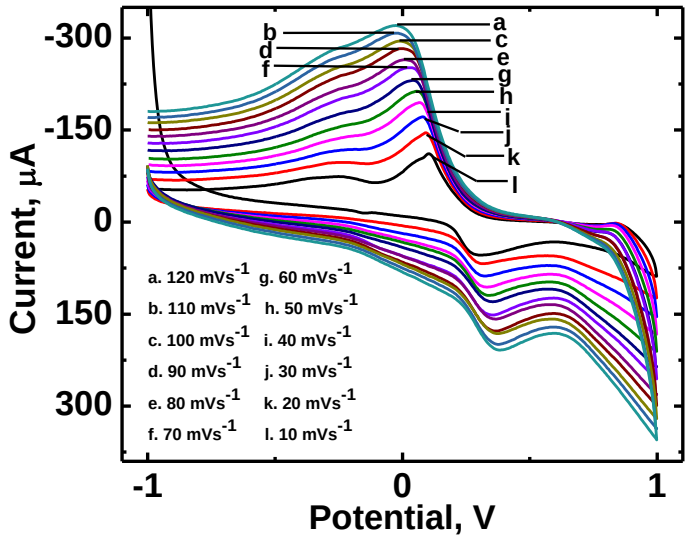

Figure 2.12: CV of 5 mM H_2O_2 in PBS with saturated N_2 at pH 7.0 on Nafion/PB/ZnO/COOH-MWNTs/GCE at various scan rates, (a) 120, (b) 110, (c) 100, (d) 90, (e) 80, (f) 70, (g) 60, (h) 50, (i) 40, (j) 30, (k) 20, (l) 10 $mV \cdot s^{-1}$

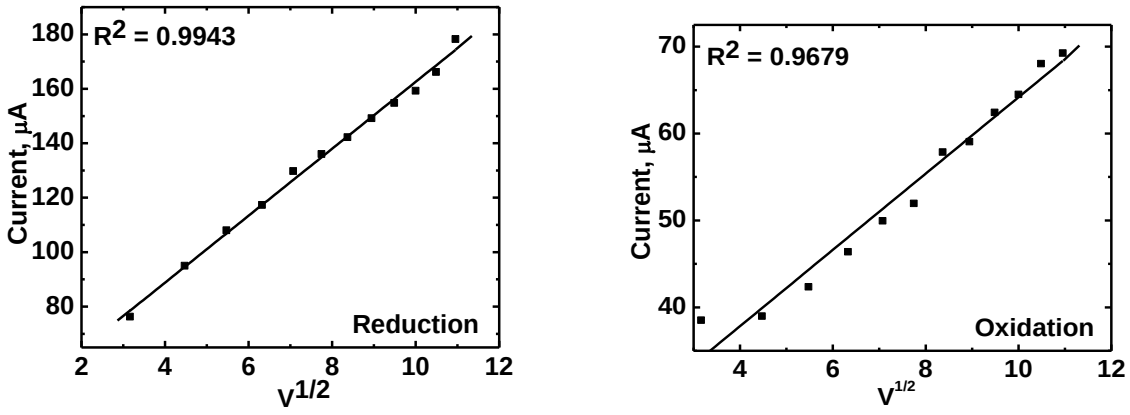

Figure 2.13: Randles-Sevçik plot of H_2O_2 at reduction and oxidation potential.

The facile method of reflux synthesized pure ZnO followed by tethered to COOH-MWNTs was performed using ultrasonication process. The fabricated ZnO/COOH-MWNTs was further attached with PB using PZC concept. The electrostatic force between PB and ZnO/COOH-MWNTs plays vital role to fabricate the sensor, PB/ZnO/COOH-MWNTs. PB in the composite increases the electron density with the purpose of significantly enhancing the sensitivity of H_2O_2 in physiological conditions. The diffusion rate at reduction potential was observed to be higher than that as oxidation potential. In summary, the reflux synthesis method and attachment of ZnO on the surface of COOH-MWNTs via ultrasonication followed by tethering of PB using an PZC process is an crucial pathway for the mass production of selective H_2O_2 sensors.

CHAPTER 3

Cytotoxicity study of PB/ZnO/COOH-MWNTs via Alamar Blue Assay

The biocompatibility of the PB/ZnO/MWNT nanocomposite for important applications in biomedical sensing field is analyzed. This nanocomposite was investigated for *in vitro* cytotoxicity of the PB/ZnO-MWNTs using the THP-1 macrophage cell line with the help of the Alamar Blue assay. Excellent biocompatibility of the PB/ZnO/MWNT with THP-1 macrophage cells were observed at a high concentration up to 200 µg/mL. The cytotoxicity effect of PB/ZnO/MWNT was compared with that of ZnO/MWNT nanocomposite.

3.1 Introduction

Widespread use of engineered nanoparticles have been realized recently because of their applications in various fields, including their importance for the fabrication of biosensors, drug and gene delivery, cancer treatment, and as diagnostic tools [107-113]. The effect of nanoparticle on human health and the environment is required to be assessed before they are applied in nanotechnology [107, 110, 113, 114]. To date, the current information of the effect of nanoparticles on human cells for the use of biosensor for *in vivo* analysis of target analytes is restricted [113]. With the advance of the field of nanotechnology, the cytotoxicity effect of ZnO NPs is specifically gaining increasing concern [115]. ZnO NPs is one of the most toxic nanoparticles in our applications. Huang et al. reported that ZnO shows the most toxic one out of fourth period transition metal oxide nanoparticles [116, 117]. Hsiao et al. attached ZnO with TiO_2 and studied the decrease of the cytotoxicity of ZnO nanoparticles [118]. A safer ZnO NPs synthesis method by doping with Fe ions was studied in 2009, resulting in the reduction of cytotoxicity with Fe doped ZnO NPs [119]. Being conjugated to nanoparticles within the CTL:PB NPs construct,

Prussian blue nanoparticle conjugation does not enhance any cytotoxicity effect to cytotoxic T lymphocyte [120]. Huang et al. reports that the HeLa cells was not affected by the presence of PB in the poly(vinylpyrrolidone) (PVP)-coated GaPBNPs composite under the cell viability assay [121]. Using THP-1 cells, we studied the cytotoxicity of PB/ZnO/COOH-MWNTs under our analysis via Alamar Blue assay. Alamar Blue assay has been used as a standard technique to assess cytotoxicity and cell viability of many cell types as reported previously. Viable cell changes into pink fluorescent product, resorufin from the non-fluorescent blue resazurin. Alamar Blue is used to analyze the reducing activity of the living cells. Resazurin is the active component of Alamar Blue [122]. Resazurin (Alamar Blue) and Resorufin present the following structures in scheme 3.1.

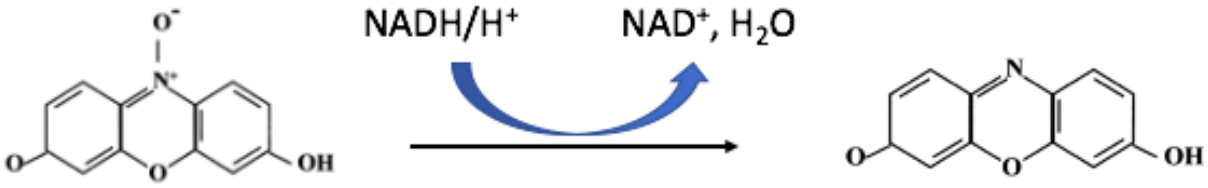

Resazurin Resorufin

Scheme 3.1: Structures of Resazurin and Resorufin

3.2 Materials and Methods

3.2.1 Preparation of PB/ZnO/COOH-MWNT nanocomposite for cytotoxicity study

A 4.0 mg of refluxed ZnO and 4.0 mg of COOH-MWNTs were mixed in absolute anhydrous ethyl alcohol (AAEA) and sonicated for 1 hr to disperse ZnO and COOH-MWNTs. The composite, ZnO/COOH-MWNTs was dried at 80^0 C. After complete dry of ZnO/COOH-MWNTs, this composite was dried in a dessicator for 24 hours. Then, 4.0 mg of ZnO/COOH-MWNTs were stirred with 2.0 mg of Prussian Blue (PB) in 1.0 mL PBS at pH 6.6 for 5 hrs to obtain 6 mg/mL

solution. A series of dilution was prepared to obtain 3.00, 1.00, 0.50, 0.25, and 0.125 mg/mL PB/ZnO/COOH-MWCNT nanocomposite concentrations.

3.2.2 Cytotoxicity Analysis

For the cell cytotoxicity study, the THP-1 human macrophage cells was obtained in Dr. Ying Gao's laboratory (Department of Biology, MTSU). Alamar blue^{TM} cell viability reagent was purchased from Thermo Fischer Scientific (Eugene, OR, USA). Insolution^{TM} Staurosporine, hemacytometer and RPMI 1640 was obtained from Sigma-Aldrich (St. Louis, MO, USA). The culture of THP-1 cells were performed in RPMI 1640 medium supplemented with 100 Unit/mL penicillin, 10%(v/v) fetal bovine serum (FBS), and 100 µg/mL streptomycin in a 5% CO_2 environment. When the cell confluency becomes 90%, the number of cells was calculated using a hemacytometer. THP-1 cells were seeded at 1.0 x 10^6, 0.9 x 10^6 and 1.0 x 10^6 cells per well in a 96-well plate. Cells were consequently treated with PB/ZnO/COOH-MWNTs in PBS at pH 7.4. The serial dilutions were conducted from the PB/ZnO/COOH-MWNT stock solution and added to 100 µL of THP-1 cell suspensions in a 96-well plate. It was finally cultured for 2 hrs. Staurosporine treated cells, untreated cells and blank solutions were simultaneously prepared as controls. After 2 hrs of incubation, 20 µL of 1x concentration of Alamar blue solution was mixed with cultures and incubated at 37^0C for 16 hrs in a 5% CO_2 condition. Fluorescence spectroscopy was used to study changes in fluorescence applying excitation/emission at 570/585 nm. Along with the optimization of cell count, 1.0 x 10^6 cells/well was chosen for triplicate experiments.

3.3 Results and Discussion

A human myelomonocytic cell line, THP-1 was obtained from a patient infected by acute monocytic leukomia [123]. THP-1 macrophage cells were incubated with various concentrations of PB/ZnO/COOH-MWNTs to study cytotoxicity of this composite. PB/ZnO/COOH-MWNT concentrations were spanned from 25 to 800 µg/mL and treated with 100 µL of THP-1 cells. After 2-hr incubation of THP-1 cells with various concentrations of PB/ZnO/COOH-MWNTs, it was further treated with Alamar blue and incubated for 16 hrs. Cytotoxicity of PB/ZnO/COOH-MWNTs was monitored on the basis of cell viability after 16 hrs incubation using Alamar blue assay as reported by Wang et. al in 2014 [124]. The counting of cells was carried out using hemacytometer. Alamar Blue dye is used as an intermediate electron acceptor in the electron transport chain. Alamar Blue dye converts into pink (reduced state) from blue (oxidized state) upon receiving electrons from metabolically active THP-1 cells, demonstrating the viability of THP-1 cells [125].

Figure 3.1 reports the color change of Alamar Blue dye from blue (oxidized state) to pink (reduced state). THP-1 cells were plated 1 x 10^6 cells/mL in rows A to H columns 1, 2 and 3. Row A column 1, 2 and 3 were untreated cells. Row B column 1, 2 and 3 were treated with staurosporine. Rows A and B column 4 are a blank solution only (media and PBS). Rows C to H columns 1 to 3 were treated with 0.025, 0.05, 0.1, 0.2, 0.4, 0.8 mg/mL of PB/ZnO/COOH-MWNTs, respectively. Rows C to H column 4 are treated with PB/ZnO/COOH-MWNTs only (cell-free). Untreated THP-1 cells in row A changed the Alamar Blue to pink, which explained the viablility of cells. However, Alamar Blue color was not changed with THP-1 cells treated with staurosporine, indicating that they are metabolically inactive. Rows C to H column 4 (PB/ZnO/COOH-MWNTs) did not show any color change of Alamar Blue explaining the

reduction processes was conducted in presence of live cells only in other wells. After the optimization of cell count, 1.0 x 10^6 cells/well was selected and triplicate experiments were performed. Figure 3.2 expresses the result of triplicate analysis, in which the evidence of the concentration-dependent toxicity pattern of PB/ZnO/COOH-MWNTs are shown. In this study, the survival rate was greater than 51% even at the highest amount of PB/ZnO/COOH-MWNTs of 200 µg/mL after 16 hours. There is no cytotoxicity issue beyond the 25 µg/mL, indicating the potential *in vivo* use of the composite.

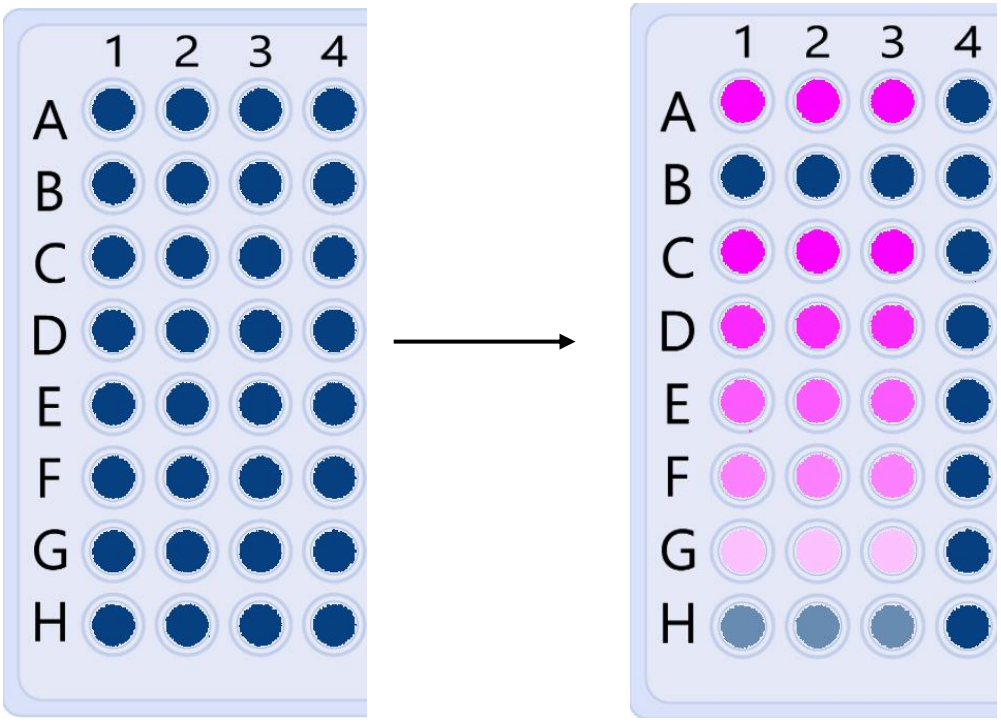

Figure 3.1: Alamar Blue assay using PB/ZnO/COOH-MWNTs against THP-1 cells; A (1-3): Untreated cells, B (1-3) Staurosporine (toxic) untreated cells, H-C (1-3): serial dilution of PB/ZnO/COOH-MWNTs (800-25 µg/mL), A-B (4): Blank, C-H (4): PB/ZnO/COOH-MWNTs

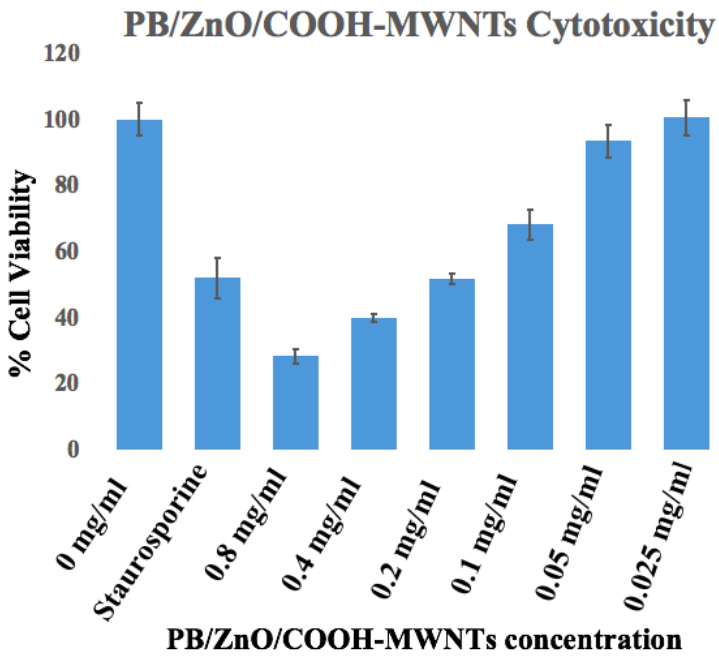

Figure 3.2: Cell viability of THP-1 cells after treating with PB/ZnO/COOH-MWNTs for 16 hrs at the concentrations shown, studied using Alamar Blue methods. Error bars indicate the means±standard deviation of three independent experiments.

3.4 Conclusions

The biocompatibility shown provides preliminary evidence that the composite can potentially be used for invasive assays. This is a new synthesized material proposed for biomedical sensing uses. This becomes very important as the application of this material is considered for *in vivo* study. Therefore, we have investigated the biocompatibility of the new fabricated PB/ZnO/COOH-MWNT nanocomposite for its potential uses in the field of biomedical sensing. The outcomes of our experiments have shown that the synthesized composite has very good compatibility with human THP-1 macrophage cells even at the amount of 200 µg/mL. Such results explain that the fabricated nanocomposite is an encouraging nanomaterial for use in the field of biomedical sensing. Since the extent of cytotoxicity of ZnO nanoparticles in the composite was analyzed, there are no artifacts from the electrode killing cells being measured. So, it will be important for this sensor to be further analyzed for H_2O_2 in other cell lines.

CHAPTER 4

Sensitive and selective Quantification of H_2O_2 in BT20 and 4T1 breast cancer cells

Abstract

A Prussian Blue (PB) zinc oxide carbon nanotube sensing composite was developed for the rapid assaying of H_2O_2 generated from BT20 and 4T1 breast cancer cells, important for elucidating mechanisms governing apoptosis of these cell lines. The combination of H_2O_2's transient nature along with matrix effects makes monitoring this molecule in biological samples a challenge. The standard addition method (SAM) was coupled with chronoamperometric sensing (CA) to overcome these obstacles. An electrocatalyst composite consisting of refluxed zinc oxide nanoparticles (NPs) tethered to carboxylic acid-functionalized multiwalled carbon nanotubes (ZnO/COOH-MWNTs) was electrostatically attached to PB for signal enhancement. Optimization of the sensor was achieved via adjusting solution pH and stirring time to optimize PB electrostatic attachment to ZnO/COOH-MWNTs prior to its deposition onto the working glassy carbon electrode (GCE) surface. CA SAM showed the ability to accurately measure H_2O_2 within the 1−21 μM range, suitable for monitoring cancer cell line apoptosis resistance scenarios and offering analytical advantages over standard enzyme-linked immunosorbent assays (ELISA) for rapid, matrix-effect-free analysis.

4.1 Introduction

Selective and quantitative measurements of H_2O_2, an important reactive oxygen species (ROS), are involved in a host of biological redox reactions [126]. Breast cancer is the most common type of malignant neoplasm among women worldwide [127]. It is estimated that 266,120 new cases of breast cancer were diagnosed in 2018, representing 15.3% of all new cancer cases in the U.S. that year [128]. A growing body of evidence suggests that oxidative stress, generating

ROS (of which H_2O_2 is the most stable as compared to peroxides, superoxides, hydroxyl radicals, and singlet oxygen), plays a key role in regulating pathways in tumor cell survival [129]. The ability to accurately measure H_2O_2 is important for understanding mechanisms underlying this phenomenon and thereby improve practical chemotherapy. However, matrix effects from interfering species in biological samples coupled with the transient nature of ROS hamper accurate measurements. Furthermore, standard immunoassays, which typically incorporate the use of fluorescent dyes contribute to the complexity of the analyte solution. Despite recent improvements in fluorescent [39, 130, 131] and genetically encoded [132] probes, very few ROS quantification studies are conducted in cancer cell media due to the lack of suitably accurate measurement techniques [133, 134]. To this end, we have developed an innovative tool for rapidly and accurately quantifying H_2O_2 in breast cancer cell media to enable these mechanistic studies.

Applying the standard addition method (SAM) to chronoamperometry (CA) detection can be used to overcome these difficulties presented by sample matrix effects. SAM is typically applied to atomic absorption, fluorescence spectroscopy, ICP-OES, and gas chromatography. There are few literature reports in which SAM is applied to CA. To date, only one group has successfully coupled SAM with CA for measuring H_2O_2; Zbiljiać et al. used a Prussian Blue (PB) carbon nanotube composite to do so [135]. The analysis range achieved in this study, however, has a lower limit of 10 μM, which is still insufficiently sensitive for analyzing oxidative stress in cancer cell lines. Furthermore, the electrochemical technique relies heavily on the Fenton reaction for H_2O_2 quantitation. In applications involving ROS probes in cancer cell media, this feature would hamper ROS analysis due to generation of additional ROS by the PB-based electro-composite. We have improved upon this electrocatalyst design by incorporating ZnO upon which H_2O_2 redox will largely take place.

Typically, slow electrocatalyst kinetics and requirements of high overpotential typically delay efficient electrochemical determination of H_2O_2 on a glassy carbon electrode (GCE) [53]. PB was electrostatically attached to the ZnO/COOH-MWNT composite, taking advantage of differences in the point of zero charge (PZC) between these two materials to attach PB to the ZnO/COOH-MWNT surface. Previously in our lab, Wayu et al. [32, 136] attached zinc oxide (ZnO) nanoparticles (NPs) to the carboxylic acid-functionalized multiwalled carbon nanotube (COOH-MWNT) surface via ultrasonication to detect hydrogen peroxide (H_2O_2). The modified electrode showed remarkable electrocatalytic activity and a stable response toward its detection. Hemoglobin (Hb), a redox enzyme, is known to increase the sensitivity and linear range of detection of H_2O_2 when it is attached to the ZnO/COOH-MWNTs as compared to the sensor without the tethered enzyme [86, 137]. We have applied PB to enhance redox activity for H_2O_2 detection using the ZnO/COOH-MWNT composite. PB, touted as an "artificial enzyme peroxidase" [57, 58], was used to enhance the redox properties of the ZnO/COOH-MWNTs to monitor H_2O_2. PB, $Fe^{III}[Fe^{II}(CN)]$, has multiple oxidation states [59] and a face-centered cubic lattice structure of a hexacyanoferrate having ferric and ferrous ions alternating in the cubic lattice sites, associated with the N and C atoms of the cyanide groups, respectively. PB is still employed as a source of electron transfer to enhance sensitivity, but the Fe mole fraction is kept low to greatly reduce Fenton-like reactions while facilitating the vast majority of redox reactions taking place at the ZnO surface. Redox activity accompanying the attachment of the PB to the ZnO/COOH-MWNTs led to enhanced H_2O_2 signal detection. Contributions from the Fenton reaction were greatly minimized on the electrode surface by keeping its surface mole fraction small. We achieved a 0.04% elemental mole fraction of Fe in the composite fabrication on the GCE surface (*vide supra*) thereby ensuring most of the H_2O_2 redox taking place at the ZnO interface. BT20 cells are

used as a model system for studying estrogen-unresponsive breast cancer. BT20 is the oldest and most widely studied of the triple negative breast cancer cell lines that was first identified from a 74-year old woman with breast carcinoma in 1958 [138, 139]. The 4T1 mammary carcinoma cell line, obtained from mice, can also be used to model human breast cancer activity. Unlike most tumor models, 4T1 can spontaneously metastasize from primary tumors in the mammary gland to multiple distant sites, such as lymph nodes, liver, lung, and bone, and hence is an excellent model system for stage IV human breast carcinoma [140].

In this study, we demonstrate, for the first time, the utility of a PB/ZnO/COOH-MWNT composite for chronoamperometric measurements of H_2O_2 in BT20 and 4T1 breast cancer cells at concentration ranges produced when these cells were oxidatively stressed. The results of this new H_2O_2 assaying technique is compared with those obtained from enzyme linked immunosorbent assays (ELISA).

4.2 Materials and Methods

Bamboo structure COOH-MWNTs (95% purity, 30 nm diam.) were purchased from Nanolab, Inc. (Waltham, MA, USA), and used as received. Reagent grade (99% purity) uric acid, phosphate buffer solutions (PBS, pH = 7.0), Prussian Blue (PB), acetaminophen (APAP), zinc nitrate hexahydrate (98% purity), folic acid (FA), and L-ascorbic acid (AA) (99% purity) were all purchased from Sigma-Aldrich (St. Louis, MO, USA). NaOH and hydrogen peroxide (H_2O_2) (30%) were obtained from Fischer Scientific (Fair Lawn, New Jersey, USA). Absolute anhydrous ethyl alcohol (AAEA) was purchased from Pharmco-AAPER (Shelbyville, KY, USA). Nafion^{TM} binder was obtained from Ion Power, Inc, (New Castle, DE, USA). Phosphate buffered saline solution (PBS) was used as the medium to manage the pH of the electrochemical cell. All chemical

reagents were of 99.9% purity or greater and obtained from Sigma-Aldrich (St. Louis, MO, USA). All experiments were conducted in deoxygenated electrolyte solution prepared by bubbling 99.9% purity N_2 gas flow (Air Gas Products, Radnor, PA, USA) through the solution for 12 min prior to each measurement. The preparation of all solutions was done using Millipore water (18 MΩ·cm).

4.2.1 Cell Culture

BT20 and 4T1 cells were purchased from American Type Culture Collection (ATCC, Manassas, VA, USA). Both cell lines were maintained in RPMI-1640 medium (Sigma-Aldrich, St. Louis, MO, USA) with 10% Fetal Bovine Serum (FBS) (Gibco) at 37°C with 5% CO_2. The medium was renewed every two days. Well-grown BT20 cells in the logarithmic phase were digested by 0.25% (w/v) Trypsin (Fisher Scientific, Hampton, NH, USA) from the original culture flask and mixed well before being seeded on a 96-well cell culture plate (Denville Scientific, Metuchen, NJ, USA) in the density of 5×10^4 cells/mL and incubated with the same full medium at 37°C with 5% CO_2 for 24 h. Cells were then treated with 100 μL of 50 μM doxorubicin (Dox) (Sigma-Aldrich, St. Louis, MO, USA). Cells treated with 100 μL of vehicle only served as a control. The Dox group and control group each had eight replicate wells. After 24 h of incubation, 50 μL of the medium was collected from each well and proceeded for H_2O_2 determination.

4.2.2 Hydrogen Peroxide Release Assay

The H_2O_2 release assay was carried on using Amplex™ Red Hydrogen Peroxide/Peroxidase Assay Kit (Invitrogen, Carlsbad, CA, USA) according to instruction. The H_2O_2 standards for standard curve were prepared by diluting the 20 mM H_2O_2 stock solution with 1x reaction buffer. The final concentrations of seven H_2O_2 standards were 10.0, 5.00, 2.50, 1.25, 0.625, 0.312, and 0.0 μM, respectively. After 50 μL of the sample medium and 50 μL of each

standard were loaded into 96-well plate, 50 μL of the working solution (0.1 mM Amplex^{TM} Red reagent, 0.02 U/mL horseradish peroxidase, and 1x reaction buffer) were added into these wells. After incubation at room temperature (25^0C) in the dark for 30 min, the absorbance of each well at 560 nm of was measured with a CLARIOstar^{TM} microplate reader (BMG Labtech, Cary, NC, USA). The concentration of H_2O_2 in the sample was calculated according to the standard curve. The student's t test was applied for the analysis of the statistical difference between the Dox group and control group.

4.2.3 Preparation of the Nafion/PB/ZnO/COOH-MWNTs/GCE sensor

Prior to modification, the GCE was polished using a 1.0-μm diameter Al_2O_3 slurry (Buehler Ltd, Lake Bluff, IL, USA), and then further polished using a 0.05-μm diameter Al_2O_3 slurry to obtain a mirror like finish. Doubly-distilled deionized 18 MΩ Millipore water (Milli-Q water filtration system, Model ELix, USA) was used to rinse the electrodes. GCEs were then cleaned by sonication in a 1:1 volume mixture of concentrated HNO_3:H_2O for 5 min. The electrodes were then dried at room temperature. Each PB/ZnO/COOH-MWNTs nanocomposite was drop-casted onto glassy carbon electrodes (GCE), 3 mm in diam. A 5-μL colloidal aliquot of the composite as a colloidal suspension was pipetted on the cleaned GCE surface. The GCE was then kept into the oven for 20 min at 80^oC. After drying, a second 10-μL aliquot of 2% Nafion^{TM} solution was dropped on top to cap the composite and dried in an oven at 80^o C for additional 12 min to obtain Nafion^{TM}/PB/ZnO/COOH-MWNTs/GCE sensor for further study.

4.3 Results and Discussion

In the CV of the 5 mM H_2O_2 solution in PBS (Figure 4.1), the 60 min sonicated composite showed the optimum sensitivity with hydrogen peroxide (H_2O_2) due to the proper optimum loading of the ZnO particles on the surface of MWNTs as shown in Figure 4.1.

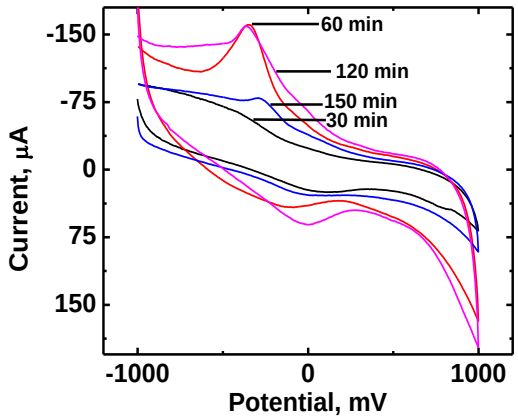

Figure 4.1: CVs in 5 mM H_2O_2 at 50 $mV \cdot s^{-1}$ using ZnO/COOH-MWNTs
Reproduced with permission from ref. [29]. Copyright 2019, American Chemical Society

4.3.1 Electrocatalytic characteristics and optimization of the sensor

Figure 4.2A displays the different electrocatalytic activities due to various loadings of PB with ZnO/COOH-MWNTs nanocomposites. Highest electrocatalytic activity was observed at (2:1) mass ratio of PB to ZnO/COOH-MWNTs composite. Figure 4.2B shows a series of CVs at room temperature for different stirring of preliminary PB/ZnO/COOH-MWNTs composite fabricated using 60 min sonication time as shown. This figure exhibits the current measured across the working electrode as a function of voltage versus Ag/AgCl reference electrode. CV system was performed with phosphate buffer solution at pH 7.0. The optimum sensitivity of this composite was observed at 2:1 ratio of ZnO/COOH-MWNTs to PB (Figure 4.2A) and 5 hrs stirring (Figure 4.2B and 4.2C).

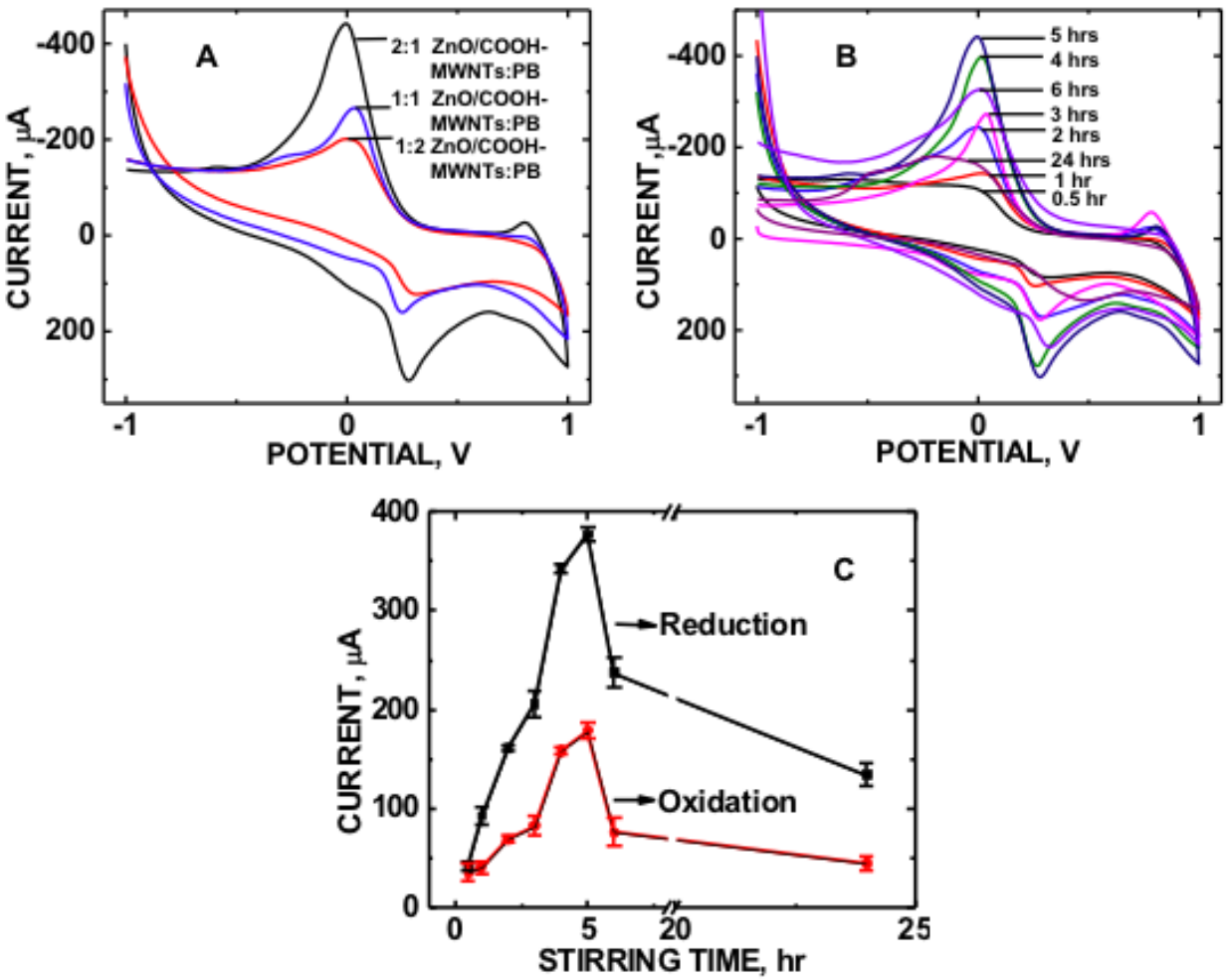

Figure 4.2: CVs of 5 mM H_2O_2 at pH 7.0 showing (A) effect of PB to ZnO/COOH-MWNTs ratios (by mass); and (B) stirring time for PB to attach to ZnO-COOH-MWNTs; (C) a graph showing 5 hrs stirring time for optimum sensitivity. Reproduced with permission from ref. [29]. Copyright 2019, American Chemical Society

The electrochemical response of Nafion™/PB/ZnO/COOH-MWNT/GCE surface with H_2O_2 was studied as control experiments. As shown in Figure 4.3, point e, there was no electrochemical behavior to H_2O_2 on the bare GCE at given potential in PBS (pH 7.0) solution. The cathodic and anodic current peaks were observed at -0.004 V and +0.27 V, respectively, which had a pronounced electrochemical response when GCE was modified with PB/ZnO/COOH-MWNTs (Figure 4.3, point a). Electrochemically controlled experiments were performed using ZnO/COOH-MWNTs and PB in which our composite (PB/ZnO/COOH-MWNTs) shows the 3

times higher sensitivity result compared without PB as shown in Figure 4.3. The increase is attributed to the proper attachment of PB, on the surface of ZnO/COOH-MWNTs. The improvement of electrochemical signal due to the attachment of PB with ZnO/COOH-MWNTs are shown as

$$Fe_4^{III}[Fe^{II}(CN)_6]_3 + 4e^- + 4K^+ \xrightarrow{\text{ZnO-COOH-MWNTs}} K_4\,Fe_4^{II}[Fe^{II}(CN)_6]_3 \quad (1)$$

$$K_4\,Fe_4^{II}[Fe^{II}(CN)_6]_3 + 2\,H_2O_2 \longrightarrow Fe_4^{III}[Fe^{II}(CN)_6]_3 + 4\,OH^- + 4\,K^+ \quad (2)$$

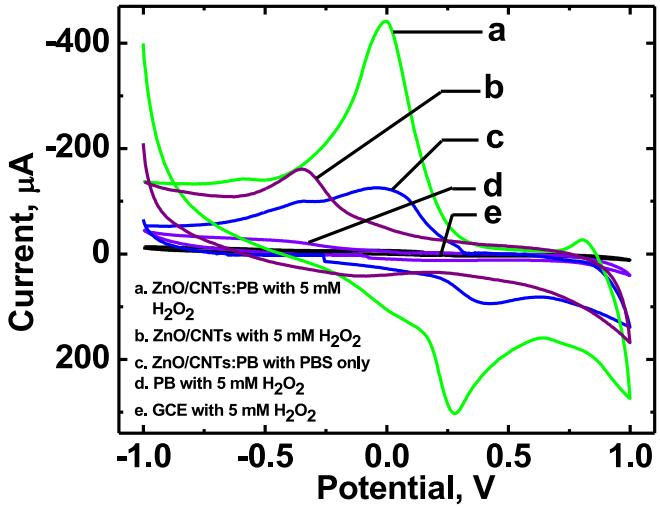

Figure 4.3: Analysis of H_2O_2 under CV at pH 7.0 with 50 $mV{\cdot}s^{-1}$ scan rate using (a) PB/ZnO/COOH-MWNTs with 5 mM H_2O_2, (b) ZnO/COOH-MWNTs with 5 mM H_2O_2, (c) PB/ZnO/COOH-MWNTs with PBS only, (d) PB with 5 mM H_2O_2, (e) GCE with 5 mM H_2O_2

Reproduced with permission from ref. [29]. Copyright 2019, American Chemical Society

Symmetric peak shapes in the CVs at various pH conditions denoted quasi-reversible redox processes. During CV, H_2O_2 is oxidized to hydroxide and hydroxide is reduced back to H_2O_2 via a two-electron process [141]. Figure 4.4 shows the amperometric response of the Nafion^{TM}/PB/ZnO/COOH-MWNTs/GCE as a function of pH in 5 mM H_2O_2 at reduction and oxidation potentials of -0.004 V and +0.27 V, respectively; the corresponding CVs of 5 mM H_2O_2 are shown in the Figure 4.5. The cathodic and anodic currents are maximized at pH 7.0 for both oxidation and reduction potentials. Figure 4.5 shows that our sensor is capable of detecting

H_2O_2 at various pH conditions. The optimum detection response of H_2O_2 was observed from pH 7.0–7.4. The highest electrocatalytic activity of our sensor with H_2O_2 was observed at pH 7.0 at both oxidation and reduction potentials.

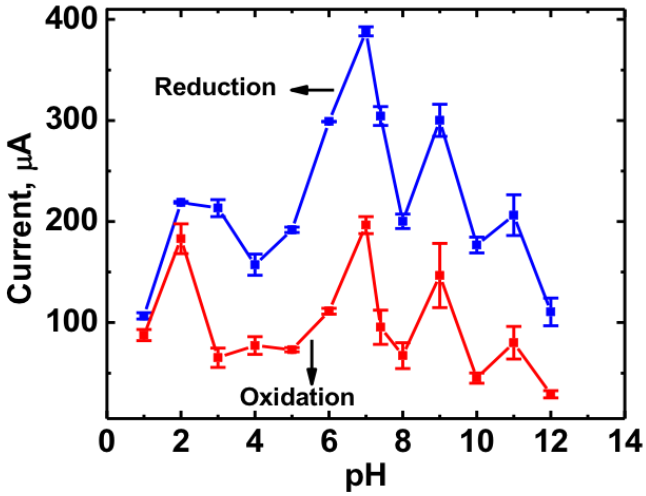

Figure 4.4: A plot of pH vs current to show optimum pH response for highest electrocatalytic activity at pH 7.0 using CVs at reduction and oxidation potential of -0.004 V and +0.270 V, respectively

Reproduced with permission from ref. [29]. Copyright 2019, American Chemical Society

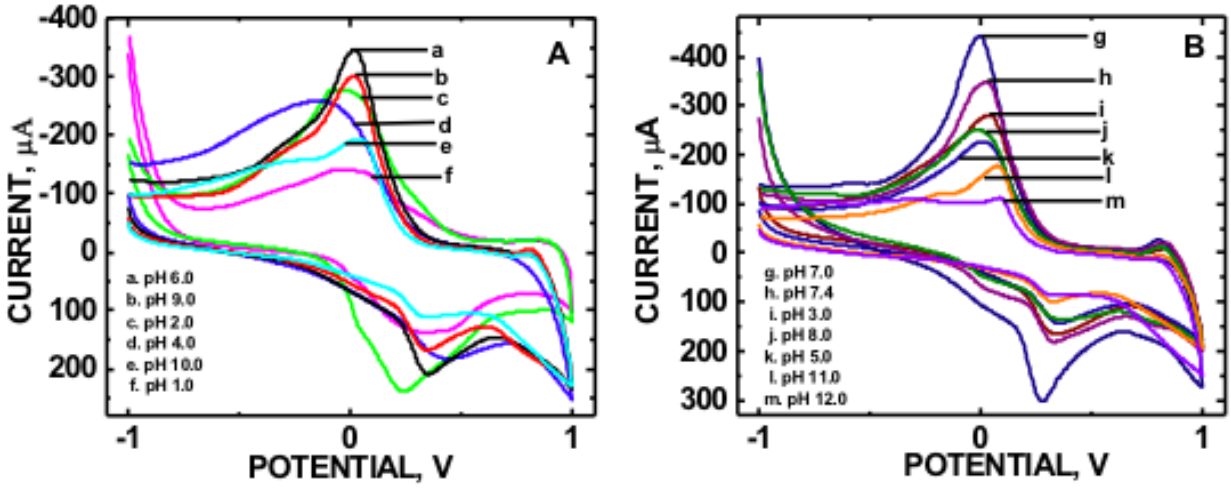

Figure 4.5: Effect of pH in the measurement of 5 mM H_2O_2 at 50 $mV \cdot s^{-1}$ using PB/ZnO/COOH MWNTs

Reproduced with permission from ref. [29]. Copyright 2019, American Chemical Society

Figure 4.6A shows a typical current-time curve of CA at the Nafion^{TM}/PB/ZnO/COOH-MWNTs modified electrodes for successive addition of various concentrations of H_2O_2 in PBS of pH 7.0 at -0.004 V. The sensor achieves a steady state current within 4 sec. It was determined that H_2O_2 concentration can be detected as low as 1 μM. The detection limit based on CA was 0.019±0.01 μM. Figure 4.6B shows a linear relationship with correlation coefficient, R^2 = 0.9678 for H_2O_2 concentrations from 1 μM to 3 mM. These results can be used to study oxidative stress of H_2O_2 in cells potentially. The oxidative stress of hydrogen peroxide on certain cancer cell lines such as MCF-10F, MCF-7 and MDA-MB-231 cell lines were studied using Dox [142]. Dox treated cancer cell lines shows the higher concentration of H_2O_2 compared to that of untreated cancer cell lines within the range of 6-to-14 μM. The detection of H_2O_2 from 2.0-to-20.0 μM is sufficient to analyze oxidative stress in these cell lines. Figure 4.6C shows an improved correlation coefficient of R^2 = 0.9822 within the concentration range of 2.0-to-22.0 μM of H_2O_2.

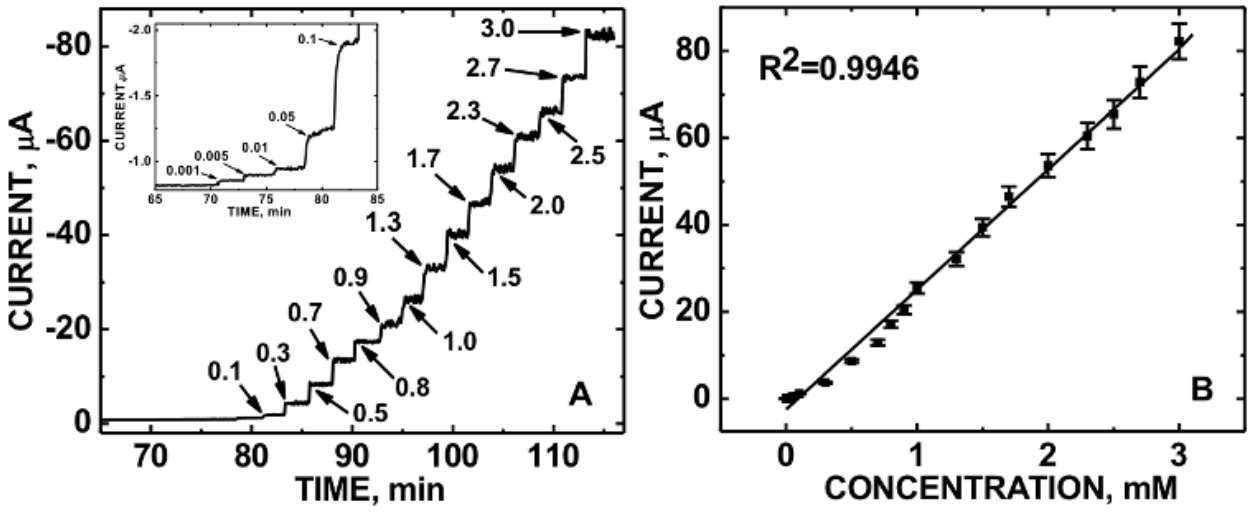

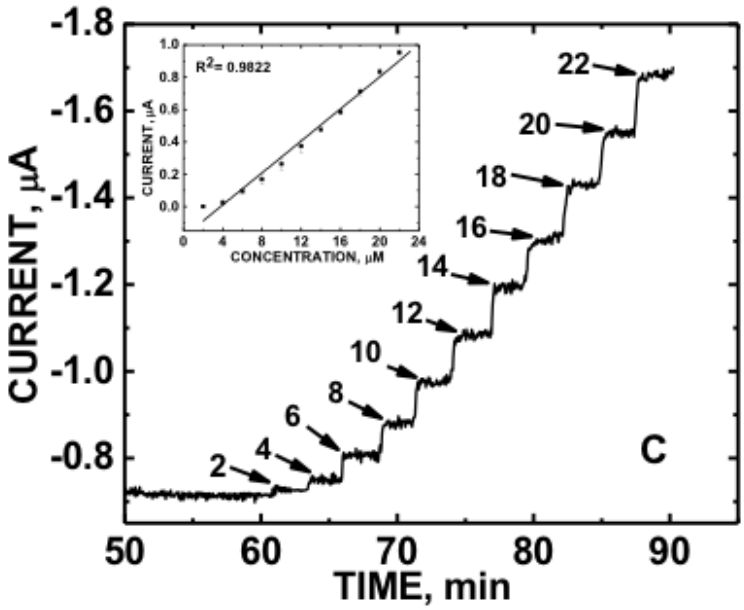

Figure 4.6: Analysis of H_2O_2 under CA at pH 7.0 with 50 $mV \cdot s^{-1}$ scan rate using PB/ZnO/COOH-MWNTs (A) a spectrum showing the detection of H_2O_2 from 1μM to 3 mM; (B) a calibration curve with $R^2 = 0.9678$; and (C) Analysis of H_2O_2 under CA at pH 7.0 with a 50 $mV \cdot s^{-1}$ scan rate using PB/ZnO/COOH-MWNTs

Reproduced with permission from ref. [29]. Copyright 2019, American Chemical Society

Similarly, CV can also study this range of H_2O_2 with $R^2 = 0.9786$ to study oxidative stress of H_2O_2 as shown in Figure 4.7.

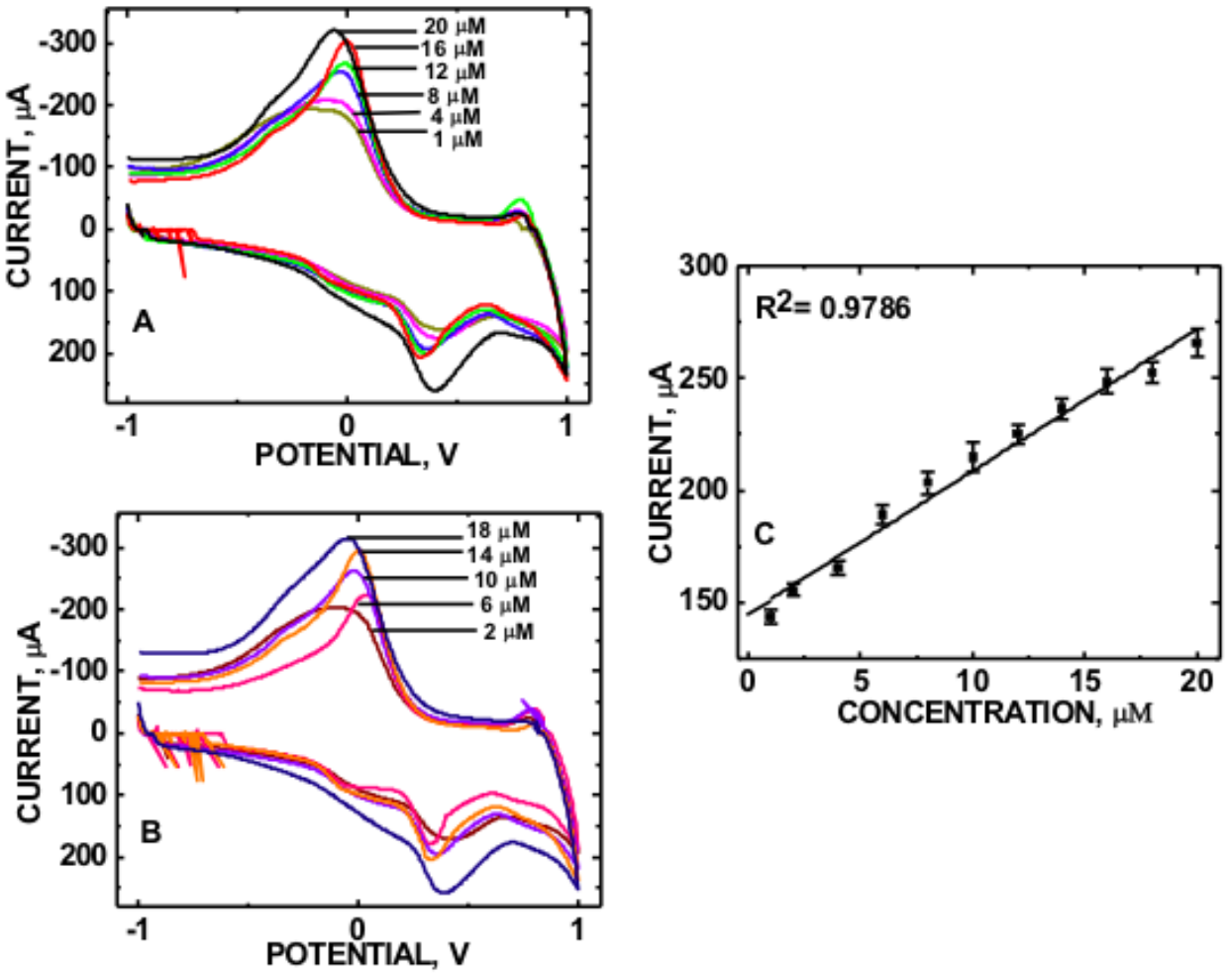

Figure 4.7: (A and B) CVs of H_2O_2 at various concentrations under pH 7.0 conditions, using PB/ZnO/COOH-MWNTs at scan rate of 50 $mV \cdot s^{-1}$; (C) calibration curve of current vs concentration under CV at pH 7.0

Reproduced with permission from ref. [29]. Copyright 2019, American Chemical Society

Figure 4.7A and 4.7B shows how CV current varied as a function of H_2O_2 from 1-to-20 μM. Figure 4.7C shows a linear correlation between the peak current and the concentration at reduction potential of -0.004 V, with correlation coefficient of $R^2 = 0.9786$.

Analytical application of the Nafion™/PB/ZnO/COOH-MWNTs/GCE sensor was studied using standard addition method under chronoamperometry (SAM CA) technique. SAM was applied by spiking in known H_2O_2 concentration, and plotting the resulting current as a linear

function of known concentration. Finally, the concentration of the analyte can be quantified when the line is extrapolated across the concentration axis (X) at zero signal intensity (i.e., at y = 0, and then, x = -b/m so that the concentration becomes b/m) [143, 144].

A sample calculation procedure for a standard addition method under CA to calculate H_2O_2 in the breast cancer cell lines is shown below (Table 4.1).

	A	B	C	D	E	F	G
1	Hydrogen peroxide standard addition method						
2	Add 0.2 mM H_2O_2 to 1.5 mL H_2O_2 containing samples, such as breast cancer cell lines						
3							
4							
5	Vo (mL)=		Vs=		I(s+x)=	X-axis function	Y-axis function
6		1.5	µL H_2O_2 added	mL H_2O_2	Signal (µA)	Si*Vs/Vo	I(s+x)*V/Vo
7	[Si]i (mM)=		0	0	513.7332	0	513.7332
8		0.2	82.5	0.0825	666.1359	0.011	702.7733745
9			94.95	0.09495	764.5152	0.01266	812.9090122
10			109.0343	0.109034	839.0105	0.014537907	899.9977817
11			125.0539	0.125054	916.9178	0.016673853	993.3605646
12			143.3654	0.143365	1009.8948	0.019115387	1106.417448
13			164.3923	0.164392	1106.2837	0.021918973	1227.526715
14			188.6401	0.18864	1206.6534	0.025152013	1358.402212
15			216.7142	0.216714	1303.3267	0.028895227	1491.626302

Table 4.1 Standard addition method under CA to detect H_2O_2
Reproduced with permission from ref. [29]. Copyright 2019, American Chemical Society

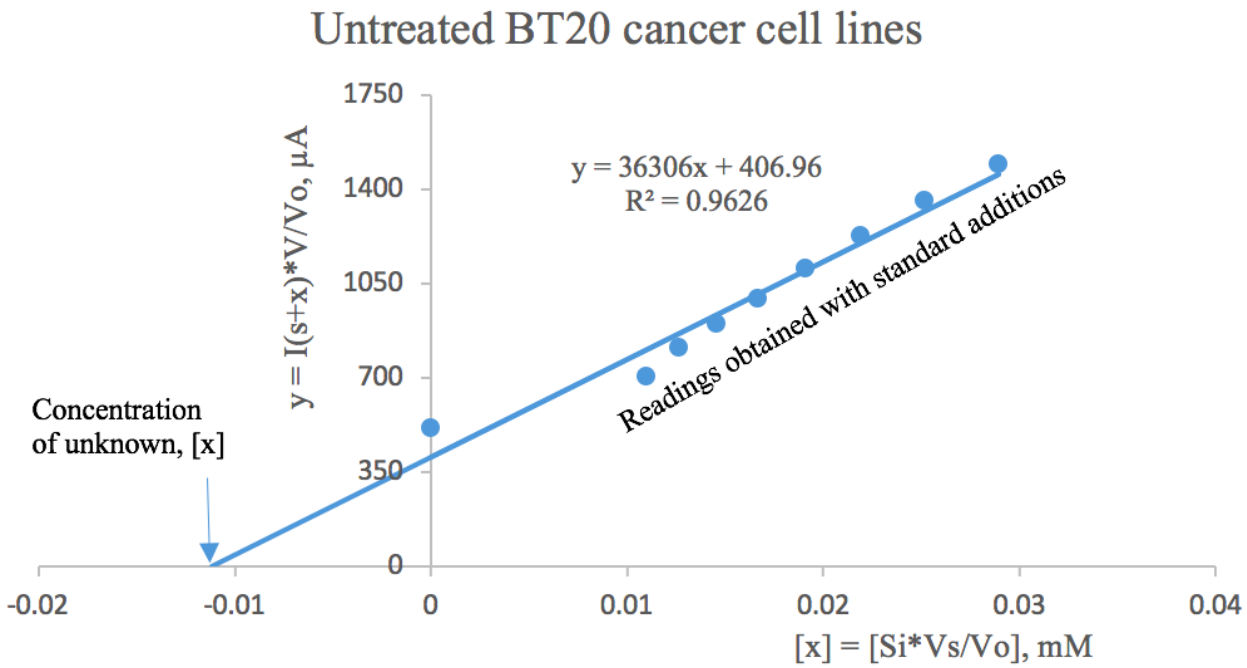

Figure 4.8: A graphical representation under standard addition method to detect H_2O_2 in complex cell systems
Reproduced with permission from ref. [29]. Copyright 2019, American Chemical Society

The standard addition method (SAM) is typically used for atomic absorption, fluorescence spectroscopy, ICP-OES and gas chromatography, but that we are applying it for the first time using CA. The SAM is especially suitable provided the sample composition is unknown or complex and shows an effect on the analytical signal. A linear relationship between the concentration and the analytical current signal of H_2O_2 is a prerequisite for using the SAM. Using the sensor, Nafion^{TM}/PB/ZnO/MWNTs/GCE, the SAM was used to determine H_2O_2 concentrations ranging from 1-to-21 µM in PBS (Figure 4.8, as a representative analysis using 5 µM H_2O_2 stock solution) before proceeding to the BT20 and 4T1 cancer cell lines. The relationship between known and calculated concentration of H_2O_2 was found with the correlation coefficient value, $R^2 = 0.9932$ as shown in Figure 4.10.

Figure 4.9 displays the raw results of standard addition method under CA. The results show that the standard addition method calculated the known concentration of H_2O_2 from 1-to-21 μM using CA. The number arrow pointed in the chromatogram represents the spiking volume of H_2O_2 such as a, b, c, d, e, f, g, h indicates 82.5, 94.9, 109.0, 125.0, 143.4, 164.4, 188.6, and 216.7 μL H_2O_2, respectively, spiked in that specific point. The raw data of standard addition method at 5 μM H_2O_2 stock solution is further analyzed using calibration curve of current vs concentration. The equation generated from the calibration curve is used to calculate the concentration of 5 μM H_2O_2 stock solution as shown here. In equation in Figure 4.9B, y = 57518 x + 309.13, x value is equal to 0.0053 mM or 5.3 μM H_2O_2 when y = 0. Finally, relationship between known and calculated H_2O_2 is established to support the validation of this SAM CA technique as shown in Figure 4.9. The calculated H_2O_2 concentration was based on CA current.

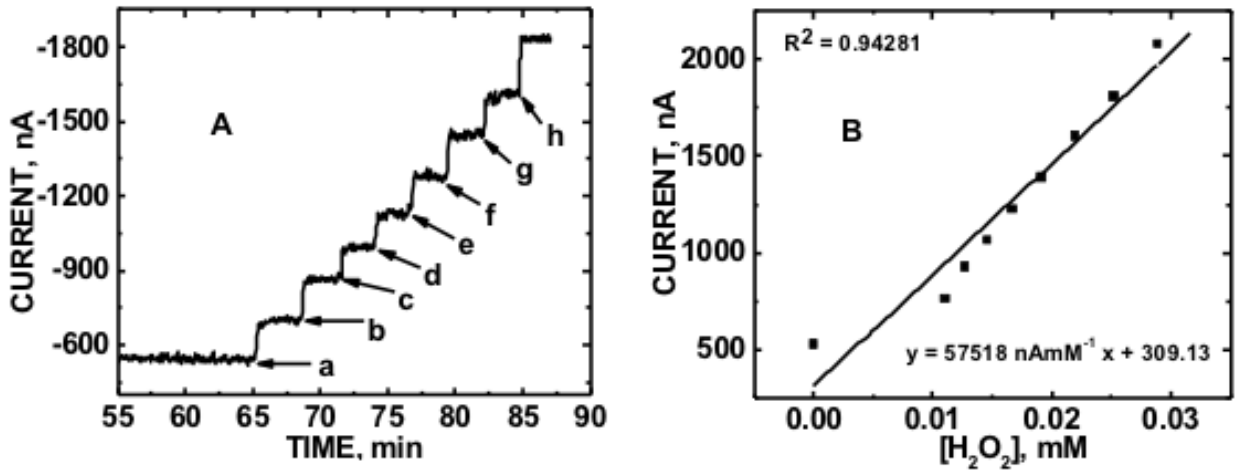

Figure 4.9: Employing the SAM to CA for assaying H_2O_2 using PB/ZnO/COOH-MWNTs using a (A) 5 μM stock solution, and (B) calibration curve to analyze the concentration of H_2O_2 at 5 μM stock solution (representative sample at 5 μM H_2O_2 stock solution)
Reproduced with permission from ref. [29]. Copyright 2019, American Chemical Society

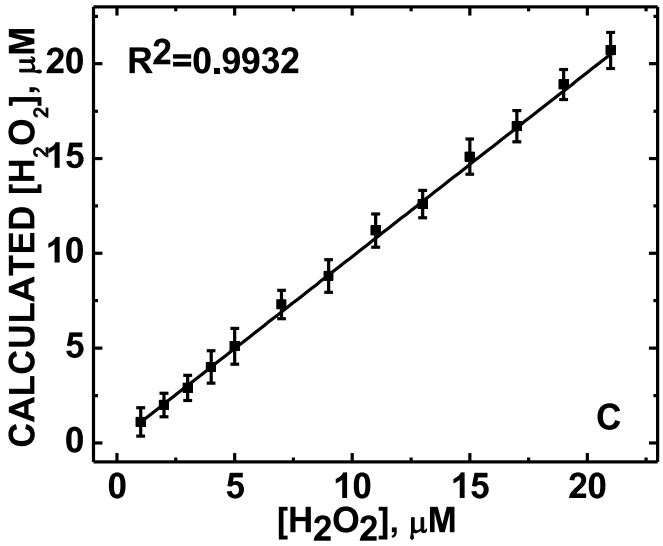

Figure 4.10: Relationship of known and calculated concentration of H_2O_2 using SAM CA in PBS (pH = 7.0) at 50 $mV \cdot s^{-1}$ using PB/ZnO-COOH-MWNTs
Reproduced with permission from ref. [29]. Copyright 2019, American Chemical Society

SAM was finally applied in BT20 and 4T1 cancer cell lines to study oxidative stress of H_2O_2 on those cell lines using Dox. This SAM was carried out in untreated and 48 hrs Dox treated BT20 cancer cell lines to compare the generation of H_2O_2 as shown in Figure 4.11. The raw data obtained from SAM of CA and its calibration curve for analysis are shown. The concentration of H_2O_2 in untreated and 48-hr Dox-treated BT20 cancer cell lines were calculated to be 10.1±1.3 μM and 16.0 ± 1.2 μM, respectively. The raw data under standard addition method of CA analyzing untreated and Dox-treated BT20 cancer cell lines are shown in Figure 4.11A and 4.11C with its calibration curve as shown in Figure 4.11B and 4.11D, respectively.

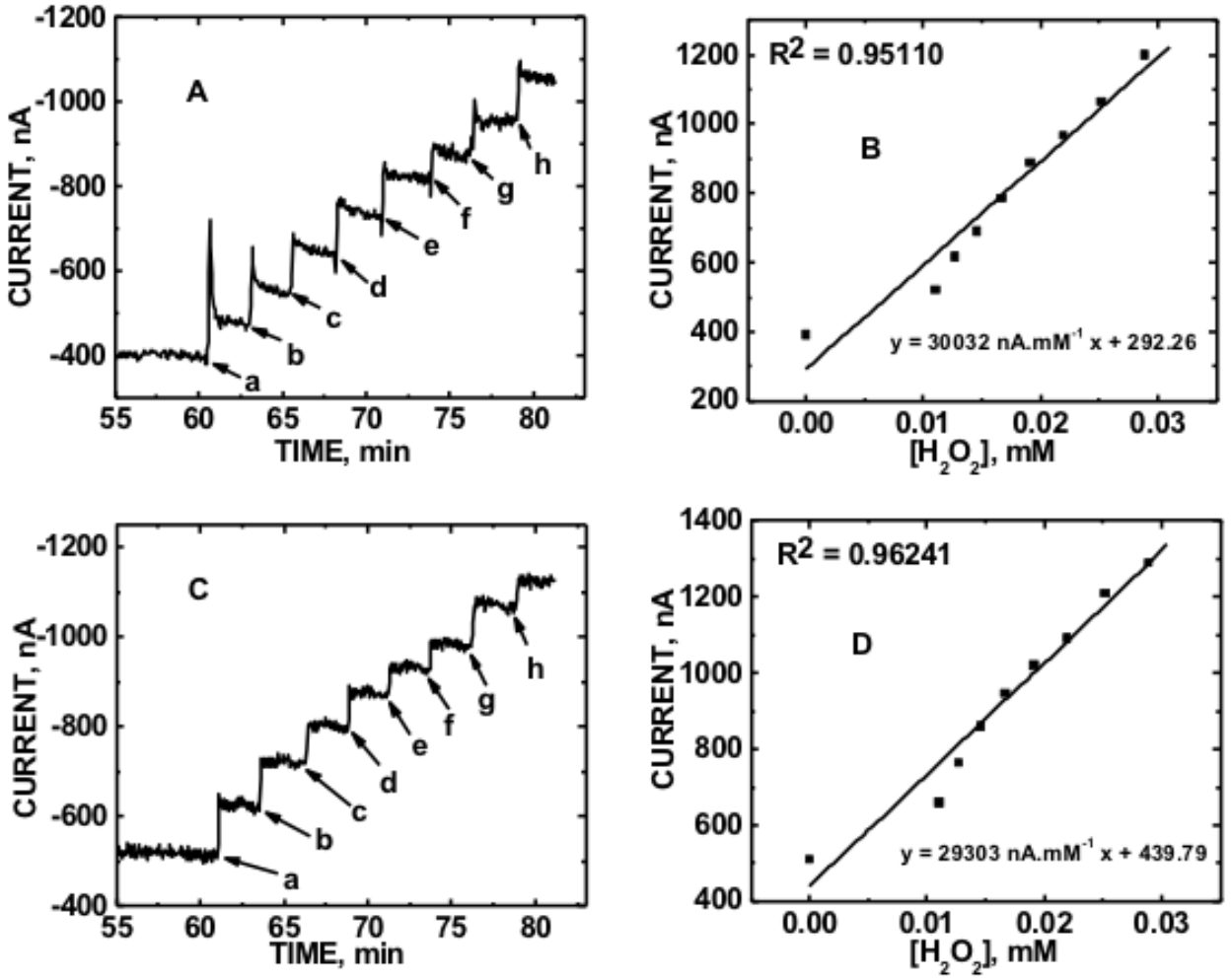

Figure 4.11: Standard addition method to detect H_2O_2 in BT20 cancer cell lines under CA in aqueous media using PB/ZnO/COOH-MWNTs (A) raw data of untreated BT20 cancer cell lines, (B) calibration curve of untreated BT20 cancer cell lines, (C) raw data of Dox-treated BT20 cancer cell lines and (D) calibration curve of Dox-treated BT20 cancer cell lines

Reproduced with permission from ref. [29]. Copyright 2019, American Chemical Society

The results (Table 4.2) appeared as higher concentration of H_2O_2 in Dox treated samples (16.0±1.4 μM) (n = 6) compared to untreated same cancer cells (10.1 μM) (n = 6) with the standard deviation of 1.2 μM in BT20 cancer cell lines as shown in Figure 4.11A.

Table 4.2: Comparison of H_2O_2 (μM) from Dox treated and Untreated BT20 cancer cell lines

SAM CA for BT20 cancer cells		ELISA results of BT20 cancer cells	
Dox treated	Control (Untreated)	Dox treated	Control (Untreated)
17.47	11.20	4.4091	4.258
15.10	12.20	5.0152	4.106
15.88	9.51	5.3182	3.652
17.47	10.59	5.3182	3.5
14.42	8.69	5.6212	4.409
15.88	8.99	5.6212	4.106
		6.0758	4.864
		6.9848	5.773

Reproduced with permission from ref. [29]. Copyright 2019, American Chemical Society

Similarly, Figure 4.12 C also shows a higher concentration of H_2O_2 (15.2 μM) (n = 3) in Dox treated 4T1 cancer cell lines (Table 4.3) compared to the untreated same cancer cell lines (11.9 μM) (n = 3). Applying calibration SAM CA curves for Dox treated and untreated 4T1 cell lines, (Figure 4.12), the measured H_2O_2 concentrations from these two samples are statistically significant with p = 0.0182. Similarly, H_2O_2 in 48-hr Dox-treated 4T1 cancer cell was calculated to be 15.2± 1.0 μM compared with 11.9 ± 1.0 μM H_2O_2 in untreated 4T1 cancer cell lines. Figure 4.12A shows the raw data of untreated 4T1 cancer cell lines under standard addition method of CA with its calibration curve as shown in Figure 4.12B whereas Figure 4.12 C displays the raw data of 48-hr Dox-treated 4T1 cancer cell lines with its calibration curve in Figure 4.12 D.

Table 4.3: Measured H_2O_2 concentrations (μM) from Dox treated and untreated 4T1 cancer cell lines

SAM CA for 4T1 cancer cell lines	
Dox treated	Control (untreated)
16.0	10.7
14.0	12.5
15.6	12.5

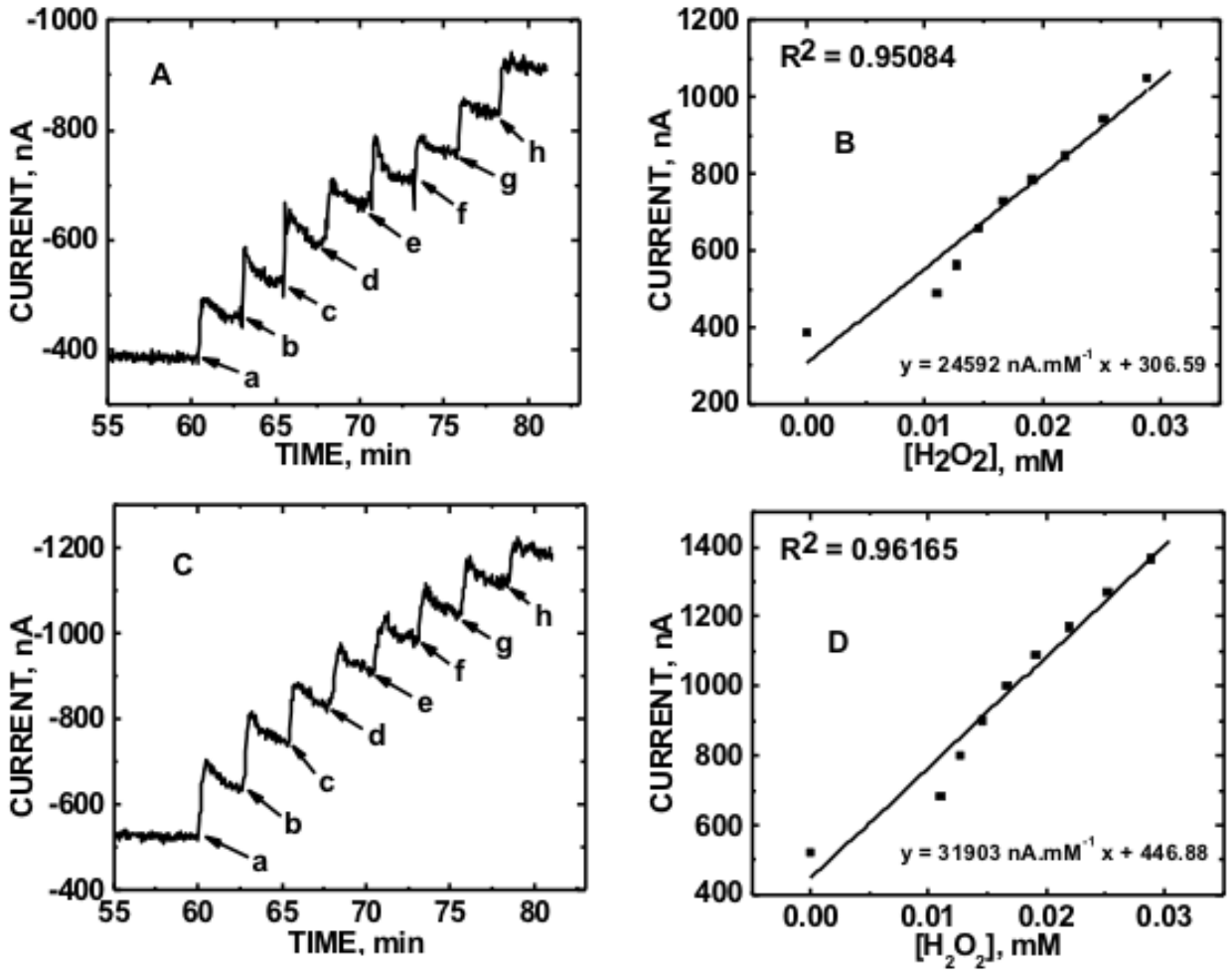

Figure 4.12: Applying the method of standard additions to detect H_2O_2 in 4T1 cancer cell lines using CA in aqueous media (A) raw data of untreated 4T1 cancer cell lines, (B) calibration curve of untreated 4T1 cancer cell lines, (C) raw data of Dox-treated 4T1 cancer cell lines and (D) calibration curve of Dox-treated 4T1 cancer cell lines
Reproduced with permission from ref. [29]. Copyright 2019, American Chemical Society

These measurements are in excellent agreement in the pattern of H_2O_2 concentration in both Dox treated and untreated BT20 cancer cell lines with those of conventional ELISA method (Table 4.2) (n = 8) as shown in Figure 4.13 B. However, the results indicate that the quantification of H_2O_2 under Nafion^{TM}/PB/ZnO/COOH-MWNTs/GCE is observed to be more sensitive (~2.5 times) than that of ELISA. Since H_2O_2 is relatively unstable compound, this needs to be detected quickly. The standard addition method under chronoamperometry is not only significantly faster

but also more sensitive to analyze H_2O_2 compared to ELISA method. In addition, the fluorescent compounds used in ELISA techniques hinder the detection of H_2O_2 in the cancer cell lines. These may be possible reasons of appearing lower concentrations of H_2O_2 under ELISA analysis. The handling of H_2O_2 samples with longer time periods may also reduce the concentration of H_2O_2 in ELISA method. In addition, H_2O_2 more rapidly decomposes in the presence of 4T1 cancer cell lines compared to BT20 cancer cell lines and PBS with the injection of 3 mM H_2O_2 in chronoamperometry as shown in Figure 4.13 D. Although H_2O_2 decomposes more rapidly in 4T1 cancer cell lines as compared to BT20, our method can still detect differences in production of H_2O_2 with the untreated and Dox treated 4T1 cancer cell lines since there is superior sensitivity offered by CA as compared to ELISA. In contrast, the ELISA technique did not differentiate between the Dox-treated and untreated 4T1 cell lines.

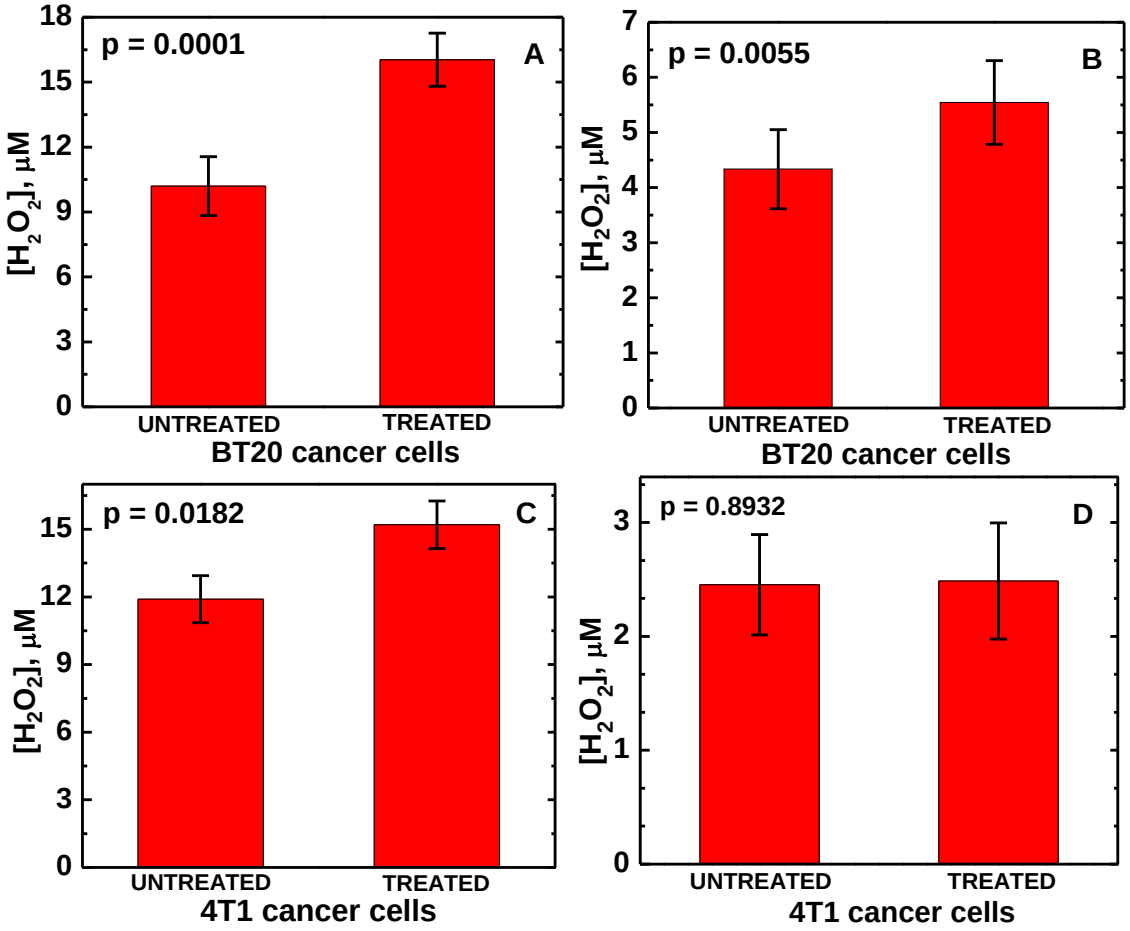

Figure 4.13: Comparison of concentrations of H_2O_2 in Dox-treated and untreated cancer cells. The bar graphs summarize measurements of H_2O_2 release from (A) BT20 cells with CA SAM, (B) BT20 cells with ELISA, (C) 4T1 cells with SAM CA, and (D) 4T1 cells with ELISA

Reproduced with permission from ref. [29]. Copyright 2019, American Chemical Society

SAM CA is not only significantly faster than ELISA but also more sensitive for analyzing H_2O_2 as compared to ELISA. This improved assaying capability of SAM CA relative to ELISA is further corroborated by control measurements of 3 mM H_2O_2 within the BT20 and 4T1 cellular environment (Figure 4.13 A). A critical difference between the assaying techniques is analysis time. It should be noted that ELISA takes approximately 3 h to quantify the H_2O_2 in these cell media. In contrast, the SAM CA procedure for H_2O_2, employing the method of standard additions, takes 15−20 min to perform the aforementioned eight standard additions for

each concentration determination, which is a substantial decrease in analysis time during which H_2O_2 would decompose in the cancer cell media, hampering ROS mechanistic analysis. This substantial reduction in analysis time permits assaying before appreciable amounts of the H_2O_2 analyte decompose. In addition, fluorescent compounds inherent to ELISA may contribute to H_2O_2 decomposition, resulting in lowered H_2O_2 readings. SAM CA is able to detect changes in H_2O_2 undetectable by ELISA in the 4T1 cell line due to rapid decomposition of H_2O_2 by these cell lines. Within the control CA experiment, current emanates from a 3 mM concentration of H_2O_2 in the presence of PBS solution, BT20, and 4T1 cell lines as a function of time (Figure 4.14), respectively. H_2O_2 more rapidly decomposes in the presence of 4T1 and BT20 cancer cells than in PBS solution. The rate of decomposition is in descending order: 4T1 > BT-20 > PBS. Although H_2O_2 decomposes more rapidly in the 4T1 cancer cell line as compared to BT20, SAM CA can still detect differences in production of H_2O_2 with the untreated and Dox-treated 4T1 cancer cells. In contrast, ELISA is not able to differentiate differences in H_2O_2 release between the Dox- treated and untreated 4T1 cells (Figure 4.13 D).

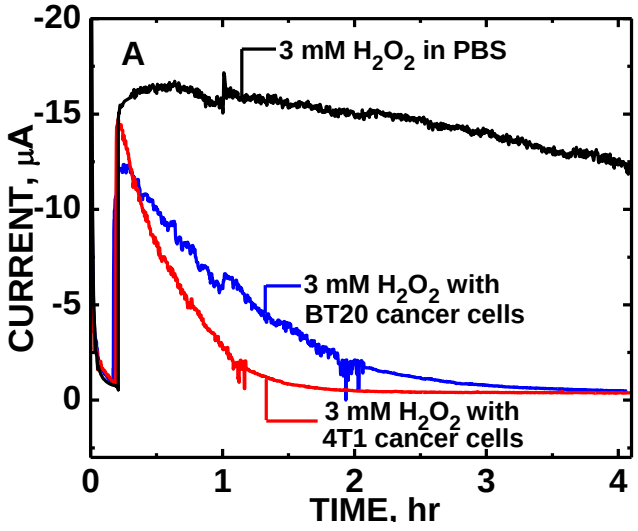

Figure 4.14: A control CA study of H_2O_2 decomposition in PBS, BT20, and 4T1 cancer cells upon addition of 3 mM H_2O_2 (A). Real time CA measurements of H_2O_2 were made using the PB/ZnO/COOH-MWNT sensor

Reproduced with permission from ref. [29]. Copyright 2019, American Chemical Society

The CA (Figure 4.15) displays excellent selectivity of the composite, Nafion^{TM}/PB/ZnO/COOH-MWNT/GCE against various interfering analytes. Injection of a 1.0 mM H_2O_2 resulted in a significant increase of current at the 62 min time point. Subsequent additions of 1.0 mM UA, 1.0 mM AA, 1.0 mM APAP, 1.0 mM FA, and 1.0 mM UA at 2 min time intervals, resulted in no signal (observable current), explaining composite's selectivity for H_2O_2. Eventually, at the 77 min time point, 1.0 mM H_2O_2 was added in the electrochemical cell, resulting in increase of additional current without losing selectivity.

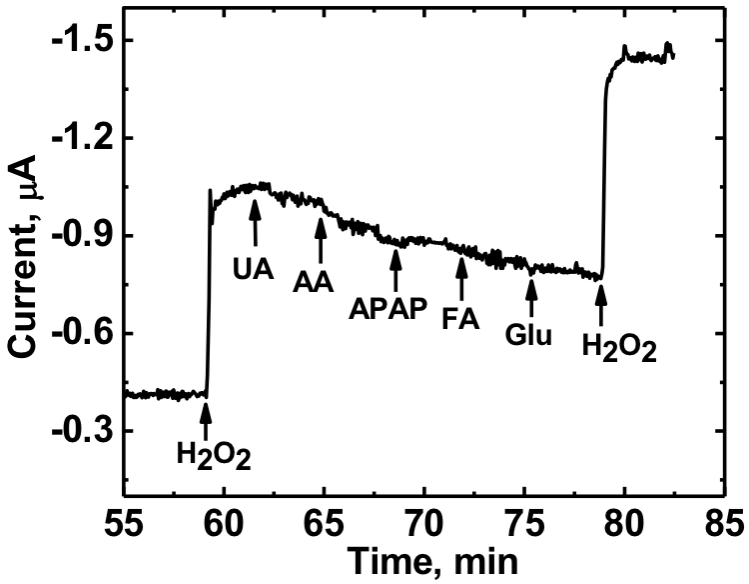

Figure 4.15: CA selectivity study of H_2O_2 using PB/ZnO/COOH-MWNTs at pH 7.4 with a 50 $mV \cdot s^{-1}$ scan rate.

Reproduced with permission from ref. [29]. Copyright 2019, American Chemical Society

4.4 Conclusions

In summary, the PB/ZnO/COOH-MWNT composite demonstrated high electrocatalytic activity toward the reduction of H_2O_2 in the 1μM to 3mM range. CA SAM was effective for measuring H_2O_2 within the 1−21 μM range. The potential application of the sensor for selective determination of H_2O_2 was studied in the presence of interfering analytes such as UA, AA, APAP, FA, and Glu. SAM CA was applied successfully in BT20 and 4T1 cancer cells to monitor H_2O_2 in Dox-treated and untreated cancer cells for monitoring oxidative stress in cancer cells. The SAM CA technique offers advantages over conventional ELISA in that it is more rapid and does not require external fluorescent compounds which may alter the sample matrix. Due to the method's ability to bypass matrix effects for H_2O_2 quantitation, the procedure should prove to be an important arsenal to quantify oxidative stress in breast cancer cell resistance to apoptosis, an understanding of which is important for advancing practical chemotherapy treatments.

CHAPTER 5

Electrochemically-assisted Assays to Measure Reactive Oxygen Species (ROS) and Glutathione from Oxidatively-Stressed BT20 Cells

Abstract

In this study, we develop a new electrochemical approach to study the interplay between oxidative stress and cell viability via ROS measurements. A zinc oxide carbon nanotube composite applied to a glassy carbon working electrode will be used to achieve these assays. The technique has the advantage of rapid ROS assaying without cell matrix effects or incorporation of fluorescent labeling dyes that would otherwise skew ROS concentration determinations. Oxidative stress will be triggered by addition of carbonyl cyanide 3-chlorophenylhydrazone (CCCP) to target the mitochondria. Flow cytometry is used to quantify cell viability in conjunction with electrochemical measurements.

5.1 Introduction

H_2O_2 has been the major redox metabolite in redox sensing, signaling and redox regulation. H_2O_2 diffuses through cells and tissues to initiate immediate cellular effects including cell shape alterations, initiation of proliferation and recruitment of immune cells. Hydrogen peroxide is a key metabolite in oxidative stress [145]. Many serious diseases involve oxidative stress, a condition in which excess reactive oxygen species (ROS) cause cell and tissue damage. An imbalance between production of free radicals and reactive metabolites (reactive oxygen species) indicates oxidative stress. Products of a normal cellular metabolism are reactive oxygen species (ROS). Such ROS is important in stimulation of signaling pathways in plant and animal cells in response to changes in intra- and extracellular environmental situations. Continued oxidative stress in cells results in chronic inflammation leading to most chronic diseases, such as

cancer, diabetes, cardiovascular, neurological and pulmonary diseases. In fact, cancer initiation and propagation has been associated with oxidative stress by rising DNA mutation or increasing DNA damage, genome instability and cell proliferation. ROS are involved in all three stages of cancer. Therefore, it is tumorigenic by virtue of their capacity to enhance cell proliferation, survival and cellular migration [129]. Cellular injury activates many responses, such as cell death, proliferation, repair and adaptation. To control tissue homeostasis and the pathophysiologic process of neurologic disorders, such as Parkinson's disease, Alzeimer's disease, amyotrophic lateral sclerosis, Huntington's disease. A genetically regulated form of cell death is called apoptosis. It refers to the programmed cell death. It involves in various biological processes including embryogenesis, ageing and other diseases. Apoptosis explains the orchestrated collapse of a cell characterized by membrane blebbing, cell shrinkage, condensation of chromatin, and fragmentation of DNA followed by rapid engulfment of the corpse by neighboring cells. Various existing treatments such as non-steroidal anti-inflammatories and anticancer treatments can be performed through apoptosis. It differs from necrosis, in which a cell is damaged by an external force, such as poison, a bodily injury, an infection or loss of blood supply. This might be due to a heart attack or stroke [146]. Using electron microscopic analysis, necrosis shows cell swelling and damage of cell morphology with the discharge of intracellular organelles whereas apoptotic cell death explains specific morphological changes with chromatin condensation, cell shrinkage, DNA fragmentation, chromatin condensation, membrane blebbing. During the early phase of apoptosis, phosphatidylserine (PS) almost totally trapped to the inner layer of phospholipid plasma membrane is shifted to the outer leaflet of the plasma membrane. This process takes place by the decreased ATP-dependent translocase activity and the increased calcium-dependent scramblase activity without violating the plasma membrane integrity. Fluorescein isothionate (FITC)-conjugated

annexin-V, which is a Ca^{+2} dependent phospholipid binding protein, is applied as a responsible marker for PS exposure. During the late phase of apoptosis, a movement from tightly to loosely packing of the plasma membrane phospholipids with PS externalization permits propidium iodide (PI) penetration into the cells and binding with DNA. Double staining of cells with FITC-Annexin-V and PI under the flow cytometry method has been verified to be a valuable method to distinguish between the early and late phase of apoptosis. Alternations in morphology of the apoptotic cell can also be studied by flow cytometry based on change in light scattering properties, side scattering (SSC) and forward scattering (FSC) [147].

Electron transfer chain (ETC) is the source used for endogenous OS generation in response to a small mitochondrial depolarization, and ETC inhibition reduces ROS and transient K_{ca} current. Nanomolar carbonyl cyanide m-chlorophenylhydrazone (CCCP) generates ROS by inducing small mitochondrial depolarization, elevated ROS and activated transient K_{ca} current. However, the micromolar CCCP, an electron transport chain blocker, induced a large mitochondrial depolarization, reduced ROS, and inhibited transient K_{ca} current [148]. The CCCP prohibit oxidative phosphorylation and an abnormal mitochondrial membrane potential occurs. This causes the destruction of mitochondria and finally apoptosis. Cell damage caused by CCCP is accompanied by an increase in ROS. To understand the role of CCCP on cell damage and apoptosis during long-term incubation, the effects of various concentrations of CCCP on cell damage and apoptosis at various incubation times need to be studied [149]. Park et al. [150] reported that CCCP induced mitochondrial dysfunction in a concentration-dependent manner in SH-SYSY cells. The treatment of CCCP not only significantly reduced mitochondrial membrane potential (MMP) in a concentration dependent manner but also significantly reduced ATP levels compared to control

(DMSO) or control cells. The CCCP treatment is provided to control the degree of apoptosis systematically.

Glutathione (GSH) is the non-enzymatic intracellular antioxidant found in most forms of aerobic cells. The antioxidative activity of GSH is due to electron transfer to reduce H_2O_2 to H_2O and O_2 whereas GSH is oxidized into GSH disulphide (GSSG). To reproduce GSH for cellular antioxidative protection, GSSG is reduced to GSH by glutathione reductase with the help of NADPH [151]. Reduced GSH is the highly available form of GSH present in millimolar concentrations in mammalian cells under normal conditions. In this condition, the ratio of reduced to oxidized glutathione (GSH/GSSG) ratio generally exists high (>10:1). The prolonged exposure of cells to oxidative stress reduces the GSH/GSSG ratio because of decreased amount of GSH, resulting in the ratio value of 1:1 [152]. In the human body, the antioxidant properties of glutathione (GSH) is able to scavenge physiological free radicals related with inflammatory disorders. Therefore, alternations in physiological glutathione concentrations have been associated with various kinds of cancers, Alzeimer's disease, Parkinson's disease and aging. The normal level of glutathione in human whole blood is in millimolar range whereas it is in micromolar range in serum. Serum glutathione concentrations are related with cancer [153]. Bola Sadashiva et al. [154] explains that cancerous samples have 152 or 156 µM GSH±25.34 or 23.33 compared to the control samples with 196 µM GSH ±18.32. Tsai et al. [155] also reports a decrease in GSH/ GSSG ratio in the blood of breast cancer patients. Due to the correlation between various diseases such as cancer and glutathione concentrations, it is required to monitor glutathione level in physiological system for medical diagnostics. Therefore, the quantification of GSH and GSSG in blood are considered as a useful marker of diseases in humans.

In this study, we have developed approaches to study the interplay between oxidative stress and cell viability via ROS measurements in BT20 cancer cells which was described in Chapter 4. Our developed sensor can monitor oxidative stress rapidly. In addition, Electrochemical analysis of glutathione will provide more insights about the further information and treatment of cancer cells.

5.2 Materials and Methods

Prussian Blue (PB), zinc nitrate hexahydrate (98% purity), carbonyl cyanide 3-chlorophenyl hydrazone (CCCP), Annexin V-FITC apoptosis detection kit, RPMI 1640 medium were all purchased from Sigma-Aldrich (St. Louis, MO, USA). Guava easy check kit (beads) and Guava ICF instrument cleaning fluid were purchased from Luminex corporation (12212 technology Blvd, Austin, TX 78727). Dulbecco's phosphate buffered solution (DPBS) was obtained from Lonza (Walkersville, MD, USA) and trypsin was received from Corning (mediatech, Inc. Manassas, VA 20109). Fetal bovine serum (FBS) was brought from Takara Bio. USA Inc. (1290 Terra Bella Avenue, Mountain View, CA 94043, USA) and 1% penicillin/streptomycin and hydrogen peroxide (H_2O_2) (30%) were obtained from Fisher Scientific (Fair Lawn, New Jersey, USA). Trypan blue solution was purchased from Hyclone Laboratories (925 West 1800 South Logan, Utah 84321). The cell culture container was bought from VWR lifesciences and cryo vials were obtained from Globe Scientific Inc. (400 corporate drive, Mahwah, New Jersey, 07430). Absolute anhydrous ethyl alcohol (AAEA) was purchased from Pharmco-AAPER (Shelbyville, KY, USA). Nafion^{TM} binder was obtained from Ion Power, Inc, (New Castle, DE, USA). Phosphate buffer solution (PBS) was used as the medium to manage the pH of the electrochemical cell. All chemical reagents were of 99.9% purity or greater and obtained from Sigma-Aldrich (St. Louis, MO, USA). All experiments were conducted in deoxygenated

electrolyte solution prepared by bubbling 99.9% purity N_2 gas flow (Air Gas Products, Radnor, PA, USA) through the solution for 12 min prior to each measurement. The preparation of all solutions was done using Millipore water (18 MΩ·cm). on the other hand, flow cytometer is used to study the apoptosis of BT20 cells.

5.2.1 Cell Culture

BT20 cells were purchased from American Type Culture Collection (ATCC, Manassas, VA, USA). This cell line was maintained in RPMI-1640 medium (Sigma-Aldrich, St. Louis, MO, USA) with 10% Fetal Bovine Serum (FBS) (Gibco) and 1% Penicillin/Streptomycin at 37^{o}C with 5% CO_2. The medium was renewed every two days. Well-grown BT20 cells in the logarithmic phase were digested by 0.25% (w/v) trypsin (Fisher Scientific, Hampton, NH, USA) from the original culture flask and mixed well before being seeded on a 6-well cell culture plate (Denville Scientific, Metuchen, NJ, USA) in the density of 1×10^6 cells/mL and incubated with the same full medium at 37^{o}C with 5% CO_2 for 24 h. Then medium was removed inside the tissue culture hood where all the cells were attached at the bottom of the well. 2 mL of various concentration of CCCP prepared in RPMI-1640 medium was treated with cells in each well for 24 hrs. The cells treated with medium only and no CCCP of vehicle only served as a negative control. The CCCP treated group and control group each had three replicate wells. After 24 h of incubation, 500 μL of the cell medium was collected from each well and proceeded for apoptosis study.

5.2.2 Flow Cytometry

In flow cytometry, it works on the principle of the passage of cells in a single file in front of a laser so that they can be detected, counted and sorted. This technique works on the principle of light scattering and fluorescence emission by the specific fluorescent probe-labelled cells as

they pass through a laser beam. The Guava EasyCyte system operates easily with minimal maintenance. The power switch, sample loader, and waste and cleaning solution vials are the only instrument components that should be routinely handled. The most of the interaction is through the software via the laptop. Guava Soft 4.0 software is used for the acquisition and analysis of data. This software is used to set up and maintain the system, providing a number of assay-specific acquisition and analysis modules. The Guava InCyte module helps us to acquire and analyze upto 12 fluorescence parameters in combination with forward scatter (FSC) and side scatter (SSC) including width and time. It offers automated compensation and an instant update feature. The Guava EasyCyte is configured to detect fluorochromes or fluorochromes with similar fluorescence. Flow cytometer has up to three lasers out of a possible four options such as violet laser (405 nm), 100 mW, blue laser (488 nm), 50 mW or 150 mW, green laser (532 nm), 100 mW and red laser (652 nm), 100 mW. It contains photodiode as forward and side scatter detector. Under fluidics specification, this instrument has standard square capillary with ID of 100 µm as flow cell dimension. Sample flow rate exists between 7 µL/min to 72 µL/min. Final particle concentration of 10^4 to 10^6 cells/mL is required for accurate results under sample concentration. 10,000 cells/vial is required as the sample for our analysis.

5.2.2.1 Cleaning Procedure for Flow Cytometer

The cleaning of the instrument is important before running the actual sample. The Cleaning was performed between the assays to avoid airs and other impurities. 1.5 mL tube was filled with DI water up to the rib of the tube and another tube was filled with 750 µL of 10% bleach in ICF. After loading those tubes in the holders, Guava Clean 3.0 was run with DI water at first and then a holder was rotated to run 10% bleach solution in ICF. Again, Guava Clean 3.0 was run to clean

the instrument. The capillary tube should be observed to check air bubbles. Any air bubbles must be removed under multiple cleaning. At the end, the rotator was operated to leave water tube inside the instrument.

5.2.2.2 Flow cytometer calibration

This is required to check the status of the instruments whether it is functioning properly or not. The bead sample was resuspended in 1:20 ratio with diluent solution. It was put in rotator in 1.5 mL tube and rotator are inserted inside. The bead#, bead expiration date and expected particles/mL information are provided under the Easycheck software. After running the experiments, the particles/mL are displayed. This number should be close enough to expected particles and appear as green color. The display of such number within average 10% coefficient of variation (CV) with green color indicates that the instrument is working properly. This result suggests us to move forward for the actual analysis of BT20 cells for apoptosis study.

5.2.2.3 Apoptosis Assays

For the apoptosis assay, it is hypothesized to observe BT20 cancer cells shows an inverse relationship with the oxidative stress of cells under flow cytometer. BT-20 cancer cells with 1 x 10^6 cells/mL suspensions are treated with various concentration of CCCP for 24 hrs in the incubator to induce apoptosis. A control of BT20 cells at 1 x 10^6 cells per mL for a zero time data point are also established. After incubating these cells for 24 hrs, cells are washed twice with DPBS. Then, cells are resuspended in 1 x binding buffer at a concentration of approximately 1 x 10^6 cells/mL. 500 µL of the apoptotic cell suspension is added to a 1.5 mL vial. Similarly, 500 µL of the non-induced cell suspension is added to the 1.5 mL of vial. 5 µL of Annexin V FITC conjugate and 10 µL of propidium iodide (PI) solution is added to each cell suspension. The vials are incubated at room temperature for exactly 10 minutes and are protected from light. Finally,

fluorescence of the cells is determined immediately with a flow cytometer. Cells, which are early in the apoptotic process, will stain with the Annexin V FITC conjugate alone. Live cells will show no staining by either the propidium iodide solution or Annexin V FITC conjugate. Necrotic cells will be stained by both the propidium iodide solution and Annexin V FITC conjugate.

Our sensor (PB/ZnO/COOH-MWNTs) is able to quantify H_2O_2 and Glutathione (GSH), biomarkers of oxidative stress. The relationship between oxidative stress and apoptosis of the cells will be delineated in detail for this flow cytometer study.

PB/ZnO/COOH-MWNTs composite was fabricated for the biochemical detection of glutathione (GSH). ZnO nanoparticles were tethered to COOH-MWNTs using sonication process and finally attached to PB using PZC concept. The current response versus various concentration of GSH was measured using chronoamperometry. Different parameters, including sonication time, pH and loading were varied for the best current response. The composite with optimum current response was formed using a 60-min sonication time and 5 hours stirring at pH 7.0. Good selectivity with a limit of detection of ($3.6_{7}\pm0.1_{57}$) µM and dynamic range of 100µM – 5 mM for GSH is presented, applicable for studying oxidative stress of cells. The sensor was selective to GSH in presence of other interfering analytes. GSH was demonstrated in the following sections that the composite (PB/ZnO/COOH-MWNTs) works in PBS first before moving onto BT20 cell medium.

5.3 Introduction

Thiols offer regulatory extracellular and intracellular functions, important to living organisms. Glutathione, a combination of three peptides of glutamate, cysteine and glycine is considered crucial for reducing oxidative stress of cells and maintaining redox homeostasis that is vital for cell growth. Sulfhydryl reduced form and disulfide oxidized form represent the redox

equilibrium of GSH. GSH takes part in many important biological functions that involve protein and DNA synthesis, bioreductive reactions, enzyme activity, amino acid transport, protein against oxidative/nitrosative stress and detoxification of metabolism [156-159]. It is reported that concentration of GSH in plasma is 4.1 mM by high performance liquid chromatography and that of GSH by porous nickel oxide microflower sensor is 4.7 mM in human plasma [160, 161]. GSH is considered as the key biomarker for various diseases and cancers due to its various amount of GSH from its normal level in micromolar to millimolar concentration available in biological cells. The changes in physiological GSH concentration is responsible for many diseases such as Alzeimer, Parkinson, diabetes mellitus, aging, HIV and cancers [162]. Glutathione is universally distributed in animal tissues, microorganisms and plants. It is normally available in high concentration (0.1 – 10) mM [163]. In most cells, GSH concentration is about 1 – 2 mM [164]. The basal GSH level of human alveolar epithelial cell line, A549 contains 150 µM GSH [165-167]. In addition, Raman et al. reports that the basal GSH level in epithelial lining fluid in non-smokers is observed to be (200-400) µM GSH whereas the concentration of GSH in epithelial lining fluid for smokers is found to be in the range of (400 – 600) µM GSH [165, 168, 169].

Various methods such as spectrophotometry [170], spectrofluorometry [171-173], high performance liquid chromatography [174, 175], capillary zone electrophoresis [176], enzymatic methods [177], electrochemical methods [178, 179] have been used to study GSH. The analysis of GSH mainly depends on many parameters such as LOD, sensitivity, selectivity, cost effectiveness and analysis time. Though CE and HPLC techniques are advanced techniques with regard to LOD of GSH. However, there are serious concerns in terms of cost effectiveness, analysis time and selectivity. Out of these techniques, electrochemical methods provide many merits excluding LOD. In this study, after successfully tethering Prussian Blue (PB) on the surface of ZnO/COOH-

MWNTs, we explore, for the first time, the utility of a PB/ZnO/COOH-MWNT composite for assaying GSH using chronoamperometry.

5.3.1 Results and Discussion

The electrochemical response of Nafion^{TM}/PB/ZnO/COOH-MWNTs/GCE surface with GSH was studied as control experiments. As shown in Figure 5.1, there was no electrochemical behavior to GSH on bare GCE at given potential in PBS (pH 7.0) solution. The cathodic and anodic current peaks were observed at 0.0864 V and 0.3447 V, respectively, which had a pronounced electrochemical response when GCE was modified with PB/ZnO/COOH-MWNTs as shown in Figure 5.1. Electrochemically controlled experiments were performed using ZnO/COOH-MWNTs, ZnO and PB in which our composite (PB/ZnO/COOH-MWNTs) shows the better results as shown in Figure 5.1. The increase is attributed to the proper attachment of PB, on the surface of ZnO/COOH-MWNTs.

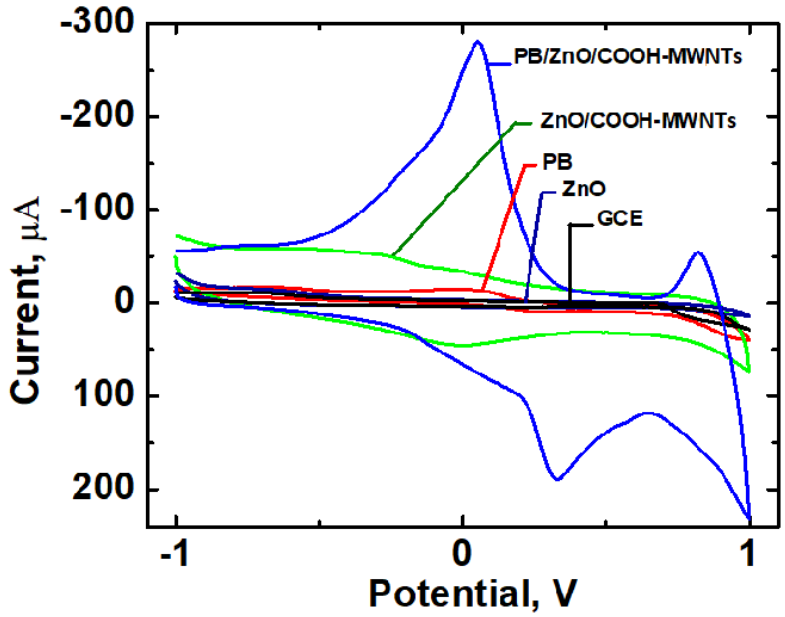

Figure 5.1: Analysis of glutathione under CV at pH 7.0 with 50 mV·s^{-1} scan rate using PB/ZnO/COOH-MWNTs, ZnO/COOH-MWNTs, ZnO, PB and GCE with 1 mM GSH

Symmetric peak shapes in the CVs at various pH conditions denoted quasi-reversible redox processes. During CV, reduced glutathione (GSH) is oxidized to glutathione disulfide (GSSG) and GSSG is reduced back to GSH [180]. Figure 5.2 shows the amperometric response of the Nafion^{TM}/PB/ZnO/COOH-MWNTs/GCE as a function of pH in 1 mM GSH at reduction and oxidation potentials of 0.0864 V and 0.3447 V, respectively; the corresponding CVs of 1 mM HVA are shown in Figure 3. The cathodic and anodic currents are maximized at pH 7.0 for both oxidation and reduction potentials. Figure 5.3 shows that our sensor is capable of detecting GSH at various pH conditions. The highest detection response of GSH was observed at acidic condition. The response of our sensor decreases as the pH of the solution moves from acidic to alkaline medium. However, we stay on pH 7.0 for our GSH analysis since it is the physiological pH.

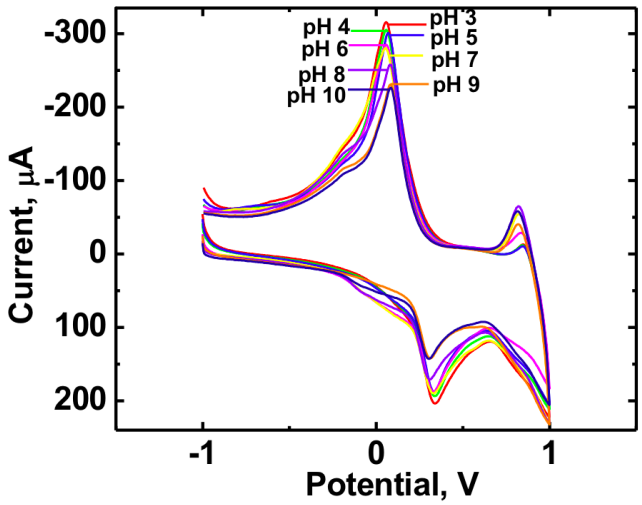

Figure 5.2: Effect of pH on 1 mM GSH using PB/ZnO/COOH-MWNTs

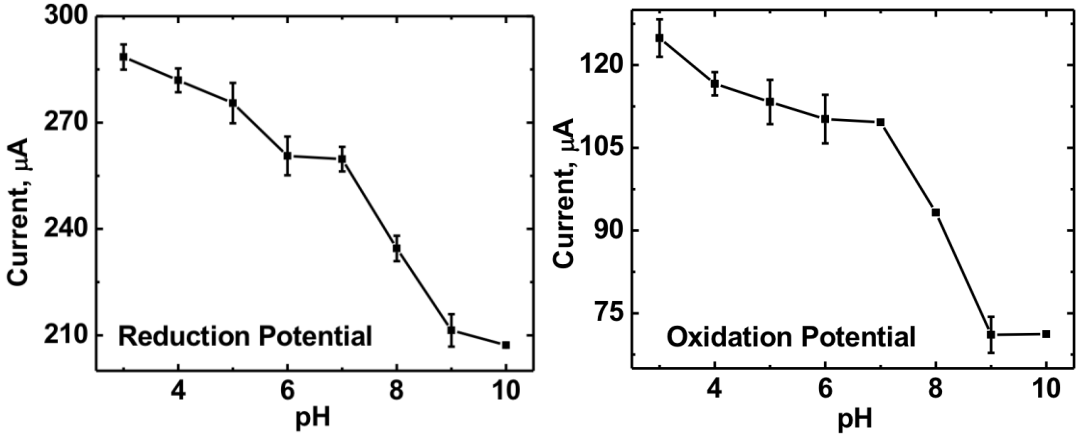

Figure 5.3: Effect of pH on GSH under oxidation and reduction potential

Figure 5.4 shows a typical current-time curve of CA at the Nafion/PB/ZnO/COOH-MWNTs modified electrodes for successive addition of various concentrations of GSH in PBS of pH 7.0 at +0.3447 V. Within 4 sec, the sensor arrived at a steady-state current. It was determined that GSH concentration can be detected as low as 100 μM with the detection limit of (3.666±0.1577) μM. Figure 4 also exhibits a linear relationship between current vs concentration with correlation coefficient, $R^2 = 0.9847$ for GSH concentrations from 100 μM to 5 mM.

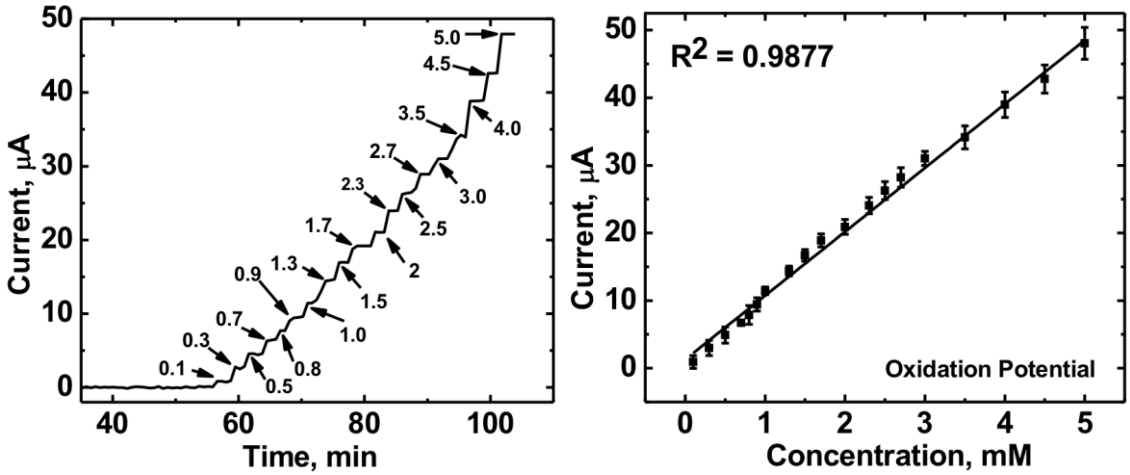

Figure 5.4: CA of PB/ZnO/COOH-MWNTs to detect (0.1-5) mM GSH at 0.3447 V with pH 7 and its calibration curve

Cyclic voltammograms of 1 mM GSH at pH 7.0 was shown in Figure 5.5. This CV was observed at different scan of 10, 20, 30, 40, 50, 60, 70, 80, 90, 100, 110, and 120 $mV \cdot s^{-1}$ using PB/ZnO/COOH-MWNTs/GCE electrode. The electrocatalytic reduction of GSH due to the effect of the potential by Nafion/PB/ZnO/COOH-MWNTs/GCE was investigated by cyclic voltammetry. The peak potential for the catalytically reduced GSH moves to increasingly negative potential with a larger scan rate. However, with the scan rates, the peak current (I_{pc}) of reduction for GSH increased linearly which indicates that the reduction reaction was diffusion controlled. The relationship between the scan rate and I_{pc} was observed to have a good linear connection over the range of 10 – 120 $mV \cdot s^{-1}$ as shown in Figure 5.6. A correlation coefficient (R^2) of 0.9997 was obtained for the linear regression equation,

$$I_{pc}\,(\mu A) = 48.36\ V^{1/2}\,(V \cdot s^{-1}) - 49.61 \quad \text{.....(1)}$$

under reduction potential. Similarly, a correlation coefficient (R^2) of 0.9948 was received for the linear regression equation,

$$I_{pc}\,(\mu A) = 11.91\ V^{1/2}\,(V \cdot s^{-1}) + 9.081 \quad \text{.....(2)}$$

under oxidation potential. Hence, the reaction of GSH with the electrode surface of Nafion/PB/ZnO/COOH-MWNTs/GCE shows good correlation with the expression of Randles-Sevçik Analysis as the I_{pc} increases linearly as a function of the square root of scan rate. The Randles-Sevçik Analysis equation explains the scan rate effect on the peak current in the CV. It is diffusion controlled reaction because reaction that takes place so quickly that the reaction rate is the transport of the reactant through the medium. It is the spontaneous transfer of electroactive species from regions of higher concentration to the regions of lower concentration.

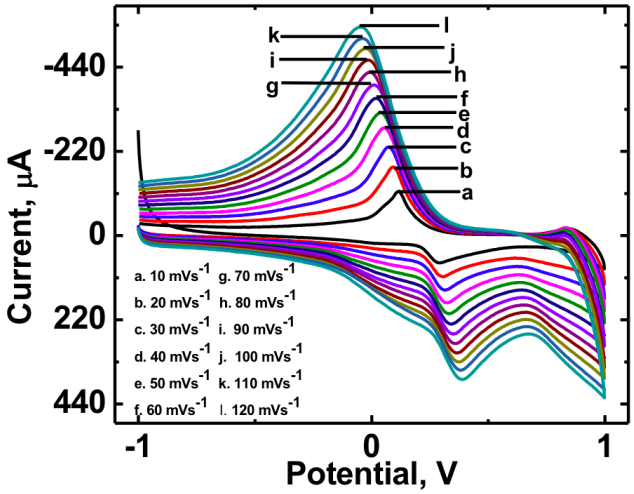

Figure 5.5: Diffusion controlled experiments of 1 mM GSH using PB/ZnO/COOH-MWNTs at pH 7

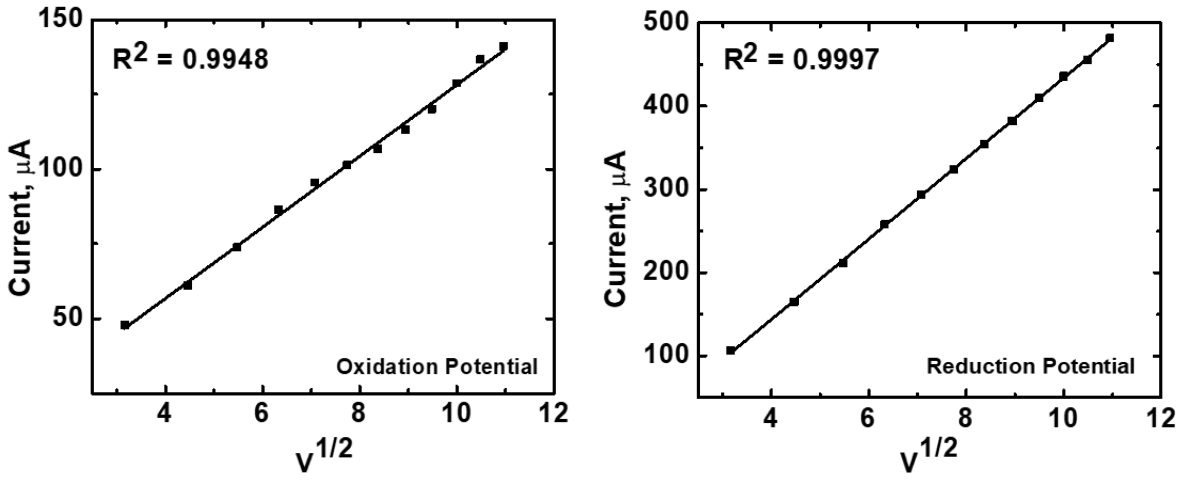

Figure 5.6: Calibration of diffusion controlled experiment of GSH using PB/ZnO/MWNTs under oxidation and reduction potential

Figure 5.7 shows the chronoamperometric responses of the Nafion/PB/ZnO/COOH-MWNTs/GCE at +0.3447 V (GSH's determined oxidation potential) versus Ag/AgCl upon sequential additions of 0.3 mM GSH, UA, Cys, H_2O_2, LA, FA, Glu, AA, APAP and GSH. These analytes were added at 27.81, 30.33, 33.39, 35.91, 38.70, 40.78, 43.10, 45.13, 47.34, 49.41 min, respectively, denoted by the arrows in Figure 7. Nafion/PB/ZnO/COOH-MWNTs could

selectively detect GSH in the presence of all of these potentially interfering analytes. No detectable current response is observed, showing that PB/ZnO/COOH-MWNTs sensor is selective to only GSH.

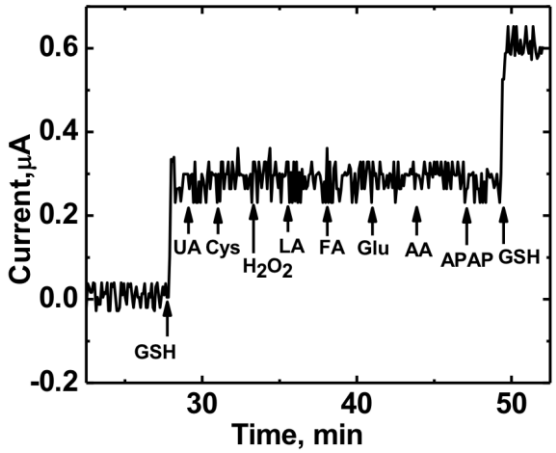

Figure 5.7: Selectivity study of 0.3 mM GSH at 0.3447 V using 5 µL PB/ZnO/COOH-MWNTS and 0.3 mM of various analytes.

PB/ZnO/COOH-MWNTs composite showed high catalytic activity for the oxidation of GSH in the range from 100 µM to 5 mM at +0.3447 V under CA. The potential application of the sensor for selective determination of GSH was studied in the presence of urine, ascorbic acid, H_2O_2, lactic acid, folic acid, glucose and acetaminophen. The good selectivity and sensitivity of GSH in presence of interfering analytes at physiological pH is useful for studying oxidative stress of cells.

5.4 Results and Discussion

Figure 5.8 shows the apoptosis results of BT20 cell and various concentrations of CCCP treated for 24 hours BT20 cells under flow cytometer experiments. A dot represents a cell. There are four quadrants, each one representing necrosis (top left), normal (down left), early apoptosis

(down right) and late apoptosis (top right). Figure 5.9 represents the raw data obtained from spiking various concentrations of CCCP treated 24 hours 1.5 mL BT20 media under SAM CA method.

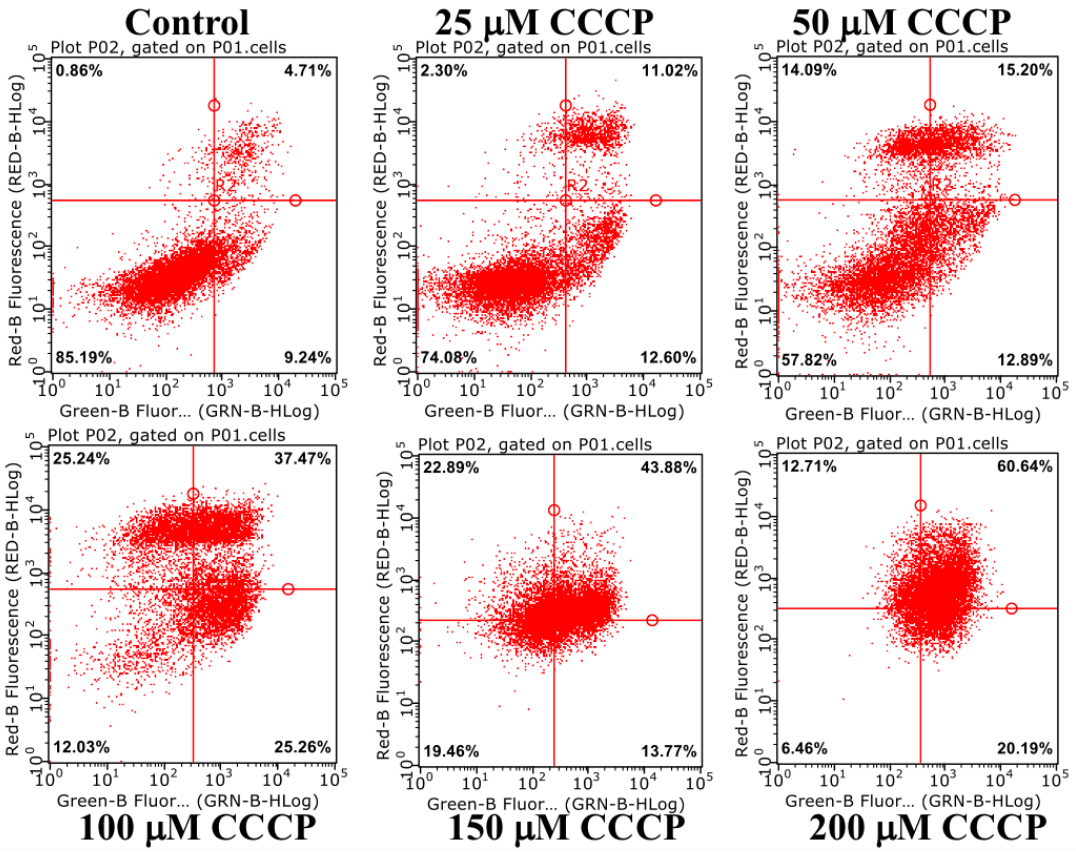

Figure 5.8: BT 20 cell apoptosis results at various concentration of CCCP 24 hrs

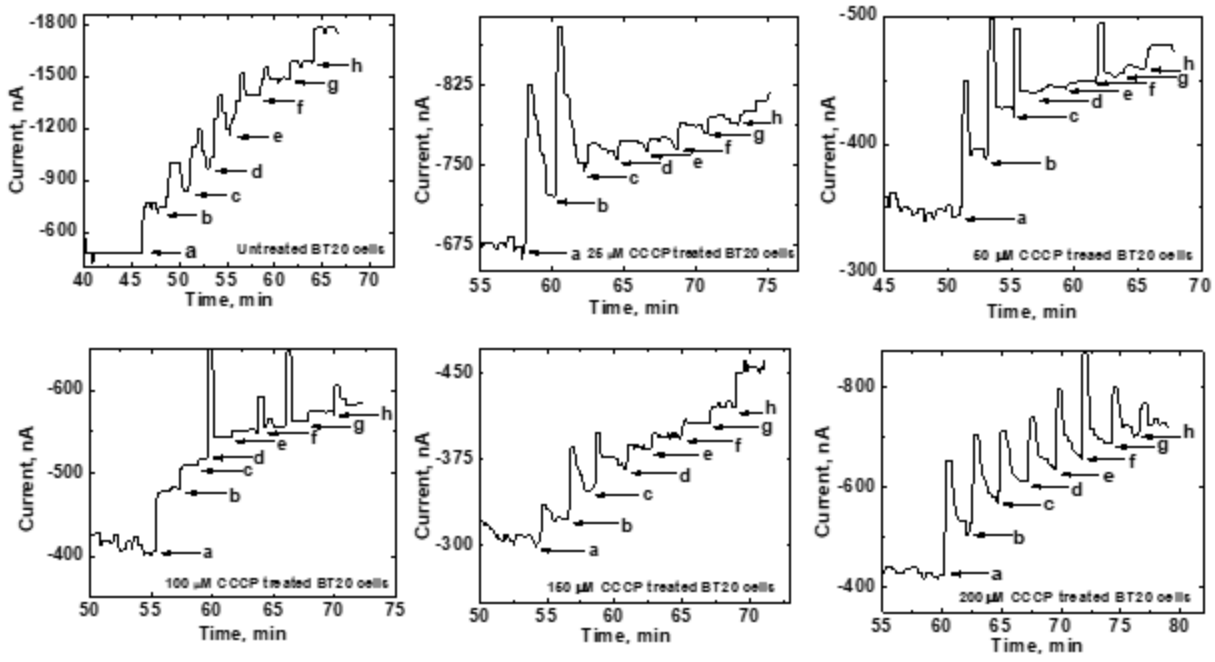

Figure 5.9: Raw data obtained from SAM CA method under spiking of (a) 11µM, (b) 12 µM, (c) 13 µM, (d) 14 µM, (e) 15 µM, (f) 16 µM, (g) 17 µM, (h) 18 µM in BT20 cells at -0.004 V under 5% filtered noise

Figure 5.10 is the CA results after spiking 1.5 mM GSH (red arrow) in the BT20 cells media to check the stability of its concentration. It is observed that the GSH concentration remain almost constant until 4 hours. It means the decomposition of GSH is almost nullified. C-myc is present in BT20 cells. It is postulated that C-myc is involved in more production of GSH in BT20 cells after spiking GSH externally. There may be certain enzymatic action to release more GSH in extracellular region and the exact mechanism is not known [181].

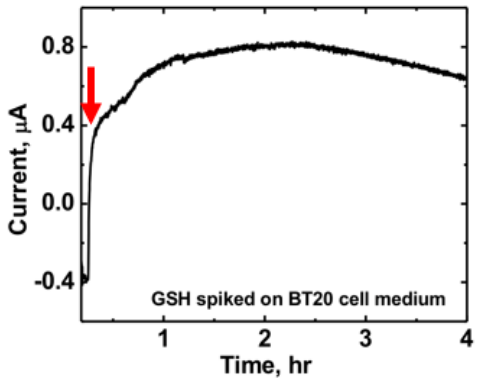

Figure 5.10: the stability of GSH in the BT20 cells after spiking 1.5 mM GSH under chronoamperometry at 0.3447 V

Figure 5.11 shows the raw CA results of GSH response at 0.3447 V after spiking control and various CCCP treated BT20 cells to the 1.5 mL PBS. Figure 5.12 shows the increasing trend of GSH current response upon higher CCCP treatment after the control experiment. Under SAM CA technique, when GSH was spiked to BT20 cells, cells respond by producing more GSH severely, hampering GSH SAM CA method. Addition of GSH is assimilating more GSH release from cells. This appears like interesting phenomena as we see increase of GSH under this method.

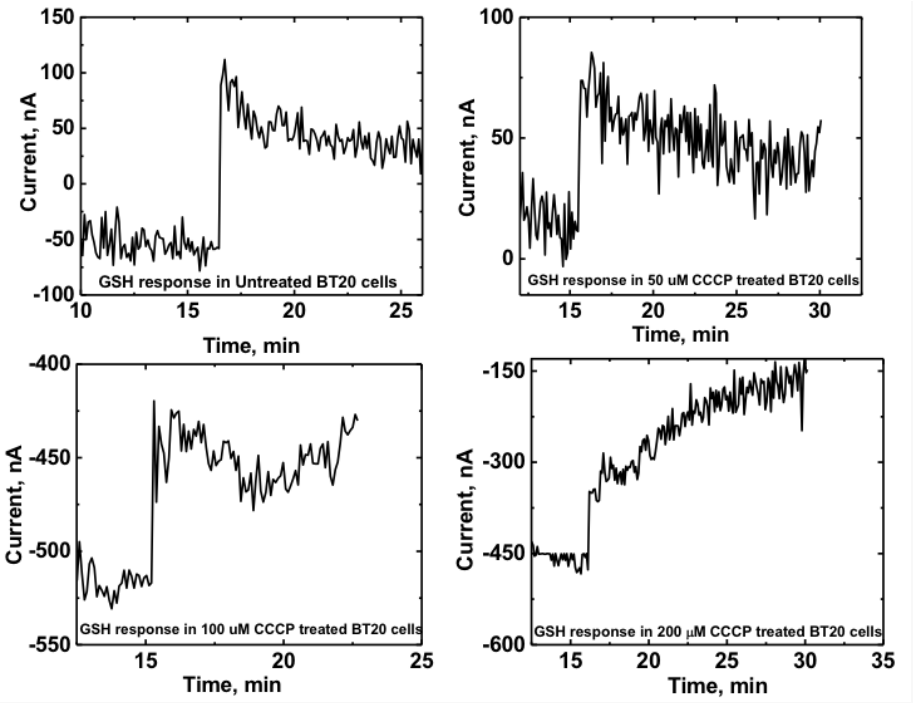

Figure 5.11: CA results of spiking control and various concentration of CCCP treated BT20 cells to the 1.5 mL PBS at 0.3447 V for GSH response

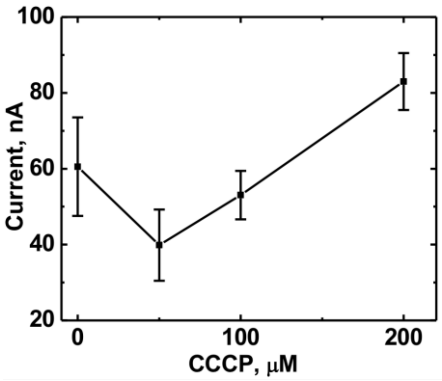

Figure 5.12: A plot of current response of GSH at various concentration of CCCP treated BT 20 cells at 0.3447 V

Table 5.3: A raw and normalized data of oxidative stress and apoptosis of BT20

		$[H_2O_2]$		Apoptosis		H_2O_2, µM
CCCP, µM	H_2O_2, µM	STD1	%Apoptosis	STD2	% live cells	norm (live)
0	5.56	1.0263	4	0.6174	96	0.05791667
25	69.05	8.4539	11.38	0.4915	88.62	0.77916949
50	47.29	5.0247	15.59	0.3651	84.41	0.56024168
100	43.46	2.9197	39	1.3347	61	0.71245902
150	38.41	1.5225	42.33	1.8471	57.67	0.66603087
200	29.53	3.9971	62.33	2.0357	37.67	0.78391293
300	32.51	5.7372	37.32	1.2055	62.68	0.51866624

	[GSH]		
CCCP, µM	nA	STD	offset
0	60.541	13.16	0.030638
50	39.858	9.422	-0.1278
100	53.045	6.403	0.319794
200	83	7.55	1.603345

Sample calculation of H_2O_2 normalized using the values of Table 5.3:

For untreated BT20 cells without using CCCP for 24 hours,

% apoptosis obtained from flow cytometer experiment = 4%

Calculated Concentration of H_2O_2 under SAM CA = 5.56 µM

% live cells = (100-4) = 96%

Normalized H_2O_2 concentration of H_2O_2 = 5.56/96 = 0.0579 µM

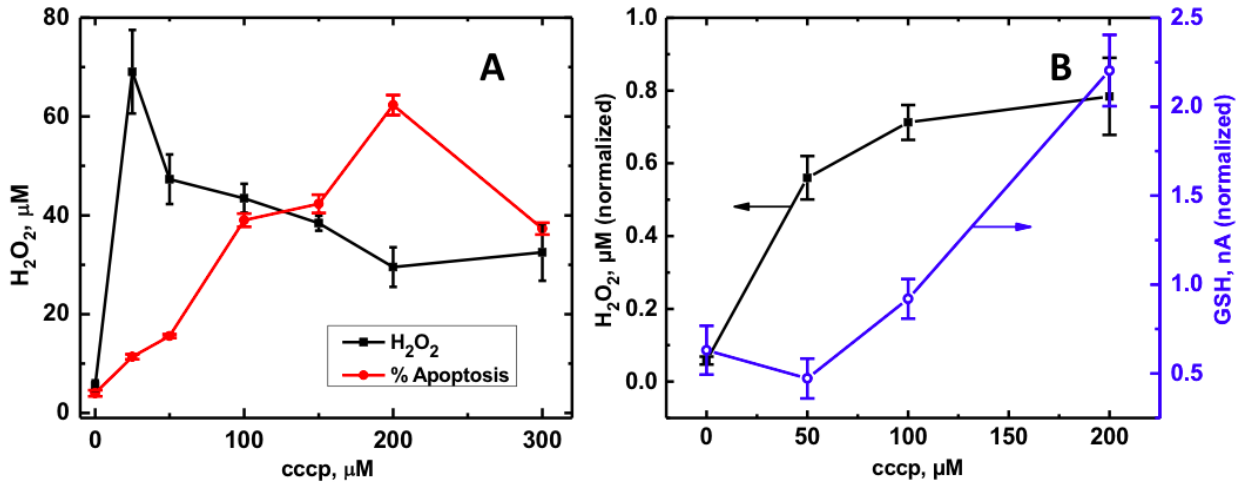

Figure 5.13: ROS and GSH generated from oxidatively-stressed BT-20 cells. **(A)** H_2O_2 concentrations from CA SAM measurements (unnormalized) and percent apoptosis as a function of CCCP dosage; **(B)** H_2O_2 and GSH release divided by percent viable cells for normalization

Figure 5.13A demonstrates the relationship between oxidative stress as indicated by the production of H_2O_2 and the % apoptosis under various concentrations of CCCP treated BT20 cells for 24 hrs. It is observed that the trend of oxidative stress and apoptosis moves in the opposite direction. Such relationship can be studied up to 200 µM CCCP treatment. Oxidative stress is higher in the cancer cells with the lower concentration treatment with CCCP. The higher the CCCP dose, the greater the apoptosis, resulting in lower oxidative stress. Although CCCP itself kills the cells, Figure 5.13B show the trend of production of H_2O_2 and GSH release divided by percent viable cells for normalization as shown in Table 3. The normalization is necessary to avoid the false positive result for our analysis to understand the relationship between oxidative stress and apoptosis. Although we can not absolutely quantify GSH, we can make relative measurements as shown in Figure 5.13 B. To further confirm the trend of GSH release from BT20 cells under various concentrations of CCCP dosage, fluorescent HPLC technique is considered. Our ultimate goal is to use F-HPLC to further make sense of normalized nano current obtained from GSH under SAM CA technique.

5.5 Conclusion

Our approach to the interplay between oxidative stress and cell viability via ROS measurements in BT20 cancer cells was studied. There is reverse relationship between oxidative stress and apoptosis under the treatment of BT20 cells from 25 μM to 200 μM of CCCP. When oxidative stress of cells goes down, the apoptosis rate increases, resulting in the increase of GSH level. So, GSH also plays vital role to reduce oxidative stress and increase the apoptosis rate.

Chapter 6

Electrochemical Detection of Dopamine Using PB/ZnO/COOH-MWNTs

Abstract

A Prussian Blue (PB) zinc oxide (ZnO) nanoparticle carboxylic acid-functionalized multiwalled carbon nanotube (PB/ZnO/COOH-MWNT) composite was fabricated for the determination of dopamine (DA). ZnO nanoparticles were tethered to COOH-MWNTs using sonication. Upon attachment of the PB to the ZnO/COOH-MWNTs, which consisted of ZnO nanoparticles 13 nm in diameter, the ZnO coalesced to larger clusters with an average diameter of 573±4nm. The current response versus various concentrations of DA was measured using chronoamperometry. The optimum conditions for DA measurements were at pH 7.0 using the oxidation current. The sensor has a linear dynamic range from 10 to 900 μM with a limit of detection of $0.378 \pm 0.01_5$ μM, suitable for practical neuroblastoma screening at the lower concentration range and process controls for polydopamine synthesis at the upper concentration range, important for modifying polymeric membranes for water purification.

6.1 Introduction

The detection of dopamine (DA) in aqueous solution has important applications for neuroblastoma screening and process control applications for polymeric membrane synthesis used in water purification. Neuroblastoma (NB) is a type of pediatric cancer. Although the percentage of incidence is 6% among 0-to-14-year-olds, of these cases, the death rate is 19%, as reported in the latest statistics [182]. A key marker for the disease is elevated DA levels in the urine. Various

carbon electrode composites have been developed to detect DA between 10 and 100 µM, suitable for detecting the onset of NB [183, 184]. Prussian Blue (PB) has been used in a many of composites to electrochemically enhance DA detection with selectivity. Yang et al. [185] used an enzyme-free molybdenum carbide Prussian blue composite to detect DA. Yi et al. [186] used a PB-modified electron to detect DA with a limit of detection of 0.01 mM for DA. Roychoudhury et al. [187] reported a label-free DA sensor using tyrosine conjugated PB-modified nickel oxide nanoparticles. While these previously reported composites were capable of assaying DA up to 120 µM, the ability to measure higher concentration ranges for practical industrial processing has not been demonstrated. Beyond the ca. 100 µM DA concentration range, there is a surge of interest in monitoring DA for polydopamine (PDA) production. PDA is essential for reinforcing membranes for water and wastewater purification, which are otherwise susceptible to fouling and degradation. The annual literature reports due to polydopamine (PDA) based membrane modifications in water purification has steadily risen by more than ten times from 2008 to 2019 [188].

Reliable DA concentration monitoring is important for reinforcing membranes to resist fouling. In particular, the ability to monitor DA concentration near 500 µM is important for understanding mechanisms (and controlling them for) governing PDA formation that involve DA self-polymerization with cyclized indolic components [189]. To maximize PDA modifications to water-filtration membranes, an understanding of the DA self-polymerization is essential. Electrochemical methods, compared to other commonly used techniques, including high-performance liquid chromatography (HPLC), absorption spectroscopy, and fluorescence, offer a more straight-forward, rapid, and more cost-effective approach for the quantification of DA [190-192]. To these ends, in this report, we show the utility of a PB zinc oxide carbon nanotube electrochemical sensing composite for assaying DA in this region with optimized sensitivity and

selectivity. A significant observation uncovered in this study, not previously seen, is the agglomeration of ZnO nanoparticles into larger clusters upon the introduction of PB to the ZnO/MWNTs.

6.2 Results and Discussion

In the CV of the 1 mM Dopamine solution in PBS, the 5-µL composite of PB/ZnO/COOH-MWNTs showed the optimum sensitivity with selectivity for DA due to the proper loading of the composite as shown in Figure 6.1.

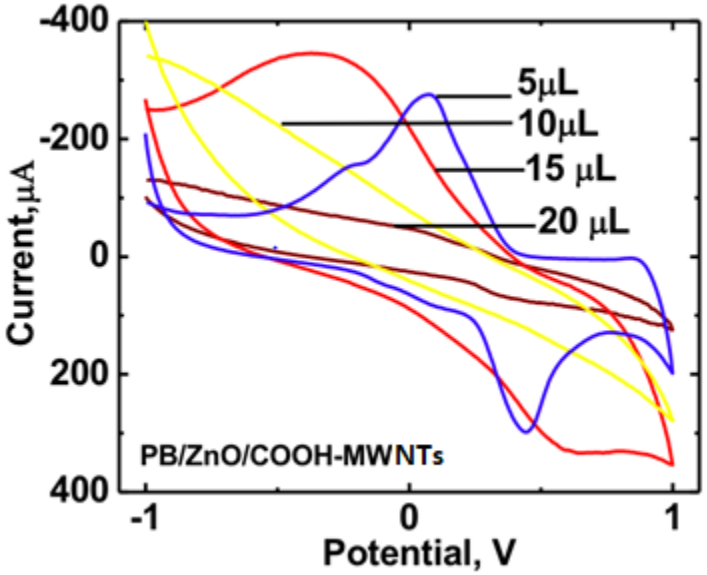

Figure 6.1: Effect of various loading of the composite,
PB/ZnO/COOH-MWNTs with DA under CV at pH 7.0 with 50 $mV \cdot s^{-1}$
Reproduced with permission from ref. [210]. Copyright 2021, Taylor & Francis

Figure 6.2 exhibits variation in CV signal as a function of different PB loadings onto the ZnO/COOH-MWNTs nanocomposite with measurements across the working electrode versus Ag/AgCl reference electrode in phosphate buffer solutions (PBS) at pH 7.0. The mass ratio (1:2) of PB/ZnO/COOH-MWNTs provides the highest electrocatalytic activity as shown in Figure 6.2.

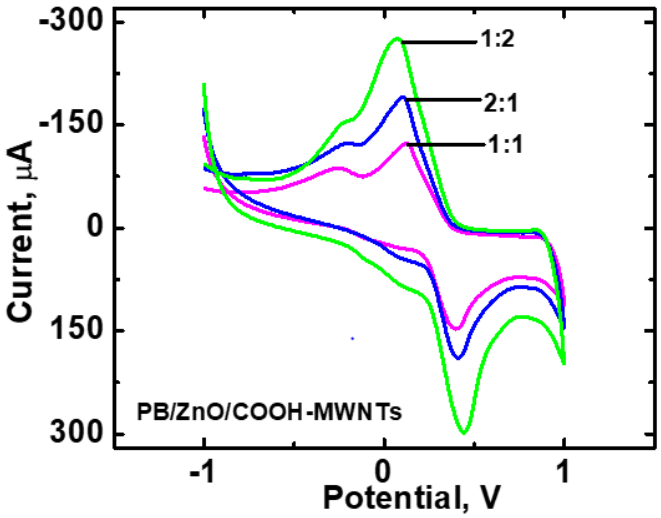

Figure 6.2: CVs of 1 mM Dopamine at pH 7.0 showing the effect of PB to ZnO/COOH-MWNTs ratios (by mass) for optimum sensitivity
Reproduced with permission from ref. [210]. Copyright 2021, Taylor & Francis

Electrochemical response of DA on Nafion/PB/ZnO/COOH-MWNTs/GCE surface was studied. As shown in Figure 6.3, there was no electrochemical behavior to DA on the bare GCE at given potential of PBS at pH 7.0 solution. The cathodic and anodic current peaks were observed at 0.0766 V and +0.438 V, respectively, which had a pronounced response when GCE was modified with PB/ZnO/COOH-MWNTs. In comparison with other electrochemical response of ZnO/COOH-MWNTs, COOH-MWNTs and PB, our composite shows better results as shown in Figure 6.3. The increase is attributed to the proper attachment of PB “artificial enzyme” on the surface of ZnO/COOH-MWNTs.

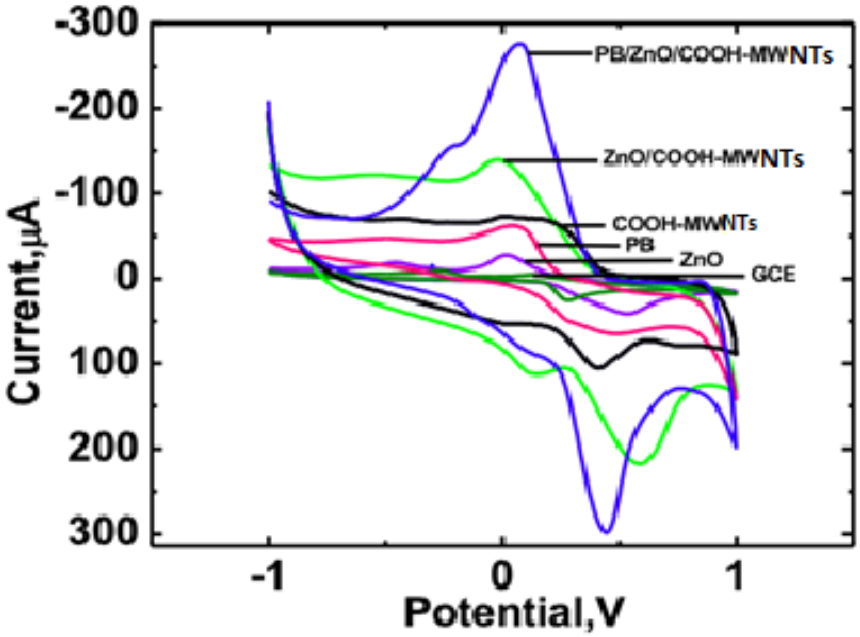

Figure 6.3: Analysis of DA under CV at pH 7.0 with a 50 $mV \cdot s^{-1}$ scan rate (a) GCE (b) ZnO, (c) PB, (d) COOH-MWNTs, (e) ZnO/COOH-MWNTs, (f) PB/ZnO/COOH-MWNTs with 1 mM DA (Control experiments)
Reproduced with permission from ref. [210]. Copyright 2021, Taylor & Francis

Figure 6.4 shows that our sensor is capable of detecting DA at various pH conditions. The optimum detection response of DA was observed from pH 6.0 to 7.0. The highest electrocatalytic activity of our sensor with DA was observed at pH 7.0 at both oxidation and reduction potentials. Symmetric peaks in the CVs at various pH conditions denoted quasi-reversible redox processes. During CV, dopamine is oxidized to dopamine-o-quinone, and dopamine-o-quinone is reduced back to dopamine via a two-electron process [183]. Figure 6.4 shows the amperometric response of the Nafion^{TM}/PB/ZnO/COOH-MWNTs/GCE as a function of pH in 1 mM DA at reduction and oxidation potentials of 0.0766 and +0.438 V vs Ag/AgCl, respectively.

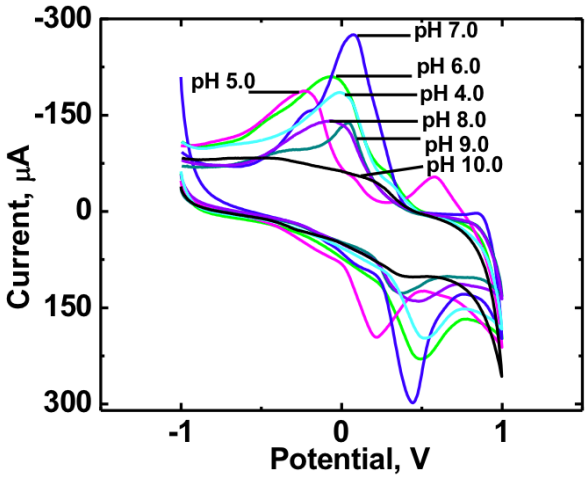

Figure 6.4: Effect of pH in the measurement of 1 mM DA at 50 $mV \cdot s^{-1}$ usingPB/ZnO/COOHMWNTs
Reproduced with permission from ref. [210]. Copyright 2021, Taylor & Francis

DA monomer is known to oxidize and undergo self-polymerization at pH values above 7 to form polydopamine [193]. As polymerization occurs under alkaline conditions, the redox chemistry of the analyte changes. We attribute the increased CV peak-to-peak height (intensity) to the formation of the polymer. At pH values of 7 and higher, the oxidation peak remains relatively stable near +0.07 V (Figure 6.4). In the weakly acidic range (pH 6.0), the DA retains its monomeric form resulting in the lowered current (due to reduced DA solution density) in the CV and a lower potential (-0.04 V).

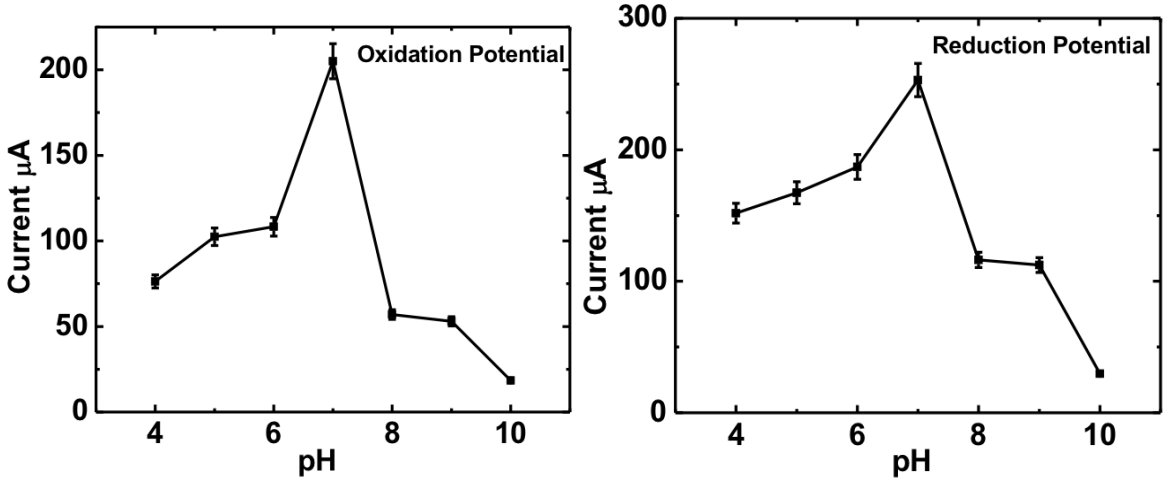

Figure 6.5: A plot of pH vs current to show optimum pH response for the highest electrocatalytic activity at pH 7.0 using CVs at reduction and oxidation potentials of 0.076 V and +0.438 V, respectively
Reproduced with permission from ref. [210]. Copyright 2021, Taylor & Francis

Figure 6.5 shows i_{pc} and i_{pa} denoting peak current obtained from reduction and oxidation CVs from 1.0 mM DA as a function of pH adjusted PBS. The maximum signal from the PB/ZnO/COOH-MWNTs from current peak maxima for both currents occurred at pH 7.0 for both oxidation and reduction potentials. Further experiments pertaining to quantitation and selectivity were then performed under these conditions, focusing on the oxidation current. This result was also observed by Yang et al. [194] biosensor, equivalent to ours, in which the pH coincided with favorable solubility for DA, noted that the solubility of DA diminishes in aqueous solution as the solvent medium becomes more alkaline.

Scheme 6.1 shows the electrochemical mechanism of DA on the surface of working electrode related to the two observed peaks in the CV data.

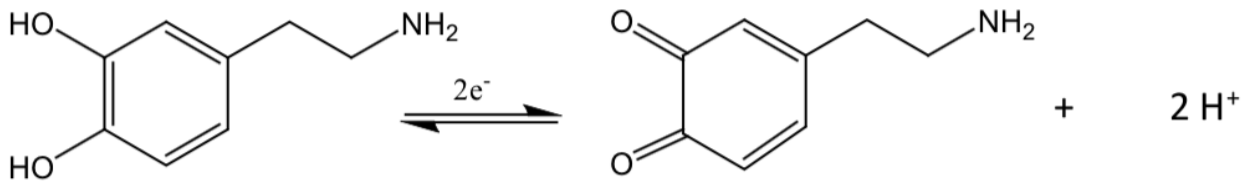

dopamine (reduced species) — dopamine-o-quinone (oxidized species)

Scheme 6.1: Reduced and oxidized forms of dopamine

Figure 6. 6 shows a typical current-time curve of CA at the Nafion/PB/ZnO/COOH-MWNTs modified electrodes for successive addition of various concentrations of DA in PBS of pH 7.0 at +0.438 V. Within 4 sec, the sensor arrived at a steady-state current. It was determined that DA concentration can be detected as low as 10 µM with the detection limit of 0.378 ± 0.015 µM. Figure 6 also exhibits a linear relationship between current vs concentration with correlation coefficient, R^2 = 0.9946 for DA concentrations from 10 µM to 900 µM.

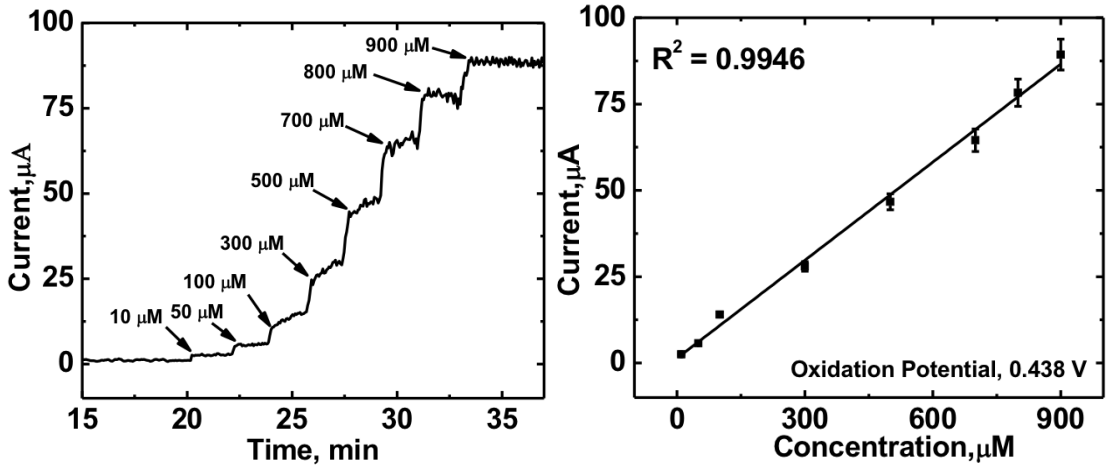

Figure 6.6: Analysis of DA under CA at pH 7.0 with 50 $mV \cdot s^{-1}$ scan rate (A) a spectrum showing the detection of DA from 10 µM to 900 µM (B) a calibration curve with R^2 = 0.9946
Reproduced with permission from ref. [210]. Copyright 2021, Taylor & Francis

6.3 Randles-Sevçik Analysis

Cyclic voltammograms of 1 mM DA at pH 7.0 was shown in Figure 6.7. This CV was observed at different scan of 10, 20, 30, 40, 50, 60, 70, 80, 90, 100, and 110 $mV{\cdot}s^{-1}$ using PB/ZnO/COOH-MWNTs/GCE electrode. The electrocatalytic reduction of DA due to the effect of the potential by Nafion/PB/ZnO/COOH-MWNTs/GCE was investigated by cyclic voltammetry. The peak potential for the catalytically reduced DA moves to increasingly negative potential with becoming scan rate larger. However, with the scan rates, the peak current (I_{pc}) of reduction for DA increased linearly which indicates that the reduction reaction was diffusion controlled. The relationship between the scan rate and I_{pc} was observed to have a good linear connection over the range of 10 – 110 $mV{\cdot}s^{-1}$ as shown in Figure 6.8. A correlation coefficient (R^2) of 0.9983 was obtained for the linear regression equation, $I_{pc}\,(\mu A) = 26.23\ V^{1/2}\,(V{\cdot}s^{-1})$ -14.92 under reduction potential. Similarly, a correlation coefficient (R^2) of 0.9912 was received for the linear regression equation, $I_{pc}\ (\mu A) = 14.58\ V^{1/2}\,(V{\cdot}s^{-1})$ +8.661 under oxidation potential. Hence, the reaction of DA with the electrode surface of Nafion/PB/ZnO/COOH-MWNTs/GCE shows good correlation with the expression of Randles-Sevçik analysis as the I_{pc} increases linearly as a function of the square root of scan rate. Randles-Sevçik Analysis equation explains the scan rate effect on the peak current in the CV. It is diffusion controlled reaction because reaction that takes place so quickly that the reaction rate is the transport of the reactant through the medium. It is the spontaneous transfer of electroactive species from regions of higher concentration to the regions of lower concentration.

The CV line shapes indicate a reversible reaction:

$$I_p = 2.69 \times 10^5 A\, D^{1/2}\, n^{3/2}\, v^{1/2} C_0 \qquad (1)$$

where I_p is the peak current in amperes, A is the electrode area (cm^2), D is the diffusion coefficient at the electrode surface ($cm^2 \cdot s$), $v^{1/2}$ is the scan rate in $V \cdot s^{-1}$, C_0 is the concentration in $mol \cdot cm^{-3}$, and n is the number of electrons involved in the redox reaction [195]. Equation (1) was employed to calculate the charged molecular diffusion coefficients for the redox processes. Diffusion coefficient calculations were prepared based on multiple CV measurements, as shown in the supporting information. The diffusion constants, D, for the oxidation and reduction processes were determined to be 2.381 x 10^{-4} $cm^2 \cdot s^{-1}$ and 7.365 x 10^{-3} $cm^2 \cdot s^{-1}$, respectively. The diffusion associated with the reduction was more significant than that for the oxidation, as denoted by the higher D value. The significance of the fact is that more amount of analytes can be quantified under reduction potential.

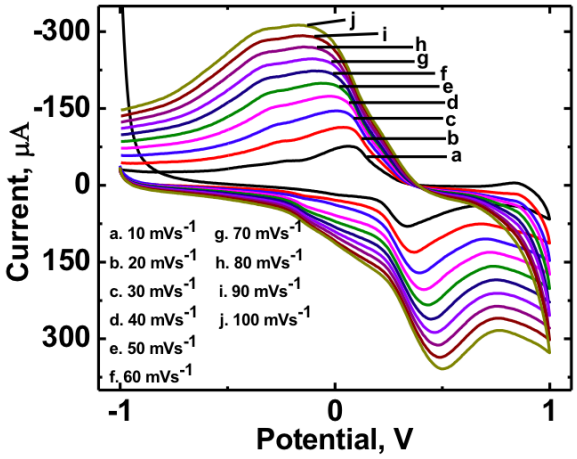

Figure 6.7: CV of 1 mM DA at pH 7.0 on Nafion/PB/ZnO/COOH-MWNTs/GCE at various scan rates; (a) 10, (b) 20, (c) 30, (d) 40, (e) 50, (f) 60, (g) 70, (h) 80, (i) 90, (j) 100, (k) 110 $mV \cdot s^{-1}$

Reproduced with permission from ref. [210]. Copyright 2021, Taylor & Francis

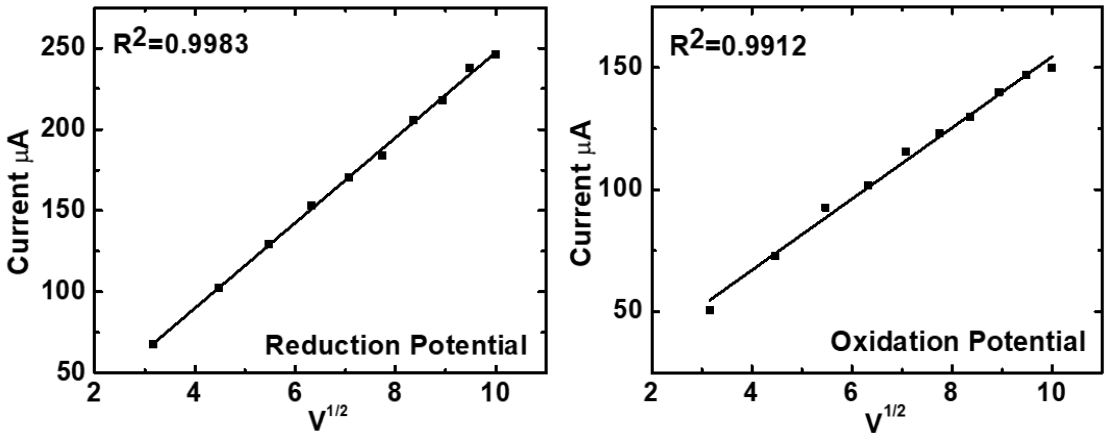

Figure 6.8: Plot of I_{pc} Vs $V^{1/2}$ at reduction and oxidation potentials
Reproduced with permission from ref. [210]. Copyright 2021, Taylor & Francis.

Figure 6.9 shows the chronoamperometric responses of the Nafion/PB/ZnO/COOH-MWNTs/GCE at +0.438 V (DA's determined oxidation potential) versus Ag/AgCl upon sequential additions of 0.3 mM DA, UA, AA, H_2O_2, LA, FA, Glu, APAP, and DA. These analytes were added at various time points, denoted by the arrows in Figure 6.9. Nafion/PB/ZnO/COOH-MWNTs could selectively detect DA in the presence of all of these potentially interfering analytes. No detectable current response is observed, showing that PB/ZnO/COOH-MWNTs sensor is selective to only DA.

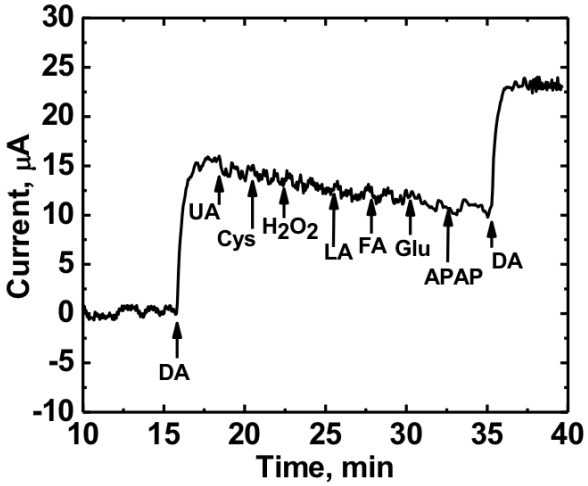

Figure 6.9: CA response of Nafion/PB/ZnO/COOH-MWNTs at +0.438 V vs Ag/AgCl to the sequential addition of 0.3 mM DA, UA, AA, H_2O_2, LA, FA, Glu, APAP, and DA in pH = 7.0 PBS
Reproduced with permission from ref. [210]. Copyright 2021, Taylor & Francis

6.4 Conclusion

The PB/ZnO/COOH-MWNTs composite showed high catalytic activity for the oxidation of DA from 10 to 900 µM at 0.438 V using CA. Large agglomerated ZnO particles, 574nm in diameter, decorated the electrode as a result of PB-induced agglomeration accompanying the optimized performance. The conditions for optimum performance for this sensor were at pH 7.0. Good selectivity and sensitivity of DA in the presence of interfering analytes are useful for neuroblastoma screening between 10 and 100 µM range. At higher DA concentrations (>100 µM), relevant for process controls involving DA cyclization to form PDA, the optimum pH for PDA formation is at 8.5 [189]. Nevertheless, the sensor still functions at [(50 µM/ 200 µM) x 100 1⁄4] 25% current measurement capacity (Figure 5B) compared to at pH 7.0.

CHAPTER 7

Electrochemical Detection of Homovanillic Acid Using PB/ZnO/COOH-MWNTs

Abstract

After tethering refluxed ZnO to carboxylic acid functionalized multiwalled carbon nanotubes (COOH-MWNTs), an electrochemical sensing composite was produced by electrostatically attaching Prussian Blue to ZnO/COOH-MWNTs to enhance sensitivity towards homovanillic acid (HVA). The current response versus various concentrations of HVA was monitored using cyclic voltammetry (CV) and chronoamperometry (CA). Optimization of the sensor was obtained via adjustment of stirring time, pH and deposition loading of the composite onto the glassy carbon electrode (GCE) surface. The sensitivity of HVA was studied in the dynamic range of 5 µM to 1000 µM under CV and 10 µM to 2.3 mM with the LOD of (0.5789±0.1978) µM under CA at pH 7, applicable for neuroblastoma screening and inhibition of aldehyde reductase.

7.1 Introduction

Homovanillic acid (HVA, 4-hdroxy-3-methoxyphenyl acetic acid), catecholamine metabolite is generally excreted in urine. Normal physiological urinary concentrations of HVA present in the range from 8.2 to 42 µmol.L^{-1}. The higher secretion of HVA is associated with presence of neuroblastoma and pheochromocytoma tumors [196, 197]. A pediatric neuroblastic tumor arising in the sympathetic nervous system from neural-crest cells indicates the neuroblastoma (NB). It is considered as the very common solid cancer of young children. The report shows that one child in 10,000 develops NB prior to the age of 15. Mainly 50% of cases are observed before the age of 2 years [198]. A rapid treatment at the first sign of NB and diagnosis for affected people with stage I is the best option compared to that of patients with stages (II), (III) or (IV). Survival rate with 90% is observed with patients of stage (I) or (II) [184]. Therefore, an

early treatment is necessary to inhibit malignancy and mortality in metastatic or repeated phase of the disease. Except tumors, an unusual excretion level of HVA shows other diseases, such as parkinson's diseases [199], suicide attempts [200], schizophrenia [201], depression [202].

The quantification of HVA biomarker in urine samples can be carried out with selective and sensitive process. HPLC with amperometric [203], most sensitive MS detection [204] have been used for determinantion of HVA. In addition, GC-MS [205], immunoassays [206], capillary electrophoresis [207] have been explained. Although these are common methods for the quantification of HVA in urine in clinical laboratories, they generally require expensive instrumentation, time-consuming process and complex sample pre-treatment. Therefore, electrochemical methods offer a simple, cost effective and rapid way of quantification without using expensive instrumentation [184]. The normal urine pH observed to be slightly acidic or basic in the range from pH =4.5 to 8.5 [208]. Khamlichi et al. [184] developed an L-leucine modified sol-gel carbon electrode for HVA quantification in the 0.4-to-100 µM concentration range in urine.

At concentrations at 1 µM and higher, monitoring HVA concentrations is important for applications for inhibiting aldehyde reductase. At concentrations 100 µM – 1 mM, HVA is known to result in uncompetitive inhibition of aldehyde reductase. There are some researchers to have interest on aldehyde reductase. The crucial part of aldehyde reductase from brain tissue is possibly for the metabolism of aldehydes obtained by deamination of the neurotransmitter biogenic amines [209]. We have designed the sensor by using solely non-perishable materials for the electrocatalyst surface to monitor HVA, producing it more amenable for industrial scale-up.

In this study, after successfully tethering Prussian blue (PB) on the surface of ZnO/COOH-MWNTs, we explore, for the first time, the utility of a PB/ZnO/COOH-MWNT composite for assaying HVA using cyclic voltammetry and chronoamperomertry.

7.2 Results and Discussion

In the CV of the 1 mM HVA solution in PBS, the 5-µL composite of PB/ZnO/COOH-MWNTs showed the optimum sensitivity with selectivity for HVA due to the proper loading of the composite as shown in Figure 7.1.

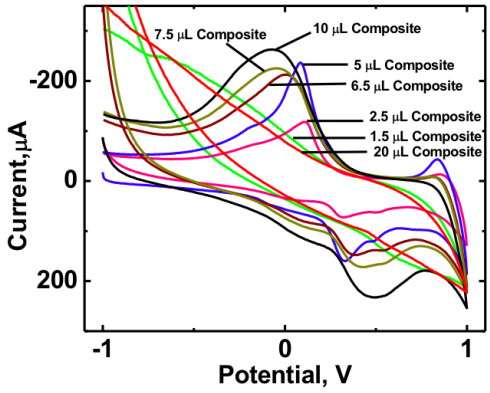

Figure 7.1: Effect of various loading of the composite,
PB/ZnO/COOH-MWNTs with HVA under CV at pH 7.0 with 50 $mV \cdot s^{-1}$

The electrochemical response of Nafion^{TM}/PB/ZnO/COOH-MWNTs/GCE surface with HVA was studied as control experiments. As shown in Figure 7.2, point e, there was no electrochemical behavior to HVA on bare GCE at given potential in PBS (pH 7.0) solution. The cathodic and anodic current peaks were observed at 0.0764 V and 0.3604 V, respectively, which had a pronounced electrochemical response when GCE was modified with PB/ZnO/COOH-MWNTs as shown in Figure 7.2a. Electrochemically controlled experiments were performed using ZnO/COOH-MWNTs and PB in which our composite (PB/ZnO/COOH-MWNTs) shows the

better results as shown in Figure 7.2a. The increase is attributed to the proper attachment of PB, on the surface of ZnO/COOH-MWNTs.

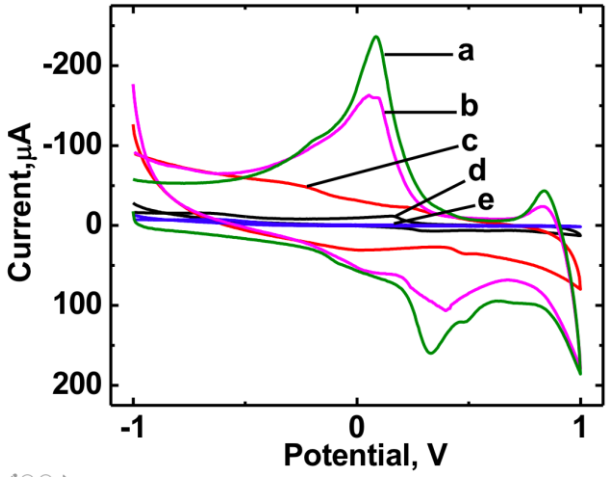

Figure 7.2: Analysis of homovanillic acid under CV at pH 7.0 with 50 $mV \cdot s^{-1}$ scan rate using (a) PB/ZnO/COOH-MWNTs with 1 mM HVA, (b) PB/ZnO/COOH-MWNTs with PBS only, (C) ZnO/COOH-MWNTs with 1 mM HVA, (d) PB with 1 mM HVA, and (e) GCE with 1 mM HVA

Symmetric peak shapes in the CVs at various pH conditions denoted quasi-reversible redox processes. During CV, HVA is oxidized to HVA radical cation and HVA radical cation is reduced back to HVA via an electron process [184]. Figure 7.3 shows the amperometric response of the Nafion^{TM}/PB/ZnO/COOH-MWNTs/GCE as a function of pH in 1 mM HVA at reduction and oxidation potentials of 0.0734 V and +0.3604 V, respectively; the corresponding CVs of 1 mM HVA are shown in Figure 4. The cathodic and anodic currents are maximized at pH 7.0 for both oxidation and reduction potentials. Figure 7.4 shows that our sensor is capable of detecting HVA at various pH conditions. The optimum detection response of HVA was observed from pH 6.0 to 8.0. The highest electrocatalytic activity of our sensor with HVA was observed at pH 7.0 at oxidation potential.

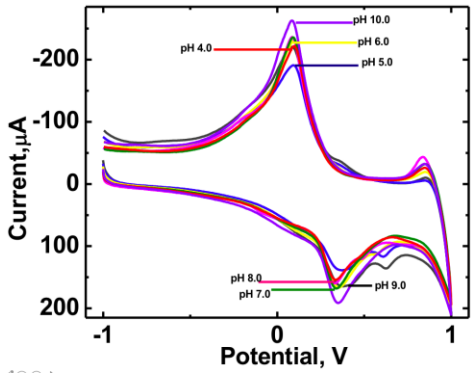

Figure 7.3: Effect of pH in the measurement of 1 mM H_2O_2 at 50 $mV \cdot s^{-1}$ using PB/ZnO/COOH MWNTs

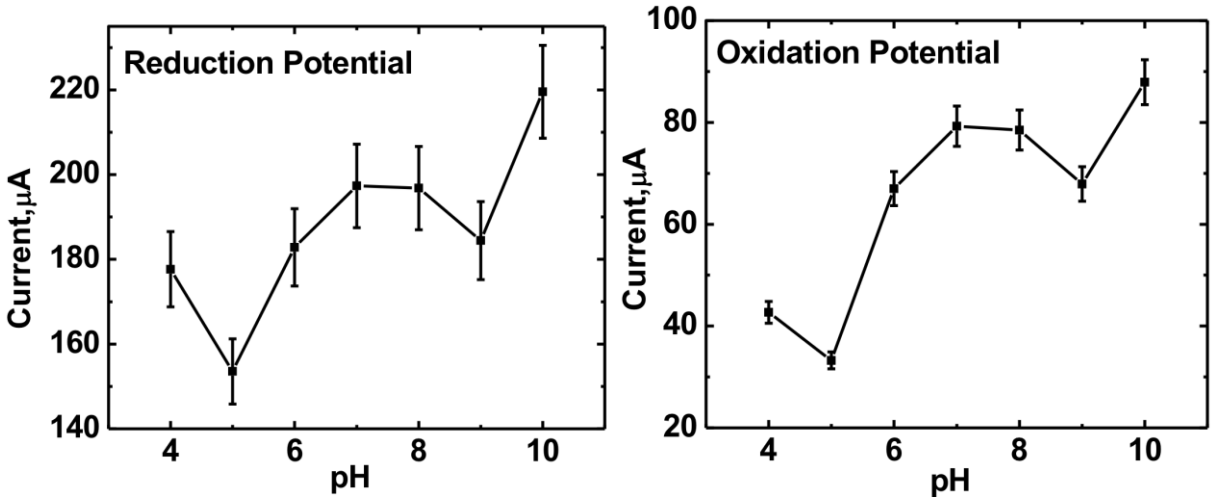

Figure 7.4: A plot of pH vs current to show optimum pH response for highest electrocatalytic activity at pH 7.0 using CVs at reduction and oxidation potential of 0.0734 V and +0.3604 V, respectively

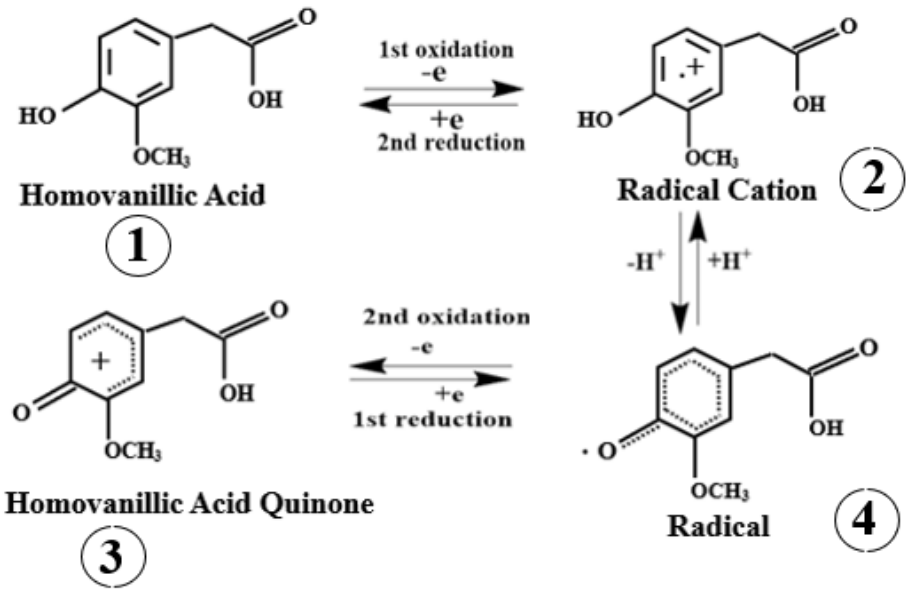

Scheme 7.1: Forms of HVA and HVA cation radical, radical and HVA quinone

7.2.1 Using CV peak height and CA to quantify HVA

The electrocatalytic behavior of PB/ZnO/COOH-MWNTs due to the effect of concentration was studied for the quantification of HVA under CV at pH 7.0. The CV of HVA shows the oxidation peak at +0.3604 V related with structure 2 as shown in Scheme 7.1 against Ag/AgCl (3.5 M KCl). Figure 7.5 explains how the current response was monitored at various concentrations of HVA. Using various concentrations in the range from 5 µM to 1 mM, the CV current responses for such concentrations were observed to be linear. The plot of peak current in µA versus concentration in µM of HVA shows a linear correlation between them. In this analysis, the range of concentration is explained by the equation of linear regression, I_{pc} (µA) = 0.00989 [HVA] (µM) + 114.4 with the correlation coefficient value (R^2) of 0.9906. Extra peaks at 0.0764 V, 0.8236 V, and 0.5365 V represent structure 1, structure 4, and structure 3, respectively, in the CV as the molecule of HVA undergoes various species as shown in Scheme 7.1. There is a change

in slope in the lower concentration of HVA in the calibration curve under CA analysis. A quadratic relationship of HVA in the range from 5 µM to 100 µM was observed as shown in the inset of calibration curve of HVA in Figure 7.5. This relationship follows the regression equation $I_{(\mu A)} = -(9.5 \times 10^{-5})\ [HVA]^2 + 0.0314\ [HVA] + 113.9$, with $R^2 = 0.9318$. In addition, the error bar is relatively larger. Further investigation is required for the analysis of HVA in its lower concentration range. However, the change in slope is not pronounced in the CA data (*vide infra*).

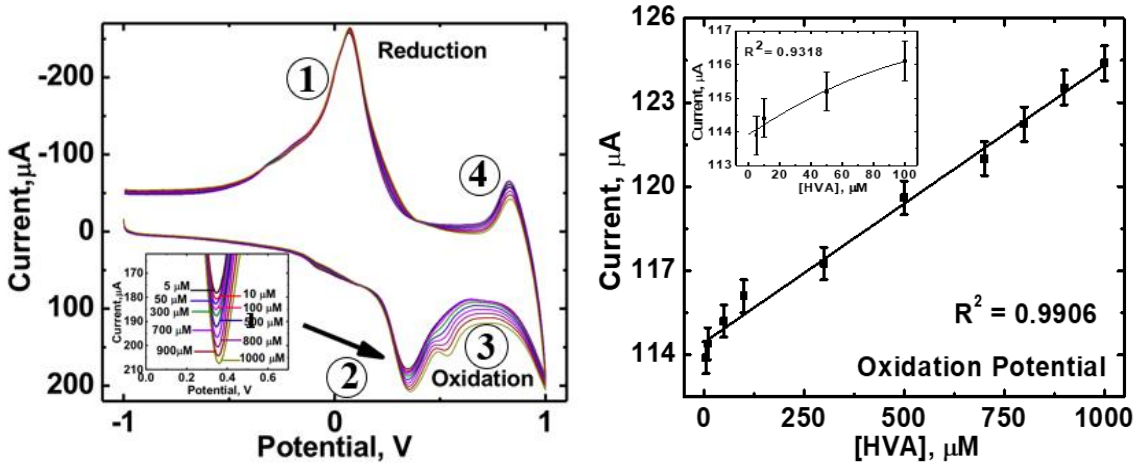

Figure 7.5: CV for the effect of different concentrations of HVA at pH 7.0 with 50 $mV \cdot s^{-1}$ scan rate and its calibration curve

Figure 7.6 shows a typical current-time curve of CA at the Nafion/PB/ZnO/COOH-MWNTs modified electrodes for successive addition of various concentrations of HVA in PBS of pH 7.0 at +0.3604 V. Within 4 sec, the sensor arrived at a steady-state current. It was determined that HVA concentration can be detected as low as 10 µM with the detection limit of (0.5789±0.1978) µM. Figure 7.6 also exhibits a linear relationship between current vs concentration with correlation coefficient, $R^2 = 0.9942$ for HVA concentrations from 10 µM to 2.3 mM. This higher range of concentration of HVA is useful for aldehyde reductase inhibition study as explained above.

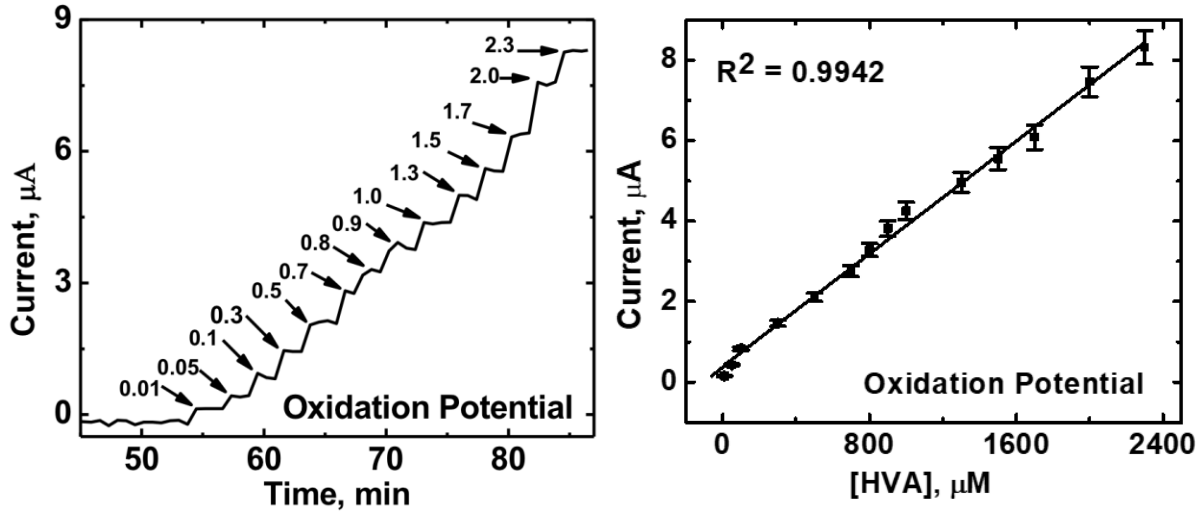

Figure 7.6: CA for the effect of different concentrations of HVA at pH 7.0 at 0.3604 V with 50 $mV{\cdot}s^{-1}$ scan rate and its calibration curve

7.3 Randles-Sevçik Analysis

Cyclic voltammograms of 1 mM HVA at pH 7.0 was shown in Figure 7.7. This CV was observed at different scan of 10, 20, 30, 40, 50, 60, 70, 80, 90, 100 and 110 $mV{\cdot}s^{-1}$ using PB/ZnO/COOH-MWNTs/GCE electrode. The electrocatalytic reduction of HVA due to the effect of the potential by Nafion/PB/ZnO/COOH-MWNTs/GCE was investigated by cyclic voltammetry. The peak potential for the catalytically reduced HVA moves to increasingly negative potential with becoming scan rate larger. However, with the scan rates, the peak current (I_{pc}) of reduction for HVA increased linearly which indicates that the reduction reaction was diffusion controlled. The relationship between the scan rate and I_{pc} was observed to have a good linear connection over the range of 10 – 110 $mV{\cdot}s^{-1}$ as shown in Figure 7.8. A correlation coefficient (R^2) of 0.9999 was obtained for the linear regression equation,

$$I_{pc}\,(\mu A) = 38.35\ V^{1/2}\,(V{\cdot}s^{-1}) - 50.73 \qquad (1)$$

under reduction potential. Similarly, a correlation coefficient (R^2) of 0.9910 was received for the linear regression equation,

I_{pc} (μA) = 12.09 $V^{1/2}$ ($V \cdot s^{-1}$) +9.190……(2)

under oxidation potential. Hence, the reaction of HVA with the electrode surface of Nafion/PB/ZnO/COOH-MWNTs/GCE shows good correlation with the expression of Randles-Sevçik Analysis as the I_{pc} increases linearly as a function of the square root of scan rate. Randles-Sevçik Analysis equation explains the scan rate effect on the peak current in the CV. It is diffusion controlled reaction because reaction that takes place so quickly that the reaction rate is the transport of the reactant through the medium. It is the spontaneous transfer of electroactive species from regions of higher concentration to the regions of lower concentration.

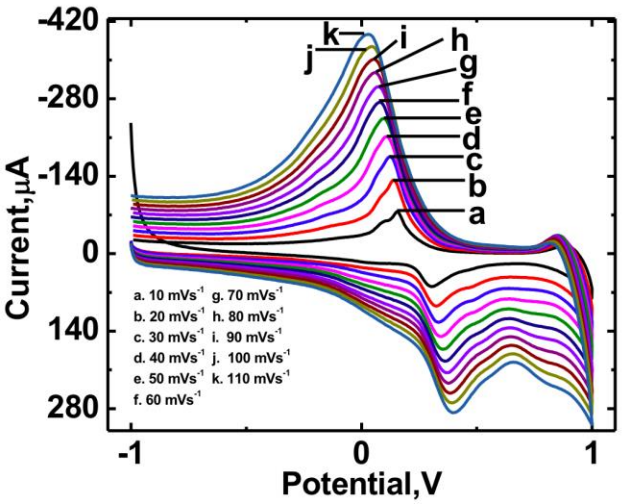

Figure 7.7: CV of 1 mM HVA at pH 7.0 on Nafion/PB/ZnO/COOH-MWNTs/GCE at various scan rates; (a) 10, (b) 20, (c) 30, (d) 40, (e) 50, (f) 60, (g) 70, (h) 80, (i) 90, (j) 100, (k) 110 $mV \cdot s^{-1}$

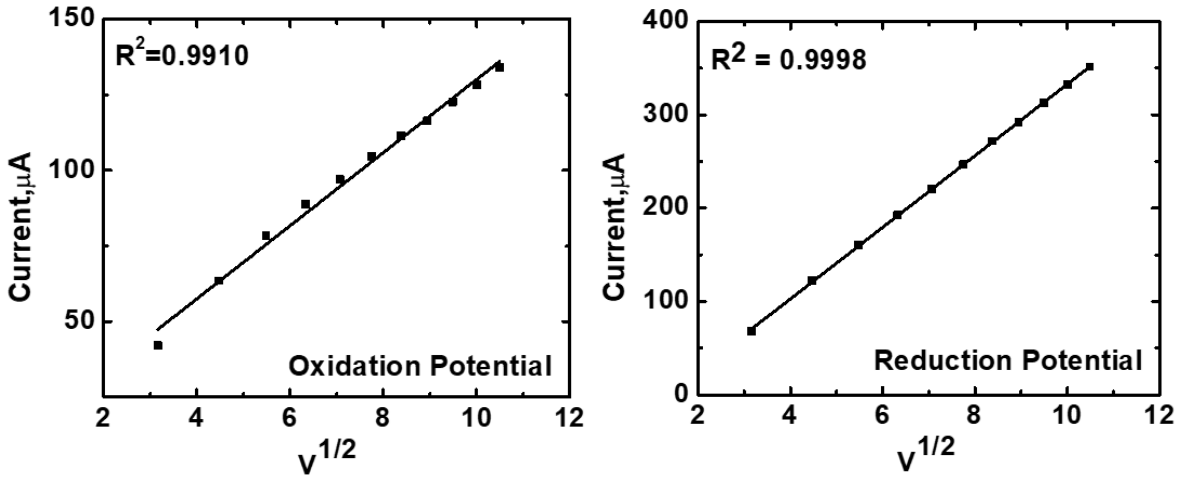

Figure 7.8: Plot of I_{pc} Vs $V^{1/2}$ at reduction and oxidation potentials

Figure 7.9 shows the chronoamperometric responses of the Nafion/PB/ZnO/COOH-MWNTs/GCE at +0.3604 V (HVA's determined oxidation potential) versus Ag/AgCl upon sequential additions of 0.3 mM UA, Cys, H_2O_2, LA, FA, Glu, AA, APAP. These analytes were added at various time points, denoted by the arrows in Figure 8. Nafion/PB/ZnO/COOH-MWNTs could selectively detect HVA in the presence of all of these potentially interfering analytes. No detectable current response is observed, showing that PB/ZnO/COOH-MWNTs sensor is selective to only HVA.

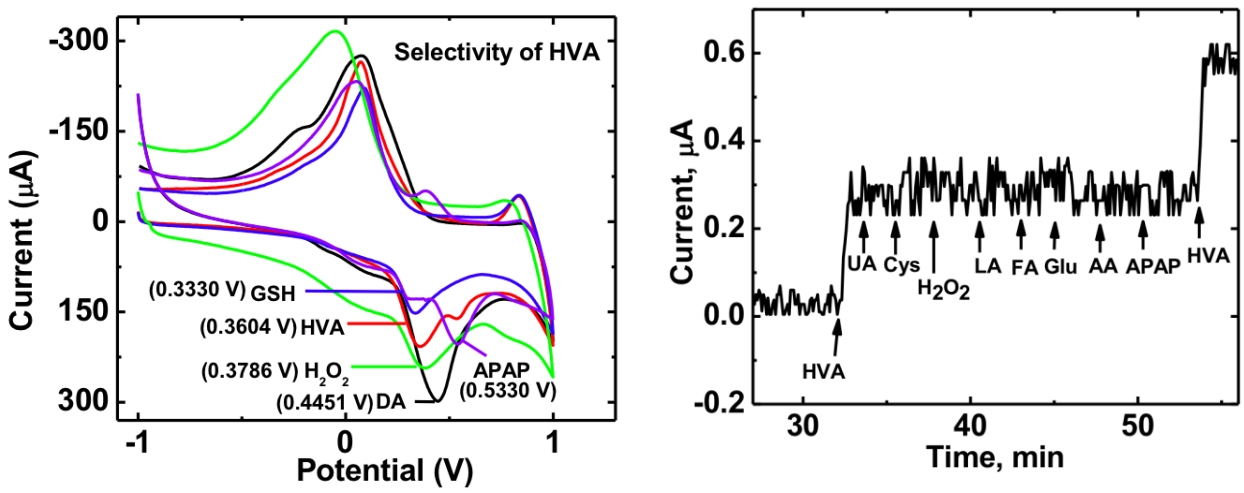

Figure 7.9: CV and CA selectivity study of HVA at 0.3604 V with pH 7.0

7.4 Conclusions

PB/ZnO/COOH-MWNTs composite demonstrated high catalytic activity toward the oxidation of HVA in the 5 µM to 1 mM range under CV and 10 µM to 2.3 mM under CA. The potential application of the sensor for selective determination of HVA was studied in the presence of H_2O_2, glutathione, dopamine, and acetaminophen. The good selectivity and sensitivity of HVA in presence of interfering analytes at pH 7.0 is relevant for urinalysis to screen for neuroblastoma. The higher concentration of HVA is presented for the application in aldehyde reductase inhibitors.

A cost-effective H_2O_2-sensor has been established to monitor H_2O_2 sensitively and selectively. Zinc oxide nanoparticles, carbon nanotubes and Prussian Blue are earth rich materials which are characterized and used for the design of the electrochemical sensing composites. ZnO nanoparticles were synthesized using reflux process at the initial part of the project. Such pure synthesized ZnO nanoparticles were characterized by TEM and EDX. PB/ZnO/COOH-MWNTs was fabricated with the help of ultrasonication and PZC concept. This fabrication route shows an excellent strategy for designing electrochemical sensors. The cytotoxicity study of

PB/ZnO/COOH-MWNTs was done via Alamar Blue Assay shows its biocompatibility. PB/ZnO/COOH-MWNTs is able to accurately monitor H_2O_2 in cancer cell lines compared to the conventional ELISA technique.

A CV method was used to analyze the efficiency of designed electrochemical sensors. This sensor exhibits higher current signal at low overpotential (-0.004 V vs Ag/AgCl) to determine H_2O_2 when PB was successfully attached on the surface of ZnO/COOH-MWNTs.

A CA method was used to analyze the sensitivity and selectivity of the developed sensor. This sensor showed a detection limit of 0.019 µM of H_2O_2. The selectivity of the sensor was examined in the presence of interfering analytes such as UA, AA, APAP, FA and Glu. The designed sensor is able to detect H_2O_2 only at reduction potential (-0.004 V). This is the potential application of the sensor for selective detection of H_2O_2 in physiological conditions. Under the designed CA detection method, Standard addition method was combined to further monitor H_2O_2 in the ex-situ condition of BT20 and 4T1 cancer cell lines. Overall, the sensor using PB/ZnO/COOH-MWNTs composite modified GCE under CA provides a rapid, facile, sensitive and selective electrochemical sensor to detect H_2O_2. This sensor was observed to be able to determine H_2O_2 as low as 1 µM quantitatively.

The relationship between apoptosis and oxidative stress of BT20 cells is established to understand the mechanism of the death of cancer cells. This sensor appears as the versatile sensor since it is also capable to study glutathione, dopamine, and homovanillic acid.

References

1. Radushkevich, L. V.; Lukyanovich, V. M. The structure of carbon forming in thermal decomposition of carbon monoxide on an Iron catalyst. *Russian J. Phys. chem.* **1952**, 25, 88-95.
2. Iijima, S. Helical microtubules of graphitic carbon. *Nature* **1991**, 354, 56-58.
3. Kroto, H. W.; Heath, J. R.; O'Brien, S. C.; Curl, R. F.; Smalley, R. E. C_{60}: Buckministerfullerene. *Nature* **1985**, 318, 162-163.
4. Cushing, B. L.; Kolesnichenko, V. L.; O'Connor, C. J. Recent advances in the liquid-phase syntheses of inorganic nanoparticles. *Chem. Rev*. **2004**, 104, 3893-3946.
5. Wang, J. Carbon nanotube based electrochemical biosensors: A review. *Electroanalysis* **2005**, 17, 7-14.
6. Gong, K.; Yan, Y.; Zhang, M.; Su, L.; Xiong, S.; Mao, L. Electrochemistry and electroanalytical applications of carbon nanotubes: A review. *Anal. Sci.* **2005**, 21, 1383-1393.
7. Ahammad, A. J. S.; Lee, J-J.; Rahman, Md. A. Electrochemical sensors based on carbon nanotubes. *Sensors* **2009**, 9, 2289-2319.
8. Rivas, G. A.; Rubianes, M. D.; Rodriguez, M. C.; Ferreyra, N. F.; Luque, G. L.; Pedano, M. L.; Miscoria, S. A.; Parrado, C. Carbon nanotubes for electrochemical biosensing, *Talanta* **2007**, 74, 291-307.
9. Vashist, S. K.; Zheng, D.; Al-Rubeaan, K.; Luong, J. H.T.; Sheu, F-S. Advances in carbon nanotube based electrochemical sensors for bioanalytical applications. *Biotechnol. Adv.* **2011,** 29,169-188.
10. Hu, C.; Hu, S. Carbon nanotube-based electrochemical sensors: principles and applications in biomedical systems. *J. Sensors* **2009**, 2009,1-40.
11. Yanez-Sedeno, P.; Riu, J.; Pingarron, J. M.; Rius, F. X. Electrochemical sensing based on carbon nanotubes. *Trends in Anal. Chem.* **2010**, 9, 939-953.
12. Kimmel, D. W.; LeBlanc, G.; Meschievitz, M. E.; Cliffel, D. E. Electrochemical sensors and biosensors. *Anal. Chem.* **2012**, 84, 685-707.
13. Kurowsa E.; Brozozka, A.; Jarosz, M.; Sulka, G. D.; Jaskula, M. Silver nanowire array sensor for sensitive and rapid detection of H_2O_2. *Electrochim. Acta* **2013**, 104, 439-447.
14. Campanella L.; Roversi R.; Sammartino, M. p.; Tomassetti, M. Hydrogen peroxide determination in pharmaceutical formulations and cosmetics using a new catalase biosensor. *J. Pharm. Biomed. Anal.* **1998**, 18, 105-116.
15. Lu, C. P.; Lin, C. T.; Chang, C. M.; Wu, S. H.; Lo, L. C. Nitrophenylboronic acid as highly chemoselective probe to detect hydrogen peroxide in foods and agricultural products. *J. Agric. Food Chem.* **2011**, 59, 11403-11406.
16. Recio, E.; Alvarez-Rodriguez, M. L.; Rumbero, A.; Garzon, E.; Coque, J. J. Destruction of chloroanisoles by using a hydrogen peroxide activated method and its application to remove chloroanisoles from cork stoppers. *J. Agric. Food Chem.* **2011**, 59, 12589-12597.
17. Usui, Y.; Sato, K.; Tanaka, M.; Catalytic dihydroxylation of olefins with hydrogen peroxide: An organic-solvent- and metal-free system. *Angew. Chem. Int. Ed.* **2003**, 42, 5623-5625.
18. Huang, X.; Atwood, C. S.; Hartshorn, M. A.; Multhaup, G.; Goldstein, L. E.; Scarpa, R. C.; Cuajungco, M. P.; Gray, D. N.; Lim, J.; Morr, R.D.; Tanzi, R. E.; Bush, A. L.; The Aβ peptide of Alzeimer's disease directly produces hydrogen peroxide through metal ion reduction. *Biochem.* **1999**, 38, 7609-7616.

19. Veal, E. A.; Day, A. M.; Morgan, B. A. Hydrogen peroxide sensing and signaling. *Mol. Cell* **2007**, 26, 1-14.
20. Rojas, M. R.; Leung, C.; Whitley, D.; Zhu, Y.; Arnold, R. G.; Saez, A. E. Advanced oxidation of trace organics in water by hydrogen peroxide solar photolysis. *Ind. Eng. Chem. Res.* **2011**, 50, 12479-12487.
21. Lopez-Lazaro, M. Dual role of hydrogen peroxide in cancer: possible relevance to cancer chemoprevention and therapy. *Cancer Lett.* **2007**, 252, 1-8.
22. Giorgio, M.; Trinei, M.; Migliaccio, E.; Pelicci, P. G. Hydrogen peroxide: A metabolic by-product or a common mediator of ageing signals? *Nat. Rev. Mol. Cell Biol.* **2007**, 8, 722-728.
23. Thome-Duret V.; Reach, G.; Gangnerau, M. N.; Lemonnier, F.; Klein, J. C.; Zhang, Y.; Wilson, G. S. Use of a subcutaneous glucose sensor to detect decreases in glucose concentration prior to observation in blood. *Anal. Chem.* **1996**, 66, 3822-3826.
24. Chen, K. J.; Chandrasekara Pillai, K.; Rick, J.; Pan, C. J.; Wang, S. H.; Liu, C. C.; Hwang, B. J. Bimetallic PtM (M=Pd, Ir) nanoparticle decorated multi-walled carbon nanotube enzyme-free, mediator-less amperometric sensor for H_2O_2. *Biosens. Bioelectron.* **2012**, 33, 120-127.
25. Ikarashi, Y.; Tsuchiya, T.; Nakamura, A. Cytotoxicity of medical materials sterilized with vapor-phase hydrogen peroxide. *Biomater.* **1995**, 16, 177-183.
26. Reddy, M. A.; Kishore, M. S.; Pralong, V.; Caignaert, V.; Varadaraju, U. V.; Raveau, B. Electrochemical performance of VoMoO4 as negative electrode material for Li ion batteries. *J. Power Sources* **2007**, 168, 509-512.
27. Raman, R. K.; Shukla, A. K. A direct borohydride/hydrogen peroxide fuel cell with reduced alkali crossover. *Fuel Cells* **2007**, 7, 225-231.
28. Shafei, M.; Honeychurch, K. C. Voltammetric behavior of hydrogen peroxide at a silver electrode fabricated from a rewritable digital versatile disc (DVD) and its determination in water samples. *Anal. Methods* **2013**, 5, 6631-6636.
29. Pandey, R. R.; Guo, Y.; Gao, Y.; Chusuei, C. C. A Prussian Blue ZnO carbon nanotube composite for chronoamperometrically assaying H_2O_2 in BT20 and 4T1 breast cancer cells. *Anal. Chem.* **2019**, 91, 10573-10581.
30. Kurowska, E.; Brzózka, A.; Jarosz, M.; Sulka, G. D.; Jaskuła, M. Silver nanowire array sensor for sensitive and rapid detection of H_2O_2. *Electrochim. Acta* **2013,** 104, 439-447.
31. Ahmad, M.; Pan, C.; Gan, L.; Nawaz, Z.; Zhu, J. Highly Sensitive Amperometric Cholesterol Biosensor Based on Pt-Incorporated Fullerene-like ZnO Nanospheres. *J. Phys. Chem. Part C* **2010,** 114, 243-250.
32. Wayu, M. B.; Spidle, R. T.; Devkota, T.; Deb, A. K.; Delong, R. K.; Ghosh, K. C.; Wanekaya, A. K.; Chusuei, C. C. Morphology of hydrothermally synthesized ZnO nanoparticles tethered to carbon nanotubes affects electrocatalytic activity for H_2O_2 detection. *Electrochim. Acta* **2013,** 97, 99-104.
33. Lipinski, B. Hydroxyl radical and its scavengers in health and disease. *Oxid. Med. Cell. Longev.* **2011,** 2011, 809696-809696.
34. Zhang, D. X.; Borbouse, L.; Gebremedhin, D.; Mendoza, S. A.; Zinkevich, N. S.; Li, R.; Gutterman, D. D. H_2O_2-Induced Dilation in Human Coronary Arterioles: Role of Protein Kinase G Dimerization and Large-Conductance Ca^{2+}-Activated K^+ Channel Activation. *Circ. Res.* **2012,** 110, 471-480.

35. Matoba, T.; Shimokawa, H.; Nakashima, M.; Hirakawa, Y.; Mukai, Y.; Hirano, K.; Kanaide, H.; Takeshita, A. Hydrogen peroxide is an endothelium-derived hyperpolarizing factor in mice. *J. Clin. Invest.* **2000,** 106, 1521-1530.
36. Luo, Y.; Liu, H.; Rui, Q.; Tian, Y. Detection of extracellular H_2O_2 released from human liver cancer cells based on TiO_2 nanoneedles with enhanced electron transfer of cytochrome c. *Anal. Chem.* **2009,** 81, 3035-3041.
37. Byon, C. H.; Heath, J. M.; Chen, Y. Review article: Redox signaling in cardiovascular pathophysiology: A focus on hydrogen peroxide and vascular smooth muscle cells. *Red. Biol.* **2016,** 9, 244-253.
38. Wu, P.; Cai, Z.; Chen, J.; Zhang, H.; Cai, C. Electrochemical measurement of the flux of hydrogen peroxide releasing from RAW 264.7 macrophage cells based on enzyme-attapulgite clay nanohybrids. *Biosens. Bioelectron.* **2011,** 10, 4012-4017.
39. Lippert, A. R.; Van de Bittner, G. C.; Chang, C. J. Boronate oxidation as a bioorthogonal reaction approach for studying the chemistry of hydrogen peroxide in living systems. *Acc. Chem. Res.* **2011,** 44, 793-804.
40. Szatrowski, T. P.; Nathan, C. F. Production of large amounts of hydrogen peroxide by human tumor cells. *Cancer Res.* **1991,** 51, 794-798.
41. Matos, R. C.; Coelho, E. O.; Souza, C. F.; Guedes, F. A.; Matos, M. A. Peroxidase immobilized on Amberlite IRA-743 resin for on-line spectrophotometric detection of hydrogen peroxide in rainwater. *Talanta* **2006,** 69, 1208-1214.
42. Sellers, R. M. Spectrophotometric determination of hydrogen peroxide using potassium titanium(IV) oxalate. *Analyst* **1980,** 105, 950.
43. Carter, W. O.; Narayanan, P. K.; Robinson, J. P. Intracellular hydrogen peroxide and superoxide anion detection in endothelial cells. *J. Leukoc. Biol.* **1994**, 55, 253-258.
44. Tarpey, M. M.; Fridovich, I. Methods of detection of vascular reactive species: nitric oxide, superoxide, hydrogen peroxide, and peroxynitrite. *Circ. Res.* **2001,** 89, 224-236.
45. Tahirović, A.; Copra, A.; Omanović-Miklicanin, E.; Kalcher, K. A chemiluminescence sensor for the determination of hydrogen peroxide. *Talanta* **2007,** 72, 1378-1385.
46. Klassen, N. V.; Marchington, D.; McGowan, H. C. E. H_2O_2 determination by the I^3(superscript -) method and by $KMnO_4$ titration. *Anal. Chem.* **1994,** 18, 2921-2925.
47. Han, L.; Wang, Q.; Tricard, S.; Liu, J.; Fang, J.; Zhao, J.; Shen, W., Amperometric detection of hydrogen peroxide utilizing synergistic action of cobalt hexacyanoferrate and carbon nanotubes chemically modified with platinum nanoparticles. *RSC Adv.* **2013,** *3*, 281-287.
48. Liu, A.; Dong, W.; Liu, E.; Tang, W.; Zhu, J.; Han, J. Non-enzymatic hydrogen peroxide detection using gold nanoclusters-modified phosphorus incorporated tetrahedral amorphous carbon electrodes. *Electrochim. Acta* **2010,** 55, 1971-1977.
49. Hafei, M.; Honeychurch, K. Voltammetric behaviour of hydrogen peroxide at a silver electrode fabricated from a rewritable digital versatile disc (DVD) and its determination in water samples. *Anal. Methods* **2013,** 5, 6631-6636.
50. Cowlard, F.; Lewis, J. Vitreous carbon- a new form of carbon. *J. Mater. Sci.* **1967**, 2, 507-512.
51. Pandolfo, A.; Hollenkamp, A. Carbon properties and their role in capacitors. *J. Power Sources* **2006**, 157, 11-27.
52. Sawyer, D. T.; Sobkowiak, A.; Roberts, J. L. Electrochemistry for chemists: Wiley 1995.

53. Geng, Y.; Fu, C.; Zhousheng, Y., Electrocatalytic Oxidation of Hydrogen Peroxide Based on the Shuttlelike Nano-CuO-Modified Electrode. *Inter. J. Electrochem.* **2012**, 2012, 1-6.
54. Lin, K. C.; Tsai, T. H.; Chen, S. M. Performing enzyme-free H_2O_2 biosensor and simultaneous determination for AA, DA, and UA by MWCNT-PEDOT film. *Biosens. Bioelectron.* **2010,** 26, 608-614.
55. Wu, C.; Qiao, X.; Chen, J.; Wang, H.; Tan, F.; Li, S. A novel chemical route to prepare ZnO nanoparticles. *Mater. Lett.* **2006,** 60, 1828-1832.
56. Bai, H. P.; Lu, X. X.; Yang, G. M.; Yang, Y. H. Hydrogen peroxide biosensor based on electrodeposition of zinc oxide nanoflowers onto carbon nanotubes film electrode. *Chinese Chem. Lett.* **2008,** 19, 314-318.
57. Li, J.; Qiu, J. D.; Xu, J. J.; Chen, H. Y.; Xia, X. H. The Synergistic Effect of Prussian-Blue-Grafted Carbon Nanotube/Poly(4-vinylpyridine) Composites for Amperometric Sensing. *Adv. Func. Mater.* **2007**, 17, 1574-1580.
58. Yanli, Y.; Xiaoyun, B.; Kwok-Keung, S. Spontaneous Deposition of Prussian Blue on Multi-Walled Carbon Nanotubes and the Application in an Amperometric Biosensor. *Nanomaterials* **2012,** 2, 428-444.
59. Ricci, F.; Palleschi, G. Sensor and biosensor preparation, optimisation and applications of Prussian Blue modified electrodes. *Bions. Bioelectron.* **2005**, 21, 389-407.
60. Musameh, M.; Wang, J.; Merkoci, A.; Lin, Y. Low-potential stable NADH detection at carbon-nanotube-modified glassy carbon electrodes. *Electrochem. Commun.* **2002**, 4, 743-746.
61. Wang, J.; Li, M.; Shi, Z.; Li, N.; Gu, Z. Direct electrochemistry of cytochrome c at a glassy carbon electrode modified with single-wall carbon nanotubes. *Anal. Chem.* **2002**, 74, 1993-1997.
62. Lu, S. Y.; Chen, Y.; Fang, X.; Feng, X. Hydrogen peroxide sensor based on electrodeposited Prussian blue film. *J. Appl. Electrochem.* **2017,** 47, 1261-1271.
63. Dresselhaus, M. S.; Dresselhaus, G.; Saito, R. Physics of carbon nanotubes. *Carbon,* **1995**, 7, 883-891.
64. Dresselhaus, M. S.; Dresselhaus, G.; Charlier, J. C.; Hernandez, E. Electronic, thermal and mechanical properties of carbon nanotubes. *Phil. Trans. R. Soc. Lond.* A, **2004,** *362*, 2065-2098.
65. Bandaru, P. R. Electrical properties and applications of carbon nanotube structures. *J. Nanosci. Nanotechnol.* **2007**, 7, 1-29.
66. Ajayan, P. M.; Zhou, Otto J. Applications of carbon nanotubes. *Top. Appl. Phys.* **2001**, 80, 391-425.
67. Awasthi, K.; Srivastava, A.; Srivastava, O. N. Synthesis of carbon nanotubes. *J. Nanosci. Nanotechnol.* **2005**, 5, 1616-1636.
68. Harris, Peter J. F. *Carbon Nanotube Science: Synthesis, properties and applications*; Cambridge University Press: New York, 2009.
69. Nikolaos, K.; Nikos, T. Current progress on the chemical modification of carbon nanotubes. *Chem. Rev*. **2010**, 110, 5366-5397.
70. Banerjee, S.; Hemraj-Benny, T.; Wong, S. S. Covalent surface chemistry of single walled carbon nanotubes. *Adv. Mater.* **2005**, 17, 17-29.
71. Singh, P.; Campidelli, S.; Giordani, S.; Bonifazi, D.; Bianco, A.; Prato, M. Organic functionalization and characterization of single-walled carbon nanotubes. *Chem. Soc. Rev.* **2009,** 38, 2214-2230.

72. Salimi, A.; Mahdioun, M.; Noorbakhsh, A.; Abdolmaleki, A.; Ghavami, R. A novel non-enzymatic hydrogen peroxide sensor based on single walled carbon nanotubes-manganese complex modified glassy carbon electrode. *Electrochim. Acta* **2011**, 56, 3387-3394.
73. Chu, H.; Wei, L.; Cui, R.; Wang, J.; Li, Y. Carbon nanotubes combined with inorganic nanomaterials: Preparations and applications. *Coord. Chem. Rev.* **2010**, 254, 1117-1134.
74. Hersch, P. Estimation of traces of oxygen in gases. Patent GB 707323, April 14, 1954.
75. Skoog, D. A.; Holler, F. J.; Crouch, S. R. Voltammetry. Principles of instrumental analysis, 6th edition, David Harris, CA, 2007, 716-760.
76. Kissinger, P. T. and Heineman, W. R. Laboratory techniques in electroanalyticalchemistry, New York, Marcel Dekker, 1984, p. 6.
77. Kissenger, P.T.; Heineman W.R. Cyclic Voltametry. *J. Chem. Educ.* **1993**, 60, 702-706.
78. Evans, D.H.; O'connell, K.M.; Petersen, R.A.; Michael, J.K. Cyclic voltammetry. *J. Chem. Educ.* **1983**, 60, 290-293.
79. Bard, A. J.; Faulker, L. R. Electrochemical methods: fundamentals and applications: Wiley New York, 1980.
80. Wang, J. Nanomaterial-based amplified transduction of biomolecular interactions. *Small* **2005**, 1, 1036-1043.
81. Luo, X.; Morrin, A.; Killard, A. J.; Smyth, M. R. Application of nanoparticles in electrochemical sensors and biosensors. *Electroanaysis* **2006**, 18, 319-326.
82. Lin, C. C.; Chu, B. T.; Tobias, G.; Sahakalkan, S.; Roth, S.; Green, M. L.; Chen, S. Y. Electron transport behavior of individual zinc oxide coated single-walled carbon nanotubes. *Nanotechnol.* **2009**, 20, 105703.
83. Green, J. M.; Dong, L. F.; Gutu, T.; Jiao, J.; Conley, J. F.; Ono, Y. ZnO-nanoparticle-coated carbon nanotubes demonstrating enhanced electron field-emission properties. *J. Appl. Phys.* **2006**, 99, 094308.
84. Vijayalakshmi, K.; Jereli, S. D.; Alagusundaram, K. Electron beam and spray technologies fabrication of hybrid MnO_2/CNTs/Ta nanocomposite for the electrochemical detection of H_2O_2. *Ceram. Int.* **2017**, 43, 14464-14472.
85. Ping, J.; Wu, J.; Fan, K.; Ying, Y. An amperometric sensor based on Prussian blue and poly-(o-phenylenediamine) modified glassy carbon electrode for the determination of H_2O_2 in beverages. *Food Chemistry* **2011**, 126, 2005-2009.
86. Ma, W.; Tian, D. Direct electron transfer and electrocatalysis of hemoglobin in ZnO coated multiwalled carbon nanotubes and nafion composite matrix. *Bioelectrochem.* **2010**, 78, 106-112.
87. Wahab, R.; Ansari, S. G.; Seo, H. K.; Kim, Y. S.; Suh, E. K.; Shin, H. S. Low temperature synthesis and characterization of rosette-like nanostructures of ZnO using solution process. *Solid State Sci.* **2009**, 11, 439-43.
88. Kubota, J.; Haga, K.; Kashiwaba, Y.; Watanabe, H.; Zhang, B. P.; Segawa, Y. Characteristics of ZnO whiskers prepared from organic-zinc. *Appl. Surf. Sci.* **2003**, 216, 431-435.
89. Gusatti, M.; Rosario, J. A.; Barrosa, G. S.; Campos, C. E.; Riella, H. G.; Kuhnen, N. Synthesis of ZnO nanostructures in low reaction temperature. *Chem. Eng. Trans.* **2009**, 17, 1017-1021.

90. Fang, B.; Zhang, C.; Zhang, G. A novel hydrazine electrochemical sensor based on a carbon nanotube-wired ZnO nanoflower-modified electrode. *Electrochim. Acta* **2009**, 55, 178–182.
91. Das, S. C. Electrochemical detection of uric acid using a refluxed zinc oxide carbon nanotube composite. MS thesis, Middle Tennessee State University, Murfreesboro, TN, 2015.
92. Saito, R.; Dresselhaus, G.; Dresselhaus, M. S. Physical Properties of Carbon Nanotubes. Imperial College Press: London: 1998.
93. Brown, G. E.; Henrich, V. E.; Casey, W. H.; Clark, D. L.; Eggleston, C.; Felmy, A.; Goodman, D. W.; Gratzel, M.; Macial, G.; McCarthy M. I.; Nealson, K. H.; Sverjensky, D. A.; Toney, M. F.; Zachara, J. M. Metal oxide surfaces and their interactions with aqueous solutions and microbial organisms. *Chem Rev.* **1999**, 99, 77-174.
94. Park, J.; Regalbuto, J. R. A simple, accurate determination of oxide PZC and the strong buffering effect of oxide surfaces at incipient wetness. *J. Colloid Interface Sci.* **1995**, 175, 239–252.
95. Chusuei, C. C., and D. W. Goodman. 2003. X-ray photoelectron spectroscopy. Encyclopedia of Physical Science and Technology 17:921–38. doi:10.1016/B0-12-227410-5/00830-9
96. Barr, T. L.; Seal, S. Nature of the use of adventitious carbon as a binding energy standard. *J. Vac. Sci. Amp. Technol. A* **1995**, 13, 1239-46.
97. Biesinger, M. C.; Lau, L. W. M.; Gerson, A. R.; Smart, R. S. C. Resolving surface chemical states in XPS analysis of first row transition metals, oxides and hydroxides: Sc, Ti, V, Cu and Zn. *Appl. Surf. Sci.* **2010**, 257, 887-98.
98. Wagner, C. D.; Davis, L. E.; Zeller, M. V.; Taylor, J. A.; Raymond, R. H.; Gale, L. H. Empirical atomic sensitivity factors for quantitative analysis by electron spectroscopy for chemical analysis. *Surf. Interface Anal.* **1981**, 3, 211-225.
99. Haber, J.; Stoch, J.; Ungier, L. X-ray photoelectron spectra of oxygen in oxides of Co, Ni, Fe and Zn. *J. Electron Spectros. Relat. Phenomena* **1976**, 9, 459–467. doi:10. 1016/0368-2048(76)80064-3.
100. Zhu, Y.; Elim, H. I.; Foo, Y. L.; Yu, T.; Liu, Y.; Ji, W.; Lee, J. Y.; Shen, Z.; Wee, A. T.; Thong, J. T. Multiwalled Carbon Nanotubes Beaded with ZnO Nanoparticles for Ultrafast Nonlinear Optical Switching. *Adv. Mater.* **2006**, 18, 587-592.
101. Singh, L. T.; Sugavaneshwar, R. P.; Nanda, K. K. Carbon nanotube-ZnO nanowire hybrid architectures as multifunctional devices. *AIP Adv.* **2013,** *3*, 082106.
102. McCafferty, E.; Wightman, J. P. Determination of the concentration of surface hydroxyl groups on metal oxide films by a quantitative XPS method. *Surf. Interface Anal.* **1998**, 26, 549-564.
103. Beamson, G; Briggs, D. High resolution of organic polymers: the Scienta ESCA 300 database(1992). *J. Chem. Edu.* **1993,** 70, A25.
104. Wagner, C. D.; Riggs, W. M.; Davis, L. E.; Moulder, J. F.; Muilenberg, G. E. Handbook of X-ray photoelectron spectroscopy, Perkin-Elmer corporation, Physical Electronics Division, Eden Prairie, Minn. 55344. **1979**.
105. Ahmad, M.; Ahmed, E.; Hong, Z. L.; Ahmed, W.; Elhissi, A.; Khalid, N. R. Photocatalytic, sonocatalytic and sonophotocatalytic degradation of Rhodamine B using ZnO/CNTs composites photocatalysts. *Ultrason. Sonochem.* **2014,** 21, 761-773.
106. Zahn, R,; Coullerez, G.; J. Voros, J.; Zambelli, T. Effect of polyelectrolyte interdistribution on electron transport in redox-active polyelectrolyte multilayers. *J. Mater. Chem.* **2012**, 22, 11073–11078.

107. Limbach, L. K.; Wick, P.; Manser, P.; Grass, R. N.; Bruinink, A.; Stark, W. J. Exposure of engineered nanoparticles to human lung epithelial cells: Influence of chemical composition and catalytic activity on oxidative stress. *Environ. Sci. Technol.* **2007**, 41, 4158-4163.
108. Fubini, B.; Ghiazza, M.; Fenoglio, I. Physicochemical features of engineered nanoparticles relevant to their toxicity. *Nanotoxicol.* **2010**, 4, 347-363.
109. Hu, X.; Cook, S.; Wang, P.; Hwang, H. M. In vitro evaluation of cytotoxicity of engineered metal oxide nanoparticles. *Sci. Total Environ.* **2009**, 497, 3070-3072.
110. Colvin, V. L. The potential environmental impact of engineered nanomaterials. *Nature Biotechnol*. **2003**, 21, 1166-1170.
111. Kroll, A.; Pillukat, M. H.; Hahn, D.; Schnekenburger, J. Interference of engineered nanoparticles with *in vitro* toxicity assays. *Archiv. Toxicol.* **2012**, 86, 1123-36.
112. Lewinski, N.; Colvin, V.; Drezek, R. Cytotoxicity of nanoparticles. *Small*, **2008**, 4, 26-49.
113. Shang, L.; Nienhaus, K.; Nienhaus, G. U. Engineering nanoparticles interacting with cells: Size matters. *J. Nanobiotechnol.* **2014**, 12, 1-11.
114. Men, S. K.; Cao, X. S.; Wang, Z. Y. Comparative study about cytotoxicity with CuO engineered nanoparticles, TiO2 engineered nanoparticles, CeO2 engineered nanoparticles, single-walled carbon nanotubes. *Adv. Mater. Res.* **2014**, 881, 956-958.
115. Kao, Y. Y.; Chen, Y. C.; Cheng, T. J.; Chiung, Y. M.; Liu, P. S. Zinc Oxide Nanoparticles Interfere With Zinc Ion Homeostasis to Cause Cytotoxicity. *Toxicol. Sci.* **2012**, 125, 462-472.
116. Punnoose, A.; Dodge, K.; Rasmussen, J. W.; Chess, J.; Wingett, D.; Anders, C. Cytotoxicity of ZnO nanoparticles can be tailored by modifying their surface structure: A green Chemistry approach for safer nanomaterials. *ACS Sustain. Chem. Eng.* **2014**, 2, 1666-1673.
117. Chusuei, C. C.; Wu, C. H.; Mallavarapu, S.; Hou, F. Y. S.; Hsu, C. M.; Winiarz, J. G.; Aronstam, R. S.; Huang, Y. W. Cytotoxicity in the age of nano: The role of fourth period transition metal oxide nanoparticle physicochemical properties. *Chem. Biol. Int.* **2013**, 206, 319-326.
118. Hsiao, I. L.; Huang, Y. J. Titanium Oxide Shell Coatings Decrease the Cytotoxicity of ZnO Nanoparticles. *Chem. Res. Toxicol.* **2011**, 24, 303-313.
119. George, S.; Pokhrel, S.; Xia, T.; Gilbert, B.; Ji, Z.; Schowalter, M.; Rosenauer, A.; Damoiseaux, R.; Bradley, K. A.; Madler, L.; Nel. A. E. Use of a rapid cytotoxicity screening approach to engineer a safer zinc oxide nanoparticle through iron doping. *ACS Nano*, **2009**, 4, 15-29.
120. Burgo, R. A.; Patel, S.; Bollard, C. M.; Cruz, C. R. Y.; Fernandes, R. Conjugating Prussian blue nanoparticles onto antigen-specific T-cells as a combined nanoimmunotherapy. *Nanomedicine* **2016**, 11, 1759-1767.
121. Kandanapitiye, M. S.; valley, B.; Yang, L. D.; Fry, A. M.; Woodward, P. M. Gallium analogue of soluble Prussian blue KGa[Fe(CN)6].nH_2O: Synthesis, characterization and potential biomedical applications. *Inorg. Chem.* **2013**, 52, 2790-2792.
122. O'Brien, J.; Wilson, I.; Orton, T.; Pognan, F. Investigation of the Alamar Blue (resazurin) fluorescent dye for the assessment of mammalian cell cytotoxicity. *Eur. J. Biochem.* **2000**, 267, 5421-5426.

123. Becker, K.; Schroecksnadel, S.; Geisler, S.; Carriere, M.; Gostner, J. Effects of TiO_2 nanoparticles on human myelomonocytic cell line THP-1. *J. Nanomater. Mol. Nanotechnol.* **2014**, 0, 1-6.
124. Wang, Y.; Santos, A.; Kaur, G.; Evdokiou, A.; Losic, D. Structurally engineered anodic alumina nanotubes as nano-carriers for delivery of anticancer therapeutics. *Biomater.* **2014**, 35, 5517-5526.
125. Page, B.; Page, M.; Noel, C. A new fluorometric assay for cytotoxicity measurements in vitro. *Int. J. Oncol.* **1933**, 3, 473-476.
126. Malinouski, M.; Zhou, Y.; Belousov, V. V.; Hatfield, D. L.; Gladyshev, V. N. Hydrogen Peroxide Probes Directed to Different Cellular Compartments. *PLoS One* **2011**, 6, 14564.
127. Madej-Czerwonka, B. T. Standard in breast surgery-Breast units-future and necessity. *Contemp. Onkol.* **2014**, 18, 227− 229.
128. Cancer Facts & Figures 2018, American Cancer Society: Atlanta.
129. Reuter, S., Gupta, S.C., Chaturvedi, M.M., and Aggarwal, B.B. Oxidative stress, inflammation, and cancer: how are they linked?. *Free Radic. Biol. Med.* **2010**, 49 1603-1616.
130. Chen, X.; Tian, X.; Shin, L.; Yoon, J. Fluorescent and luminescent probes for detection of reactive oxygen and nitrogen species. *Chem. Soc. Rev.* **2011**, 40, 4783-4804.
131. Chan, J.; Dodani, S. C.; Chang, C. J. Reaction-based small-molecule fluorescent probes for chemoselective bioimaging. *Nat. Chem.* **2012**, 4, 973-984.
132. Belousov, V. V.; Fradkov, F.; Lukyanov, K. A.; Staroverrov, D. S.; Shakhbazov, K. S.; Terskikh, A. V.; Lukysnov, S. Genetically encoded fluorescent indicator for intracellular hydrogen peroxide. *Nat. Methods*, **2006**, 3, 281-286.
133. Grishma, M. R. Methods to detect hydrogen peroxide in living cells: Possibilities and pitfalls. *Comp. Biochem. Physiol. Part A: Mol. Integr. Physiol.* **2013**, 165, 429-438.
134. Winterbourn, C. C. The challenges of using fluorescent probes to detect and quantify specific reactive oxygen species in living cells. *Biochem. Biophys. Acta, Gen. Subj.* **2014**, 1840, 730-738.
135. Zbiljic, J.; Guzsvany, V.; Vajdle, O.; Prlina, B.; Agbaba, J.; Dalmacija, B.; Konya, Z.; Kalcher, K. Determination of H_2O_2 by MnO_2 modified screen printed carbon electrode during Fenton and visible light-assisted photo-Fenton based removal of acetamiprid fromwater. *J. Electroanal. Chem*, **2015**, 755, 77-86.
136. Wayu, M.; King, J.E.; Johnson, J.A.; Chusuei, C.C. A Zinc Oxide Carbon Nanotube Based Sensor for *In Situ* Monitoring of Hydrogen Peroxide in Swimming Pools. *Electroanal.* **2015**, 27, 2552-2558.
137. Palanisamy, S.; Cheemalapati, S.; Chen, S. M. Highly sensitive and selective hydrogen peroxide biosensor based on hemoglobin immobilized at multiwalled carbon nanotubes–zinc oxide composite electrode. *Anal. Biochem.* **2012,** 429, 108-115.
138. Lasfargues, E.; Ozzello, L. Cultivation of human breast carcinomas. *J. Natl. Cancer Inst.* **1958**, 21, 1131-1147.

139. Castles, C. G.; Fuqua, S. A. W.; Klotz, D. M.; Hill, S. M. Expression of a constitutively active estrogen receptor variant in the estrogen receptor-negative BF-20 human breast cancer cell line. *Cancer Res.* **1993**, 53, 5934-5939.
140. Pulaski, B. A.; Ostrand-Rosenberg, S. Mouse 4T1 breast tumor model. *Current Protocol Immunology: John Wiley & Sons*, **2000**, 39, 20.2.1-20.2.16.
141. Stefano, C.; Fabiana, A.; Danila, M.; Giuseppe, P.; Anthony, J. K. Development of a hydrogen peroxide sensor based on screen-printed electrodes modified with inkjet-printed Prussian Blue nanoparticles. *Sensors*, **2014,** 14, 14222-14234.
142. Pilco-Ferreto, N.; Calaf, G. M. Influence of doxorubicin on apoptosis and oxidative stress in breast cancer cell lines. *Int. J. Oncology* **2016,** 49, 753-762.
143. Harris, D. C. Quantitative Chemical Analysis, 8th ed. W. H. Freeman and company, New York, **2010**.
144. Westley, C.; Xu, Y.; Thilaganathan, B.; Carnell, A. J.; Turner, N. J.; Goodacre, R. Absolute quantification of uric acid in human urine using surface enhanced Raman scattering With the standard addition method. *Anal. Chem.* **2017**, 89, 2472-2477.
145. Sies, H. Hydrogen peroxide as a central redox signaling molecule in physiological oxidative stress: oxidative eustress. *Redox Biol.*, **2017**, 11, 613-619.
146. Renehen, Andrew G.; Catherine Booth, Christopher S. Potten. "What is apoptosis, and why is it important?" British Medical Journal. June 23, 3001. (March 8, 2010) http://www.ncbl.nlm.nih.gov/pmc/articles/PMC 1120576.
147. Choi, S. J.; Kim, M. H.; Lim, S. W.; Gwak, M. S. Effect of Ketamine on apoptosis by energy deprivation in astroglioma cells using flow cytometry system. *J. Korean Med. Sci.* **2005**, 20, 113-20.
148. Xi, Q.; Cheranov, S. Y.; Jaggar, J. H. Mitochondria-derived reactive oxygen species dilute cerebral arteries by activating Ca+2 sparks. *Circ. Res.* **2005**, 97, 354-362.
149. Niu, H.; Zhang, Y.; Tang, J.; Zhu, X.; Ye, Y.; Zhao, Y. A bifunctional fluorescent sensor for CCCP-induced cancer cell apoptosis imaging. *Chem. Commun.* **2020**, 56, 12423.
150. Park, Y. S.; Choi, S. E.; Koh, H. C. PGAM5 regulates PINK1/Parkin-mediated mitophagy via DRP1 in CCCP-induced mitochondrial dysfunction. *Toxic. Lett.* **2018**, 284, 120-128.
151. Birben, E.; Sahiner, U. M.; Sackesen, C.; Erzurum, S.; Kalayaci, O. Oxidative stress and antioxidant defense. *World Allergy Organ. J.* **2012**, 5, 9-19.
152. Stojanovic, Z. S.; Durovic, A. D.; Ashrafi, A. M.; Koudelkova, Z.; Zitka O.; Richtera, L. Highly sensitive simultaneous electrochemical determination of reduced and oxidized glutathione in urine samples using antimony trioxide modified carbon paste electrode. *Sens. Actuators B Chem.* **2020**, 318, 128141.
153. Harfield, C. J.; Batchelor-McAuley, C.; Compton, R. G. Electrochemical determination of glutathione: a review. *Analyst*, **2012**, 137, 2285-2296.
154. Vidyasagar, M. S.; Kodali, M.; Saxena, P. P.; Upadhya, D.; Krishna, C. M.; Vadhiraja, B. M.; Fernandes, D. J.; Bola Sadashiva, S. R. Predictive and prognostic significance of glutathione levels and DNA damage in cervix cancer patients undergoing radiotherapy. *Int. J. Radiation Oncology Biol. Phys.* **2010**, 78, 343-349.
155. Yeh, C. C.; Hou, M. F.; Wu, S. H.; Tsai, S. M.; Lin, S. K.; Hou, L. A.; Ma, H.; Tsai, L. Y. A study of glutathione status in the blood and tissues of patients with breast cancer. *Cell. Biochem. Funct.* **2006**, 24, 555-559.

156. Oktyabrsky, O. N.; Smirnovam, G. V.; Muzyka, N. G. Role of glutathione in regulation of hydroperoxidase I in growing Escherichia coli. *Free Radic. Biol. Med.*, **2001**, 31, 250.
157. Vina, J. Glutathione: Metabolism and physiological functions, CRC, Boca Raton, 2000.
158. Dolphin, D.; Poulson, R.; Avramovic, O. Glutathione: Chemical, biochemical and medical aspects, Wiley, New York, 1989.
159. Hartfield, J. C.; Batchelor-McAuley, C.; Compton, R. G. Electrochemical determination of glutathione: a review. *Analyst*, **2012**, 137, 2285-2296.
160. Pang, H.; Shi, Y.; Du, J.; Ma, Y.; Li, G.; Chen, J.; Zhang, J.; Zheng, H. Yuan, B. Porous nickel oxide microflowers synthesized by calcination of coordination microflowers and their applications as glutathione electrochemical sensor and supercapacitors. *Electrochim. Acta*, **2012**, 85, 256-262.
161. Zaidi, S. A.; Shin, J. H. A review on the latest developments in nanostructure-based electrochemical sensor for glutathione. *Anal. Methods*, **2016**, 8, 1745-1754.
162. Sies, H. Glutathione and its role in cellular functions. *Free Radic. Biol. Med.* **1999**, 27, 916-921.
163. Meister, A. Glutathione metabolism and its selective modification. *J. Biol. Chem.*, **1988**, 263, 17205 – 17208.
164. Forman, H. Y.; Zhang, H.; Rinna, A. Glutathione: overview of its protective roles, measurement, and biosynthesis. *Mol. Aspects Med.* **2009**, 30, 1 – 12.
165. Rahman, I.; Kode, A.; Biswas, S. K. Assay for quantitative determination of glutathione and glutathione disulphide levels using enzymatic recycling method. *Nat. Protocols*, **2006**, 1, 3159-3165.
166. Rahman, I.; Li, X. Y.; Donaldson, K.; Harrison, D. J.; MacNee, W. Glutathione homeostasis in alveolar epithelial cell in vitro and lung in vivo under oxidative stress. *Am. J. Physiol.* **1995**, 269, L285-L292.
167. Rahman, I.; Bel, A.; Mulier, B.; Donaldson, K.; MacNee, W. Differential effects of oxidants and dexamethasone on y-glutamyl cysteine synthetase and y-glutamyl transpeptidase in alveolar epithelial cells. *Am. J. Physiol.* **1998**, 275, L80 – L86.
168. Morrison, D.; Rahman, I.; Lannan, S.; MacNee, M. Epithelial permeability, inflammation, and oxidant status in the air spaces of chronic smokers. *Am. J. Respir. Care Med.* **1999**, 159, 1-8.
169. Cantin, A. M.; North, S. L.; Hubbard, R. C.; Crystal, R. G. Normal alveolar epithelial lining fluid contains high level of glutathione. *Am. J. Physiol.* **1987**, 63, 152-157.
170. Raggi, M. A.; Nobile, L.; Giovannini, A. G. Spectrophotometric determination of glutathione and of its oxidation product in pharmaceutical dosage form. *J. Pharm. Biomed. Anal.* **1991**, 9, 1037-1040.
171. Liang, S. C.; Wang, H.; Zhang, Z. M.; Zhang, X.; Zhang, H. S. Direct spectrofluorometric determination of glutathione in biological samples using 5-maleimidyl-2-(m-methylphenyl) benzoxazole. *Anal. Chim. Acta*, **2002**, 451, 211-219.
172. Zhang, J.; Hu, Z.; Chen, X. Quantification of glutathione and glutathione disulfide in human plasma and tobacco leaves by capillary electrophoresis with laser induced fluorescence detection. *Talanta* **2005**, 65, 986-990.
173. Kandar, R.; Zakova, P.; Lotkova, H.; Kucera, O.; Cervinkova, Z. Determination of reduced and oxidized glutathione in biological samples using liquid chromatography with fluorimetric detection. *J. Pharm. Biomed. Anal.* **2007**, 43, 1382 –1387.

174. Katrusiak, A. E.; Paterson, P. G.; Kamencic, H.; Shokar, A.; Lyon, A. W. Pre-column derivatization high-performance liquid chromatographic method for determination of cysteine, cysteinyl-glycine, homocysteine and glutathione in plasma and cell extracts. *J. Chromatogra. B* **2001**, 758, 207-212.
175. Xu, F.; Wang, L.; Gao, M.; Jin, L.; Jin, J. Amperometric determination of glutathione and cysteine on a Pd-IrO(2) modified electrode with high performance liquid chromatography in rat brain microdialysate. *Anal. Bioanal. Chem.* **2002**, 372, 791-794.
176. Causse, E.; Malatray, P.; Calaf, R.; Charpiot, P.; Candito, M.; Bayle, C.; Valdiguie, P.; Salvayre, R.; Couderc, F. Plasma total homocysteine and other thios analyzed by capillary electrophoresis/laser-induced fluorescence detection: comparison with two other methods. *Electrophoresis*, **2000**, 21, 2074-2079.
177. Satah, I.; Arakawa, S.; Okamoto, A. Flow injection determination of glutathione with amperometric monitoring of the enzymatic reaction. *Anal. Chim. Acta* **1988**, 214, 415-419.
178. Raoof, J. B.; Ojani, R.; Karimi-Maley, H. Electrocatalytic oxidation of glutathione at carbon paste electrode modified with 2, 7-bis(ferrocenyl ethyl) fluoren-9-one: application as a voltammetric sensor. *J. Appl. Electrochem.* **2009**, 39, 1169-1175.
179. Ensafi, A. A.; Taei, M.; Khayamian, T.; Karimi-Maley, H.; Hasanpour, F. Voltammetric measurement of trace amount of glutathione using multiwall carbon nanotubes as a sensor and chlorpromazine as a mediator. *J. Solid State Electrochem.* **2010**, 14, 1415-1423.
180. Lash, L. H.; Jones, D. P. Distribution of oxidized and reduced forms of glutathione and cysteine in rat plasma. *Arch. Biochem. Biophys*. **1985**, 240, 583-592.
181. Sapi, E.; Flick, M. B.; Rodov, S.; Kacinsk, B. M. Ets-2 transdominant mutant abolishes anchorage-independent growth and macrophage colony-stimulating factor-stimulated invasion by BT20 breast carcinoma cells. *Cancer Res.* **1998**, 58, 1027-1033.
182. Siegel, R. L., K. D. Miller, H. E. Fuchs, and A. Jemal. 2021. Cancer statistics, CA: *A Cancer Journal for Clinicians* **2021**, 71, 7–33. doi:10.3322/caac.21654.
183. Kader, M. S., and C. C. Chusuei. 2020. A Cobalt (II) Oxide Carbon Nanotube Composite to Assay Dopamine. *Chemosensors* **2020**, 8, 22–29. doi:10.3390/chemosensors8020022.
184. Khamlichi, R. E..; Bouchta, D..; Anouar, E. H..; Atia, M. B..; Attar, A.; Choukairi, M.; Tazi, S.; Ihssane, R.; Faiza, C.; Khalid, D.; Khalid, R. A novel l-leucine modified sol-gel-carbon electrode for simultaneous electrochemical detection of homovanillic acid, dopamine and uric acid in neuroblastoma diagnosis. *Mater. Sci. Eng. C, Mater. Biol. Appl.* **2017**, 71, 870–878. doi:10.1016/j.msec.2016.10.076.
185. Yang, S.; Zhao, J.; Tricard, S.; Yu, L.; Fang, J. A Sensitive and selective electrochemical sensor based on N, P-doped molybdenum Carbide@Carbon/Prussian blue/graphite felt composite electrode for the detection of dopamine. *Anal. Chim. Acta* **2020**, 1094, 80–89. doi: 10.1016/j.aca.2019.09.077.
186. Yi, I. J., Kim, J. H.; Kang, C. J.; Choi, Y. J.; Lee, K.; Kim, Y. S. A novel electrochemical sensor using prussian blue modified indium tin oxide electrode. *Japanese J. Appl. Phys.* **2006**, 45, 438–441. doi:10.1143/JJAP.45.438.
187. Roychoudhury, A.; Prateek, A.; Chauhan, N.; Kumar, D. S.; Basu, S.; Jha, S. K. Tyrosinase-conjugated Prussian blue-modified oxide nanoparticles-based interface for selective detection of dopamine. *ChemistrySelect* **2017**, 2, 6118–28. doi:10.1002/slct.201701304.
188. Yan, Z.; Zhang, Y.; Yang, H.; Fan, G.; Ding, A.; Liang, H.; Li, G.; Ren, N.; and Bruggen, B. V. D. Mussel-inspired polydopamine modification of polymeric membranes for the application of

water and wastewater treatments: a review. *Chem. Eng. Res. Design* **2020**, 157, 195–214. doi:10.1016/j.cherd.2020.03.011.

189. Vecchia, N. F.D; Avolio, R.; Alfe, M; Errico, M. E.; Napolitano, A.; d'Ischia. M. Building block diversity in polydopamine underpins a multifunctional eumelanin-type platform tunable through a quinone control point. *Adv. Func. Maters.* **2013**, 23, 1331–1340. doi: 10.1002/adfm.201202127.
190. Huang, J.; Liu, Y.; Hou, H.; T. You, T. Simultaneous electrochemical determination of dopamine, uric acid, and ascorbic acid using palladium nanoparticle-loaded carbon nanofibers modified electrode. *Biosens. Bioelectron.* **2008**, 24, 632–637. doi:10.1016/j.bios.2008.06.011.
191. Li, H. ; Zhou, K. ; Cao, J. ; Wei, Q. ; Lin, C. T. ; Pei, S. E. ; Ma, L. ; Hu, N. ; Guo, Y. ; Deng, Z. et al. 2021. A novel modification to boron-doped diamond electrode for enhanced, selective detection of dopamine in human serum. *Carbon* **2021**, 171, 16–28. doi:10.1016/j.carbon.2020.08.019.
192. Wang, M.; Gao, Y; Zhang, J; Zhao, J. Highly dispersed carbon nanotube in new ionic liquid-graphene oxides aqueous dispersions for ultrasensitive dopamine detection. *Electrochim. Acta* **2015**, 155, 236–43. doi:10.1016/j.electacta.2014.12.114.
193. Liu, Y.; Ai, K.; Lu, L. Polydopamine and its derivative materials: synthesis and promising applications in energy, environmental, and biomedical fields. *Chem. Rev.* **2014**, 114, 5057–115. doi:10.1021/cr400407a.
194. Yang, J.; L. Niu, L.; Zhang, Z.; Zhao, J.; L. Chou, L. Electrochemical behavior of a polydop-amine nanofilm. *Anal. Lett.* **2015**, 48, 2031–2039. doi:10.1080/00032719.2015.1010120.
195. Zanello, P. Inorganic electrochemistry: theory, practice, and application. Cambridge, UK: Royal Society of Chemistry, 2003.
196. Garcia, A.; Heinanen, M.; Jemenez, L. M.; Barbas, C. Direct measurement of homovanillic, vanillylmandelic and 5-hydroxyindoleacetic acid in urine by capillary electrophoresis. *J. Chromatogr. A* **2000**, 871, 341-350.
197. Nemeckova-Makrlikova, A.; Barek, J.; Navratil, T.; Fischer, J. Simultaneous determination of tumour biomarkers homovanilic acid, vanillylmandelic acid, and 5-hydroxyindole-3-acetic acid in human urine using single run HPLC with a simple wall-jet glassy carbon electrochemical detector. *J. Electroanal. Chem.* **2020**, 878, 114629.
198. Modak, S.; Cheung, N. K. V. Neuroblastoma: Therapeutic strategies for a clinical enigma. *cancer treat. rev.* **2010**, 36, 307-317.
199. Lewitt, P.; Schultz, L.; Auinger, P.; Lu, M. CSF xanthine, homovanillic acid, and their ratio as biomarkers of Parkinson's disease. *Brain Res.* **2011**, 1408, 88-97.
200. Sher, L.; Mann, J. J.; Traksman-Bendz, R.; Winchel, R.; Huang, Y. Y.; Fertuck, E.; Stanley, B. H. Lower cerebrospinal fluid homovanillic acid levels in depressed suicide attempters. *J. Affect. Disord.***2006**, 90, 83-89.
201. Suzuki, E.; Kanba, S.; Nibuya, M.; Adachi, S.; Sekiya, U.; Shintani, F.; et al. Longitudinal changes in symptoms and plasma homovanillic acid levels in chronically medicated schizophrenic patients. *Biol. Psychiatry* **1994**, 36, 654-661.
202. Quan-Bui, K. H. L.; Plaisant, O.; Leboyer, M.; Gay, C.; Kamal, L.; Devynck, M. A.; Meyer, P. Reduced platelet serotonin in depression. *Psychiatry Res.* **1984**, 13, 129-139.
203. Zhou, Y.; Yan, H.; Xie, Q.; Huang, S.; Liu, J.; Li, Z.; et al. Simultaneous analysis of dopamine and homovanillic acid by high-performance liquid chromatography with wall-jet/thin-layer electrochemical detection. *Analyst* **2013**, 138, 7246-7253.
204. Lionetto, I.; Lostia, A. M.; Stigliano, A.; Cardelli, P.; Simmaco, M. HPLC-mass spectrometry method for quantitative detection of neuroendocrine tumor markers:

Vanillylmandelic acid, homovanillic acid and 5-hydroxyindoleacetic acid. *Clin. Chim. Acta* **2008**, 398, 53-56.
205. Fauler, G.; Leis, H. J.; Huber, E.; Schellauf, C.; Kerbi, R.; Urban, C.; Gleispach, H. Determination of homovanilic acid and vanillylmandelic acid in neuroblastoma screening by stable isotope dilution GC-MS. *J. Mass Spectrom.* **1997**, 32, 507-514.
206. Taran, F.; Frobert, Y.; Creminon, C.; Grassi, J.; Olichon, D.; Mioskowski, C.; Pradelles, P. Competitive enzyme immunoassay with monoclonal antibody for homovanillic acid measurement in human urine samples. *Clin. Chem.* **1997**, 43, 363-368.
207. Li, X.; Jin, W.; Weng, Q. Separation and determination of homovanillic acid and vanillylmandelic acid by capillary electrophoresis with electrochemical detection. *Anal. Chim. Acta* **2002**, 461, 123-130.
208. Bell, D.S. Beware the low urine pH-the major cause of the increased prevalence of nephrolithiasis in patient with type 2 diabetes. *Diabetes Obes. Metab.* **2012**, 14, 299–303.
209. Turner, A. J.; Hick, P. E. Inhibition of aldehyde reductase by acidic metabolites of the biogenic amines. *Biochem. Pharmacol.* **1975**, 24, 1731-1733.
210. Pandey, R. R.; Chusuei, C. C. Electrochemical detection of dopamine using a Prussian blue zinc carbon nanotube composite decorated with agglomerated ZnO particles. *Anal. Lett.* **2021**, https://doi.org/10.1080/00032719.2021.2010090.

Appendices

Appendix A: Experimental Set up for maintenance of live cell culture

For the maintenance of live cells, the electrochemical cell is autoclaved to make it sterile. The volume of 2 mL of A 549 cells with 10^6 cells/mL is transferred into the electrochemical cells. The temperature is maintained at 37^0 C using heat plate and temperature monitoring device whereas 5% CO_2 is maintained using pressurized device. The experimental setup for monitoring H_2O_2 in CCCP treated live cells at various time points is shown in Scheme A1.

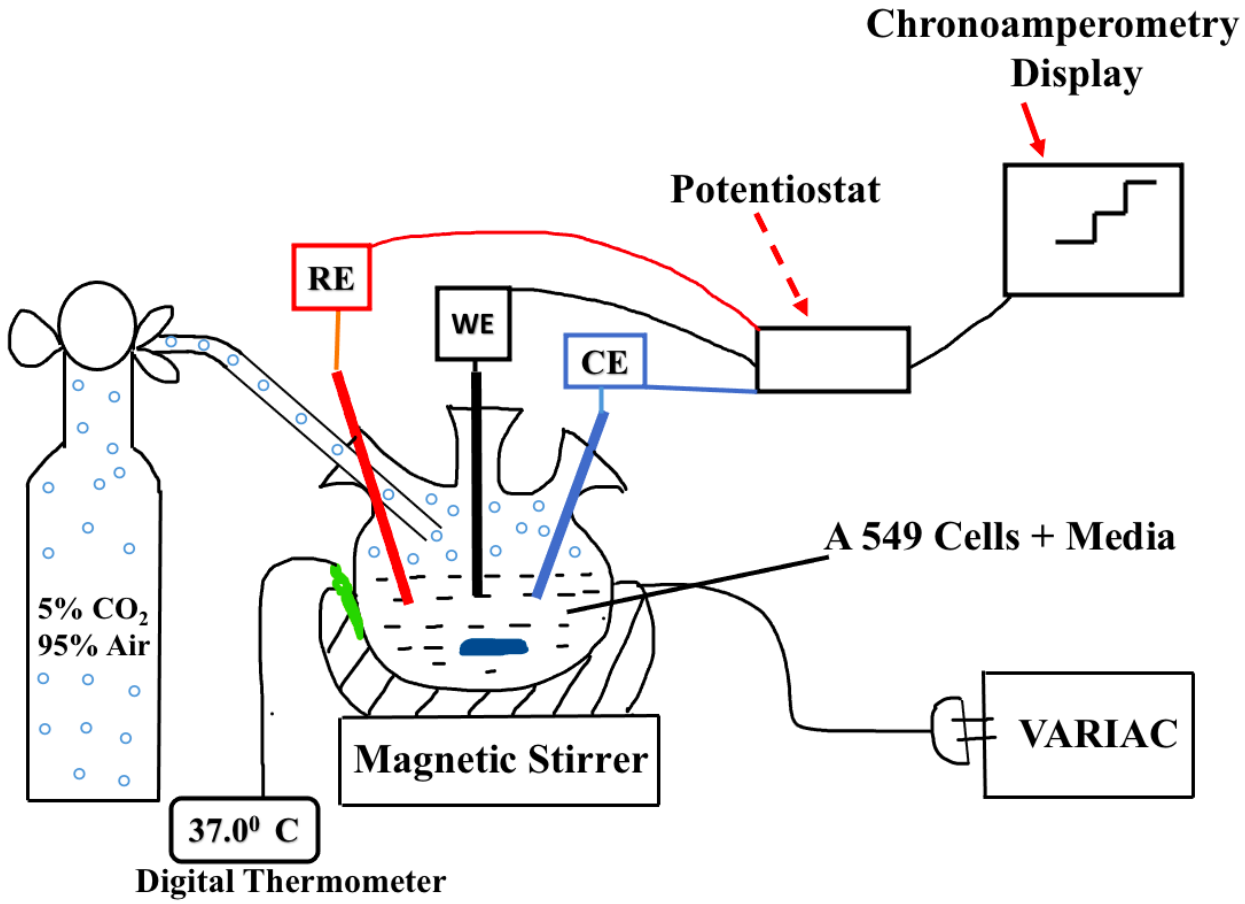

Scheme A1: Experimental set up of H_2O_2 monitoring in CCCP treated A 549 cancer cells.

Appendix B: A study of GSH and H2O2 under SAM CA method

The standard addition method under chronoamperometry was applied to detect GSH in BT20 cells using various concentrations of CCCP. The raw results are shown below:

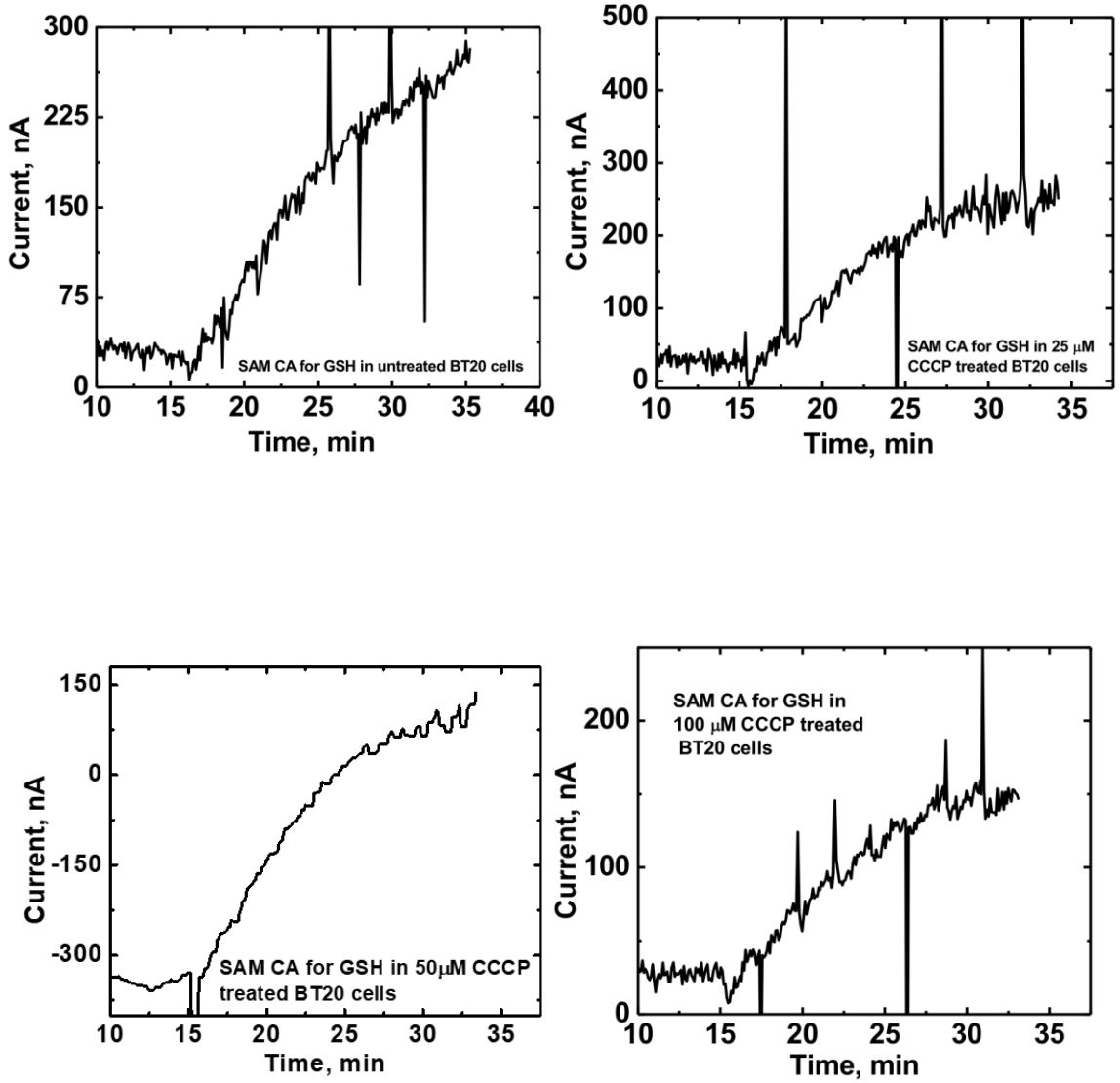

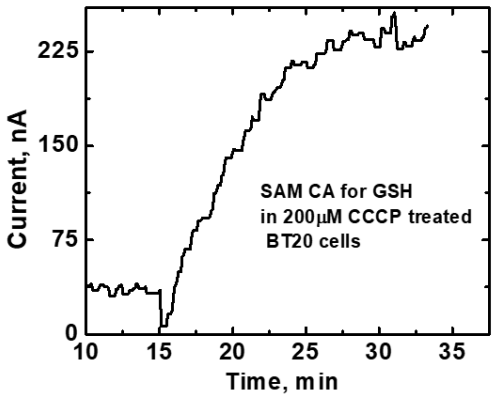

Figure B1: GSH analysis under SAM CA method using various concentrations of CCCP treated BT20 cells

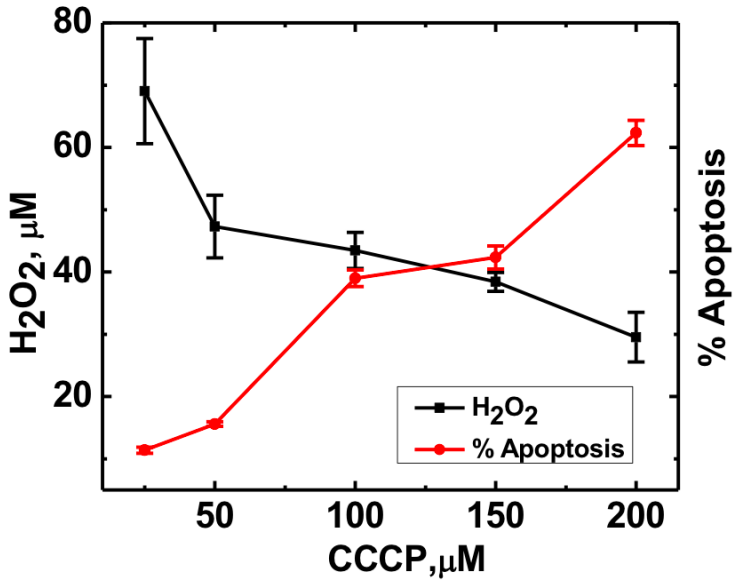

Figure B2: The relationship between apoptosis and oxidative stress obtained from BT20 cells

Appendix C: Electroactive surface area of PB/ZnO/COOH-MWNTs and ZnO/COOH-MWNTs in comparison

For quasi-reversible and irreversible processes in CV, the peak current is given by Randles-Sevcik expression,

$$I_p = (2.69 \times 10^5)\, n\, (n\alpha)^{1/2}\, ACD^{1/2}\, V^{1/2}$$

Where I_p, α, n, A, D, C and V represent the peak current in amps, transfer coefficient, the number of electrons, the electrode area (cm^2), the diffusion coefficient ($cm^2 \cdot s^{-1}$), the concentration in mol cm^{-3} and the scan rate in $V \cdot s^{-1}$, respectively. In this analysis, all parameters excluding the electrode surface areas were not altered. We compared the electroactive surface areas between ZnO/COOH-MWNTs and PB/ZnO/COOH-MWNTs towards the reduction of H_2O_2.

For ZnO/COOH-MWNTs,

$$I_p = 0.125 \times 10^{-3}\ A = (2.69 \times 10^5)\, n\, (n\alpha)^{1/2}\, A_{ZnO/COOH\text{-}MWNTs} CD^{1/2}\, V^{1/2} \quad \ldots\ldots\ldots\ldots\ldots\ldots\ldots\ldots (1)$$

For PB/ZnO/COOH-MWNTs

$$I_p = 0.430 \times 10^{-3}\ A = (2.69 \times 10^5)\, n\, (n\alpha)^{1/2}\, A_{PB/ZnO/COOH\text{-}MWNTs} CD^{1/2}\, V^{1/2} \quad \ldots\ldots\ldots\ldots\ldots\ldots\ldots\ldots (2)$$

Comparing equations (1) and (2),

$$A_{PB/ZnO/COOH\text{-}MWNTs} / A_{ZnO/COOH\text{-}MWNTs} = \frac{0.430}{0.125} = 3.44$$

This result indicate the significant impact of incorporating PB on the surface of ZnO/COOH-MWNTs for enhancing the electroactive surface area of the resulting nanocomposites.

Appendix D: Permissions from Journal Publishers

ACS Publications
Most Trusted. Most Cited. Most Read.

A Prussian Blue ZnO Carbon Nanotube Composite for Chronoamperometrically Assaying H2O2 in BT20 and 4T1 Breast Cancer Cells

Author: Raja Ram Pandey, Yuhang Guo, Ying Gao, et al
Publication: Analytical Chemistry
Publisher: American Chemical Society
Date: Aug 1, 2019

Copyright © 2019, American Chemical Society

PERMISSION/LICENSE IS GRANTED FOR YOUR ORDER AT NO CHARGE

This type of permission/license, instead of the standard Terms and Conditions, is sent to you because no fee is being charged for your order. Please note the following:

- Permission is granted for your request in both print and electronic formats, and translations.
- If figures and/or tables were requested, they may be adapted or used in part.
- Please print this page for your records and send a copy of it to your publisher/graduate school.
- Appropriate credit for the requested material should be given as follows: "Reprinted (adapted) with permission from {COMPLETE REFERENCE CITATION}. Copyright {YEAR} American Chemical Society." Insert appropriate information in place of the capitalized words.
- One-time permission is granted only for the use specified in your RightsLink request. No additional uses are granted (such as derivative works or other editions). For any uses, please submit a new request.

If credit is given to another source for the material you requested from RightsLink, permission must be obtained from that source.

BACK CLOSE WINDOW

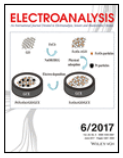

A Zinc Oxide Carbon Nanotube Based Sensor for In Situ Monitoring of Hydrogen Peroxide in Swimming Pools

Author: Mulugeta B. Wayu, Julie E. King, Jacqueline A. Johnson, et al
Publication: Electroanalysis
Publisher: John Wiley and Sons
Date: Jul 15, 2015

© 2015 WILEY-VCH Verlag GmbH & Co. KGaA, Weinheim

Order Completed

Thank you for your order.

This Agreement between Mr. Raja Pandey ("You") and John Wiley and Sons ("John Wiley and Sons") consists of your license details and the terms and conditions provided by John Wiley and Sons and Copyright Clearance Center.

Your confirmation email will contain your order number for future reference.

Printable Details

License Number	5219411271125
License date	Dec 31, 2021

Licensed Content

Licensed Content Publisher	John Wiley and Sons
Licensed Content Publication	Electroanalysis
Licensed Content Title	A Zinc Oxide Carbon Nanotube Based Sensor for In Situ Monitoring of Hydrogen Peroxide in Swimming Pools

Order Details

Type of use	Dissertation/Thesis
Requestor type	University/Academic
Format	Print and electronic
Portion	Figure/table
Number of figures/tables	2

lanl20:Electrochemical Detection of Dopamine Using a Prussian Blue Carbon Nanotube Composite Decorated with Agglomerated ZnO Particles

A

Academic UK Non Rightslink <permissionrequest@tandf.co.uk>
Mon 12/13/2021 4:33 PM

To:

- Raja Ram R. Pandey

Thank you for your e-mail which has been received by the Taylor & Francis Journal Permissions Team.
Permissions requests currently have a processing time of up to 4 weeks, however, some requests may take longer depending on the complexity of the request and any difficulties incurred whilst tracing records.

The quickest way to secure permission is to request permission via Copyright Clearance Center's RightsLink® which enables you to obtain instant price quotes, place orders and track all your licensing activity in real-time.
More in depth details on requesting permissions via RightsLink® can be found here.
We ask you to be patient during this process and to avoid re-sending your request now that you have received this confirmation e-mail as we are unable to make exceptions to our normal processing time to account for any pending deadlines you may face.
Please note that under no circumstances is it to be assumed that permission has been granted based on a response not having been received within our or your own specified time frame.

If you are requesting permission to reuse journal content commercially, advertising, or reprints please contact the commercial team directly: TFCorpermissions@informa.com
If you are requesting permission to reuse book content, please contact the books permission team directly: bookspermissions@tandf.co.uk

Best wishes,
Taylor & Francis Academic Journals Permissions Team
+44 (0)20 8052 0600